Analysis of thoracic and intra-gastric cardiac vibration signals for the monitoring of heart failure

Henry Jhoán Areiza Laverde

COLLEGE DOCTORAL BRETAGNE | MATHS, TELECOMS INFORMATIQUE, SIGNAL SYSTEMES, ELECTRONIQUE

Université de Rennes

DOCTORAL THESIS OF

UNIVERSITÉ DE RENNES

DOCTORAL SCHOOL N° 601
Mathématiques, Télécommunications, Informatique, Signal, Systèmes, Électronique
Specialty: *Signal, Image, Vision*

By

Henry Jhoán AREIZA LAVERDE

Analysis of thoracic and intra-gastric cardiac vibration signals for the monitoring of heart failure

Thesis presented and defended in Rennes, on March 10, 2023
Research Unit: LTSI, UMR Inserm 1099 Laboratoire Traitement du Signal et de l'Image

Rapporteurs before defense:

Philippe CINQUIN	Professeur des universités - Praticien hospitalier, Université Grenoble-Alpes
Sofiane BOUDAOUD	Professeur des universités, Université de Technologie de Compiègne (UTC)

Composition of the Jury:

President:	Corinne MAILHES	Professeur des universités, INP-ENSEEIHT Toulouse
Reviewers:	Philippe CINQUIN	Professeur des universités - Praticien hospitalier, Université Grenoble-Alpes
	Sofiane BOUDAOUD	Professeur des universités, Université de Technologie de Compiègne (UTC)
Thesis director:	Alfredo HERNÁNDEZ	Research Director at INSERM, LTSI-INSERM, Université de Rennes
Thesis co-director:	Lotfi SENHADJI	Professeur des universités, LTSI-INSERM, Université de Rennes

To my precious Marti,
because in her I have found the meaning of love, and...
all we need is love.

Acknowledgement

No podría dejar pasar esta oportunidad sin hacer un debido reconocimiento a todas aquellas personas que me han ayudado a llegar hasta aquí. En este punto de mi vida, tengo más que claro el inmenso valor de las enseñanzas que he recibido por parte de mis maestros y compañeros, pues es la suma de todo ese valioso conocimiento lo que ahora me permite escribir estas palabras.

Mis primeros maestros, y sin duda los más importantes, han sido mis padres: Mariela Laverde y Luis Areiza. A estos maestros les debo la vida, la cual me dieron y me enseñaron a cuidar desde que pude dar mi primer respiro. Ellos me enseñaron que la vida es una aventura, y que como en toda aventura, llegarían momentos difíciles en los cuales dudaría incluso de mí mismo, pero aún en esos momentos, ellos nunca dudarían de mí y siempre estarían a mi lado para apoyarme. Enseñanzas como esa no solo se graban en tu mente sino también en tu corazón, pues incluso ahora estando lejos de ellos físicamente, no ha pasado un solo segundo en el cual no haya sentido su apoyo y amor incondicional. Así como mis primeros maestros fueron mis padres, está claro que mis primeros compañeros fueron mis hermanos: Iván y Alejandra. Junto a ellos aprendí que esta aventura se vive mejor con locura y pasión, y en los momentos más importantes, en los que sientes una necesidad incontrolable de reír o llorar, siempre es mejor tener a alguien a tu lado para poder compartir esos sentimientos con un fuerte abrazo.

Desde niño tuve el privilegio de tener acceso a la educación formal, y hago énfasis en el lamentable hecho de que la educación es un privilegio y no un derecho en muchos lugares del mundo, pero eso es tema de otra discusión. Desde entonces me he sentido maravillado por la gran cantidad de conocimiento que se ha presentado ante mí: Matemáticas, Idiomas, Física, Geografía, Informática, Ética, Biología, Arte, Filosofía, entre otras disciplinas que me fueron impartidas en la Institución Educativa Barrio París por excelentes maestros como Míriam Echavarría, Duván Castro, Luis F. Bohórquez, Nelson Parra, Gladys Maya, Marta Zapata, Genoveva Valoyes, Alder Zapata, Soledad Bermúdez, y muchos otros a los cuales no me queda más que agradecerles por su infinita paciencia y entrega a la labor. Gracias a ellos pude afianzar mi amor por el aprendizaje, encendiendo en mí la chispa del motor que desde entonces no ha parado de girar y que me ha traído tan lejos; el motor de la curiosidad. Durante aquella época tuve compañeros que me enseñaron el valor de la amistad sincera y el trabajo en equipo. Aunque hay muchos más de los que aquí podría nombrar, son Jorge Chavarría, Iván Mejía, Jónathan Gil y Diego Calderón a quienes no podría dejar sin una mención especial en estos agradecimientos, porque más que ser mis compañeros, se convirtieron en mis hermanos, y me enseñaron que los lazos de amistad pueden llegar a ser incluso más fuertes que algunos lazos de sangre.

Es en la universidad donde empezó a tomar sentido para mí aquella célebre frase del gran filósofo Sócrates: *"solo sé que no sé nada"*, pues pude entender que entre más recorría el vasto océano del conocimiento, este más amplio y profundo se volvía. Ante tal ironía, tuve la suerte de encontrarme con nuevos maestros que, si bien se encontraban navegando en este viaje infinito que es el aprendizaje, ya contaban con experiencia y herramientas extremadamente útiles que pusieron a mi disposición, y es gracias a esa ayuda invaluable que ahora puedo navegar con mayor confianza y a buen ritmo. Fue en la Institución Universitaria ITM donde guiado por profesores como Jorge Jaramillo, Gloria Díaz, Andrés Castro, María C. Torres y Carlos Madrigal, pude enfocar mi ruta de aprendizaje hacia lugares que nunca hubiera imaginado. De la misma forma que encontré estos maestros, especialistas en cada una de sus áreas de conocimiento, pude encontrar nuevos compañeros cada vez más afines al tipo de conocimiento que capturaba mi atención: Diana Marín, Deivid Botina, Carlos Duarte, Fernando Pamplona, entre algunos otros que me acompañaron y me enseñaron que los grandes esfuerzos siempre son bien recompensados.

I need to change the language of my discourse at this point considering to whom my thanks are addressed. My most recent mentors and thesis advisors, Professors Alfredo Hernandez and Lotfi Senhadji, who gave me the opportunity to study this PhD and who guided me at every step of the way with a level of wisdom worthy of the greatest minds I have ever met in my life, and a kindness so great as to make me feel that I have a home on this side of the world. Taking this PhD has been one of the most enriching experiences of my life, not only professionally but also in personal terms. For this, an infinite thanks to them. I have also shared this experience with amazing colleagues from all over the world, most of them joining my valuable list of close friends: Marina Valdés, Shan Bisht, Carole Boëffard, Kimi Owashi, Paula Castillo, Prem Chhetri, among many others who have taught me that friendship has no borders. In addition, with special thanks for their valuable help in the completion of this thesis: Gustavo Guerrero, Remo Lazazzera, Gabriel Dieuset, Ismail Ben Ihya, Fabrice Tudoret, and Miguel Castro.

Finalmente, habiendo agradecido todo el conocimiento que he adquirido hasta ahora, me atrevo a dar las gracias por el conocimiento que estoy por adquirir, claramente esperando que la vida y el tiempo me permitan continuar el viaje. Y puedo sentirme afortunado, pues ese aprendizaje futuro ya empiezo a verlo materializado en una persona, Martina Sacco, quien ya tiene el papel de maestra y compañera en mi vida, y a su lado he aprendido una de las enseñanzas más valiosas que tengo hasta ahora: *"Beautiful things don't ask for attention"*. Junto a ella, espero poder convertirme también en maestro cuando llegue el momento, uno que pueda llenar de orgullo a todas las personas mencionadas en estos agradecimientos y todas las demás que forman parte de mi vida.

Henry Areiza

Résumé en français

Les maladies cardiovasculaires (CVD) sont la principale cause de décès dans le monde et une cause majeure d'invalidité [1, 2]. Au cours des dernières décennies, son incidence a fortement augmenté : le nombre total de cas prévalents de CVD a presque doublé, passant de 271 millions en 1990 à 523 millions en 2019, et le nombre de décès par an est passé de 12.1 millions en 1990 à 18.6 millions en 2019 [3]. Dans une étude du European Heart Network, il a été estimé que les CVD coûtaient €210 milliards par an à l'économie de l'Union européenne en 2015, dont 53% (€111 milliards) résultaient des coûts de soins de santé, 26% (€54 milliards) des pertes de productivité et 21% (€45 milliards) des soins informels aux personnes atteintes de CVD [4]. Parmi les CVD, l'insuffisance cardiaque (HF) est une affection qui survient lorsqu'il y a une altération de la structure ou du fonctionnement du cœur, en particulier du ventricule gauche (LV). Selon les estimations, 64.3 millions de personnes souffraient d'insuffisance cardiaque dans le monde en 2017, et le coût financier de l'insuffisance cardiaque était estimé à $30.7 milliards aux États-Unis en 2012, avec une projection jusqu'en 2030 révélant une augmentation probable des coûts de 127%, soit $69.8 milliards [5]. Ces données montrent que la charge des CVD représente un problème à la fois sanitaire et économique pour les systèmes de santé du monde entier, et qu'elle devrait augmenter considérablement dans les années à venir avec le vieillissement de la population mondiale.

Les patients souffrant de pathologies chroniques impliquant le système cardiovasculaire, comme l'insuffisance cardiaque, peuvent bénéficier d'une surveillance à distance à long terme des principaux paramètres cardiovasculaires afin d'adapter leur traitement de manière personnalisée et continue et de diagnostiquer précocement les événements de décompensation qui peuvent gravement endommager le fonctionnement normal du cœur [6, 7]. Ce diagnostic précoce peut réduire considérablement le risque que le patient doive être hospitalisé, ce qui s'est avéré être la principale cause de l'augmentation des coûts des soins de santé [4]. L'analyse des signaux de vibration cardiaque (CVS), sources intéressantes d'informations sur l'activité mécanique cardiaque, a déjà donné des résultats remarquables dans ce contexte, principalement parce que les principales caractéristiques de ces signaux ont été associées à certains marqueurs hémodynamiques utiles [8, 9]. De plus, la technologie des systèmes micro-électro-mécaniques (MEMS), couramment utilisés pour acquérir les CVS, s'est considérablement améliorée au cours des deux dernières décennies en termes de taille, de coût et de résolution.

Les CVS peuvent être acquis de manière non invasive au niveau du thorax, de la même manière que les médecins utilisent le stéthoscope pour écouter le phonocardiogramme (PCG) [10].

L'acquisition de signaux d'accélérométrie à partir du thorax du patient, en utilisant notamment ces dispositifs MEMS, conduit à l'observation du sismocardiogramme (SCG). L'acquisition et le traitement du SCG ont été largement développés au cours de la dernière décennie avec de nombreuses applications [11], y compris la possibilité de surveiller le SCG en ambulatoire [12, 13]. Cependant, les méthodes permettant d'obtenir des données de vibration cardiaque de haute qualité, chroniques et longitudinales, qui ne nécessitent pas l'implication d'un médecin ou du patient pour acquérir correctement et régulièrement ces signaux, restent à développer. Les systèmes implantables peuvent être une solution à ce défi d'observabilité.

Plusieurs études ont étudié comment acquérir des signaux accélérométriques pour mesurer la vibration cardiaque à l'intérieur des cavités cardiaques de manière invasive [14, 15]. Il a été démontré que les valeurs d'amplitude des principales composantes de vibration cardiaque de ces signaux sont significativement corrélées à des marqueurs hémodynamiques significatifs [8, 9, 16]. Certains dispositifs cardiaques implantables (ICD), tels que les appareils de thérapie de resynchronisation cardiaque (CRT), intègrent déjà des capteurs accélérométriques pour observer et analyser les signaux d'accélérométrie cardiaque, dans le but de prédire les futurs événements d'insuffisance cardiaque [17, 18] ou de définir des protocoles d'optimisation automatique des paramètres des ICD [19, 14]. Néanmoins, certains des principaux problèmes liés à l'utilisation des ICD sont les risques associés aux procédures hautement invasives qui doivent être réalisées pour capturer les signaux d'accélérométrie en contact direct avec le cœur [20, 21].

Notre équipe a déjà proposé des méthodes d'acquisition et de traitement des signaux mécaniques cardiaques provenant d'accéléromètres intégrés dans la sonde de stimulation des ICD [14, 15, 22]. Plus précisément, certaines de ces méthodes visaient à extraire des caractéristiques des signaux d'accélérométrie thoracique et à les comparer aux marqueurs hémodynamiques classiques de l'échocardiographie afin d'optimiser les paramètres des dispositifs CRT implantés chez les patients souffrant d'insuffisance cardiaque [23, 24]. Cependant, tous les patients ne peuvent pas bénéficier d'un dispositif cardiaque implantable actif, exigeant ainsi le développement de méthodes personnalisées qui peuvent être adaptées aux besoins de chaque patient [25, 26]. Par conséquent, il est clair que le développement d'un système de surveillance des vibrations cardiaques offrant une gestion intégrée des paramètres multimodaux avec un dispositif peu invasif est actuellement nécessaire dans le domaine des maladies cardiovasculaires chroniques, afin de déclencher une attention médicale précoce et adéquate contre les événements de décompensation.

Objectifs

L'objectif principal de cette thèse est de **proposer des méthodes d'acquisition et de traitement du signal afin d'utiliser au mieux les unités inertielles dans le suivi des patients souffrant d'insuffisance cardiaque, en exploitant efficacement les informa-**

tions multimodales provenant du CVS. Les méthodes proposées viseront l'applicabilité potentielle sur des systèmes embarqués, en tirant parti des avantages technologiques offerts par les nouvelles technologies de développement des MEMS. L'un des principaux défis identifiés dans la littérature réside dans la nature des variables physiques mesurées par les capteurs inertiels, qui sont susceptibles d'être affectées par des perturbations mécaniques associées aux conditions établies pour la mesure, ce qui gêne l'analyse correcte des principales composantes des signaux cibles [11, 27, 28]. Par conséquent, les objectifs spécifiques suivants ont été établis pour le développement de cette thèse :

1. Évaluer la faisabilité de la surveillance cardiovasculaire chronique des CVS à l'aide d'un nouveau dispositif implantable peu invasif pour l'estimation des paramètres hémodynamiques chez les patients souffrant d'insuffisance cardiaque.
2. Définir des stratégies et des méthodes qui exploitent les vastes informations multimodales des CVS dans le but d'identifier les paramètres utilisés pour estimer des marqueurs hémodynamiques.
3. Développer un système d'acquisition de signaux cardiaques qui incorpore l'utilisation de capteurs MEMS de pointe pour l'évaluation préliminaire de la détection en temps réel des événements cardiorespiratoires par l'utilisation de technologies telles que l'apprentissage automatique appliqué aux CVS.

Contenu du manuscrit

Le Chapitre 1 présente une synthèse des principales parties anatomiques et fonctions physiologiques du système cardiovasculaire dans le contexte de l'étude de l'insuffisance cardiaque. De plus, une revue de l'état de l'art des méthodes les plus pertinentes pour l'acquisition, le traitement et l'analyse des CVS est présentée.

Le Chapitre 2 décrit la caractérisation des signaux acquis lors d'une expérimentation préclinique à l'aide d'un implant gastrique pour évaluer l'hypothèse selon laquelle des CVS peuvent être captés à partir d'un petit implant de surveillance positionné au niveau du fond gastrique, car ce site anatomique semble être un bon candidat pour une surveillance cardiovasculaire à long terme, étant donné qu'il est physiquement proche du cœur. Cet implant est capable de mesurer des données cardiaques électrophysiologiques et d'accélérométrie 3D et pourrait être administré en toute sécurité à l'aide de techniques d'implantation peu invasives telles que la gastroscopie, améliorant ainsi le confort du patient et son adhésion aux traitements impliquant des dispositifs implantables. Trois versions différentes de l'implant ont été utilisées pour réaliser les expérimentations proposées, qui étaient axées sur la comparaison des signaux acquis à partir du fond de l'estomac avec les données de référence acquises par des capteurs standard du site thoracique,

et sur l'évaluation de la possibilité d'estimer les marqueurs cardiovasculaires longitudinaux à partir du site gastrique.

Les résultats obtenus ont montré que la variation temporelle des marqueurs tels que la fréquence cardiaque et la durée et l'amplitude des sons cardiaques mesurés avec l'implant étaient fortement corrélés avec les signaux de référence, ce qui est très important pour l'utilité prévue de l'implant dans la surveillance à long terme de l'insuffisance cardiaque chronique. De plus, lorsque les valeurs SNR des signaux d'accélérométrie sont supérieures à 6 dB ou que le contraste des bruits cardiaques est supérieur à 2, les composantes S1 et S2 peuvent être correctement segmentées et des marqueurs hémodynamiques peuvent être estimés à partir de ces données, ce qui prouve de manière préclinique la faisabilité d'un suivi cardiovasculaire chronique chez les patients atteints d'insuffisance cardiaque en utilisant cet implant. Cependant, le principal défi pour l'utilisation de l'implant reste l'optimisation du rapport signal/bruit, en particulier pour gérer certaines sources de bruit spécifiques au site d'acquisition gastrique qui peuvent induire des perturbations principalement dans les CVS mesurés.

Le Chapitre 3 présente le développement d'un prototype de système d'acquisition permettant de mesurer de manière synchronisée les signaux mécanocardiographiques (MCG), électrocardiographiques (ECG) et phonocardiographiques (PCG) de façon non invasive. Ce système incorpore la mesure des CVS par l'utilisation d'un capteur MEM de pointe, qui a la particularité d'intégrer un noyau d'apprentissage automatique (MLC) permettant le déploiement d'applications d'apprentissage automatique on-the-edge. Une telle propriété pose l'hypothèse que ce type de technologie pourrait être exploité pour le développement futur de dispositifs implantables ou portables pour la surveillance des patients cardiaques, avec l'avantage de permettre l'utilisation de l'apprentissage automatique on-the-edge pour améliorer l'efficacité de ces dispositifs en termes de traitement en temps réel, de vitesse, de mémoire, de taille, de consommation d'énergie et même de précision. Afin d'effectuer une première évaluation du système à la lumière de cette hypothèse, un premier groupe de tests a été réalisé pour valider la corrélation entre les signaux MCG et PCG, en prenant ce dernier comme référence gold standard, et un second groupe de tests a été développé dans le but de réaliser une évaluation préliminaire de l'hypothèse selon laquelle le MLC intégré dans le capteur MEM peut être utilisé pour détecter automatiquement des événements cardiorespiratoires liés à des variations hémodynamiques.

Les résultats obtenus ont montré des niveaux adéquats de corrélation entre les CVS mesurés et la référence PCG sur les caractéristiques de temps et de magnitude, qui sont les plus communément associées à différents types de paramètres hémodynamiques dans la littérature. De plus, une erreur de synchronisation inférieure à 2 ms entre les différents capteurs, a montré les bénéfices de l'effort particulier donné à la synchronisation temporelle correcte des signaux, acquis par différents capteurs, avec des protocoles différents et des résolutions hétérogènes. En outre, le cadre expérimental conçu pour effectuer des mesures lors de changements aigus des

paramètres hémodynamiques a permis d'obtenir des résultats de performance appropriés, avec une détection en temps réel de l'apnée avec une sensibilité, une spécificité et une précision de 0.75, 0.98 et 0.94, respectivement, et une détection en temps réel de la manœuvre de Valsalva avec une sensibilité, une spécificité et une précision de 0.70, 0.93 et 0.68, respectivement. Ces résultats démontrent la faisabilité préliminaire de la reconnaissance et de la classification de schémas associés à de multiples événements cardiorespiratoires impliquant des variations des paramètres hémodynamiques on-the-edge.

Contributions

Les principales contributions du travail développé dans cette thèse peuvent être résumées comme suit :

— La présentation des premières preuves précliniques de la faisabilité de la surveillance cardiovasculaire chronique à partir d'un dispositif cardiaque implantable peu invasif placé dans le fond de l'estomac.

— Le développement d'un système prototype spécialisé pour l'acquisition de signaux cardiaques multimodaux, qui intègre un MLC intégré dans un capteur MEM pour la reconnaissance et la classification on-the-edge de multiples événements cardiorespiratoires liés à des variations hémodynamiques.

— La proposition d'un algorithme efficace et facile à mettre en œuvre, basé sur des caractéristiques contextuelles, pour obtenir les instants de détection finale des principales composantes du CVS communément liées aux principaux sons cardiaques.

Ce travail a conduit à la publication d'un article dans le cadre d'un numéro spécial "Cardiac Vibration Signals : Old Techniques, New Tricks and Applications" dans le journal international indexé "Frontiers in Physiology" [29].

Conclusion

Le travail multidisciplinaire réalisé au cours de cette thèse ouvre des nouvelles perspectives dans l'exploitation des signaux mécaniques cardiaques pour le développement de nouveaux dispositifs permettant le suivi longitudinal de patients diagnostiqués avec une maladie cardiaque chronique, telle que l'insuffisance cardiaque. En particulier, la faisabilité d'un monitoring cardiovasculaire longitudinal à partir d'un implant gastrique innovant a été étudiée. En parallèle, nous avons réalisé un système intégrant des nouveaux capteurs à ultra-basse consommation, qui permettent un traitement et une détection on-the-edge. Ces capteurs sont particulièrement prometteurs pour une nouvelle génération de dispositifs de monitoring cardiovasculaire. Plusieurs pistes de développement futur sont évoquées.

Table of Contents

List of acronyms

ABS	Acrylonitrile Butadiene Styrene
AC	Aortic Valve Closure
ACC	Accelerometry
AO	Aortic Valve Opening
ARNI	Angiotensin Receptor/Neprilysin Inhibitor
AV	Aortic Valve
A-V	Atrioventricular
BCG	Ballistocardiogram
BNP	B-type Natriuretic Peptide
CBC	Complete Blood Count
CPP	Continuous Positive inspiratory Pressure
CRT	Cardiac Resynchronization Therapy
CVS	Cardiac Vibration Signals
DALYs	Disability-Adjusted Life Years
EA	Endocardial Acceleration
ECG	Electrocardiogram
Echo	Echocardiogram
EF	Ejection Fraction
FCG	Forcecardiography
FN	False Negative
FP	False Positive
GCG	Gyrocardiogram
HAR	Human Activity Recognition
HAT	Hardware-Attached-on-Top
HF	Heart Failure
HR	Heart Rate
HRV	Hear Rate Variability

ICD	Implantable Cardiac Device
IHD	Ischemic Heart Disease
IVC	Isovolumic Contraction
LA	Left Atrium
LV	Left Ventricle
MC	Mitral Valve Closure
MCG	Mechanocardiogram
MEMS	Micro-Electro-Mechanical Systems
MLC	Machine Learning Core
MO	Mitral Valve Opening
MRA	Mineralocorticoid Receptor Antagonist
MRI	Magnetic Resonance Imaging
MV	Mitral Valve
NT-proBNP	N-Terminal pro-BNP
PCB	Printed Circuit Board
PCG	Phonocardiogram
PEA	Peak Endocardial Acceleration
PEEK	Polyetheretherketone
PV	Pulmonary artery Valve
RA	Right Atrium
RE	Rapid Ejection
RF	Rapid Filling
RV	Right Ventricle
SCG	Seismocardiogram
SGLT2	Sodium–Glucose co-Transporter 2
SNR	Signal-to-Noise Ratio
STE	Speckle-Tracking Echocardiography
TP	True Positive
TN	True Negative
TV	Tricuspid Valve
+P	Positive Predictive Value

List of Figures

List of Tables

Introduction

Cardiovascular disease (CVD) is the leading cause of death worldwide and a major cause of disability [1, 2]. Over the last few decades, its incidence has sharply increased, where the total prevalent cases of CVD nearly doubled from 271 million in 1990 to 523 million in 2019, and the number of deaths per year increased from 12.1 million in 1990 to 18.6 million in 2019. Over this period, years lived with disability doubled from 17.7 million to 34.4 million, and disability-adjusted life years (DALYs) also increased significantly, mainly caused by ischemic heart disease (IHD) and stroke, reaching 182 million DALYs due to IHD and 143 million DALYs due to stroke. CVD also remains a leading cause of increased health care costs and premature mortality, causing 6.2 million deaths between the ages of 30 and 70 in 2019 only [3]. In a study by the European Heart Network, it was estimated that CVD cost the European Union economy €210 billion per year in 2015, of which 53% (€111 billion) resulted from healthcare costs, 26% (€54 billion) from productivity losses and 21% (€45 billion) from informal care of people with CVD [4]. These data show that the burden of CVD represents both a health and economic concern for health systems worldwide, which is expected to grow dramatically in the years ahead with the global aging of the population. Additionally, recent research associated with the COVID-19 pandemic has revealed new concerns related to CVD, involving the increased risk of poor outcomes for patients with cardiovascular risk factors and pre-existing CVD [30], the notification of patients with COVID-19 who have reported to develop cardiovascular complications in the absence of any previous history of CVD [31], and even the emergence of risks associated with vaccination against COVID-19 to develop CVD [32].

Within CVD, Heart Failure (HF) is a condition that occurs when there is an alteration in the structure or functioning of the heart, specially the left ventricle (LV). It was estimated that 64.3 million people suffered from HF worldwide in 2017, and the financial cost of HF was estimated at $30.7 billion in the U.S. in 2012, with a projection to the year 2030 revealing a likely increase in costs of 127%, i. e., $69.8 billion [5]. IHD represents one of the highest risks for developing HF, with a rate of 65% for men and 48% for women. IHD accounted for 26.5% of the global age-standardized prevalence rate of HF in 2017, being more likely to impact higher-income regions [33].

Patients suffering from chronic pathologies involving the cardiovascular system, such as HF, may benefit from a long-term remote monitoring of the main cardiovascular parameters in order to adapt their therapy in a personalized and continuous fashion and to early diagnose decompensation events that can severely damage the normal functioning of the heart [6, 7]. This

early diagnosis can significantly reduce the risk of the patient needing hospitalization, which has proven to be the main cause of increased health care costs [4]. The analysis of cardiac vibration signals (CVS), interesting sources of information about the cardiac mechanical activity, has already shown remarkable results in this context, mainly because the main components of these signals have been associated with some useful hemodynamic markers [8, 9]. Furthermore, Micro-Electro-Mechanical Systems (MEMS) sensor technology, commonly used to acquire CVS, has improved significantly during the last two decades in terms of size, cost, and resolution.

CVS may be acquired non-invasively from the chest, in a similar fashion as cardiologists apply the stethoscope for listening to the phonocardiogram (PCG) [10]. The acquisition of accelerometry signals from the chest of the patient, using in particular these MEMS devices, leads to the observation of the seismocardiogram (SCG), that is characterized by the presence of two main components, S1 and S2, which correspond to the first and second heart sounds in the PCG, respectively [27]. SCG acquisition and processing have been widely developed during the last decade, with applications ranging from IHD characterization, to cardiac stress and HF monitoring [11]. Furthermore, recent developments of wearable or connected devices offer the possibility to monitor the CVS in ambulatory monitoring [12, 13]. However, methods to obtain high-quality, chronic and longitudinal cardiac vibration data, that do not require the involvement of a medical practitioner or the patient to correctly and regularly acquire these signals, remain to be developed. Implantable systems may be a solution to this observability challenge.

Several studies have examined how accelerometric signals can be acquired to measure cardiac vibration from within the heart chambers in an invasive manner [14, 15]. These endocardial acceleration (EA) signals have two main components known as EA1 and EA2, which are associated with the first and second heart sounds, respectively. The peak-to-peak values of the main cardiac vibration components of these signals have been shown to be significantly correlated with meaningful hemodynamic markers [8, 9, 16]. Implantable cardiac devices (ICD) such as cardiac resynchronization therapy (CRT) devices, cardioverter-defibrillators and pacemakers are normally used in the treatment and follow-up of chronic heart diseases as HF. Some of these ICD already integrate accelerometer sensors to observe and analyze cardiac accelerometry signals from subcutaneous or intra-cardiac sites, with the objective to predict future HF events [17, 18] or to define automatic optimization protocols of the ICD parameters [19, 14]. Nevertheless, some of the main problems related to the use of ICD are the risks associated with the invasive procedures that must be performed to capture acceleration signals in direct contact with the heart and the risk of infection or complications of the leads [20, 21].

In past works, our team has proposed methods for the acquisition and processing of cardiac mechanical signals from accelerometers embedded into the stimulation lead of ICD [14, 15, 22]. Specifically, some of these methods have focused in extracting features from chest accelerometry signals and compare them to classical hemodynamic echocardiography markers in order to

optimize parameters of CRT devices implanted in HF patients [23, 24], considering that not all patients may benefit from an active cardiac implantable device, thus requiring the development of customized methods that can be adjusted to the needs of each patient [25, 26]. Therefore, it is clear that the development of a remote cardiac vibrations monitoring system offering integrated management of multimodal parameters with a minimally invasive device is currently needed in the chronic cardiovascular diseases domain, to trigger very early and adequate medical attention against the decompensation events.

This PhD thesis is in line with the work carried out at the *Laboratoire Traitement du Signal et de l'Image* (LTSI) for several years, in the *Stimulation thÉrapeutique et monitoring Personnalisés pour l'Insuffisance cardiaque et les Apnées-bradycardies* (SEPIA) team, on cardiac accelerometric signal processing. It is developed in a multidisciplinary environment, in collaboration with professionals from the SEPIA team and the medical device industry. More specifically, this thesis is conducted within the framework of the project entitled "Digital Implantable Gastric Stethoscope (DIGS)" of the Agence Nationale de la Recherche (ANR) [34], which is developed in direct collaboration between LTSI, the *Recherche Translationnelle et Innovation en Médecine et Complexité* (TIMC) team, the company *Sentinhealt* and the *Laboratoire Radiopharmaceutiques Biocliniques INSERM U1039* (LRB). The main objective of this project is to validate a data extraction process for early detection of HF decompensation in real-life conditions. This project can have economic benefits through the potential transfer of the developed technologies to the industrial partners that have been working for several years with the SEPIA team in this field.

The **main objective** of this thesis is to further investigate in this domain and, in particular, **to propose signal acquisition and processing methods to make the best use of inertial units in the monitoring of patients with heart failure, by efficiently exploiting multimodal information from CVS**. The proposed methods will target the potential applicability on embedded systems, leveraging the technological advantages offered by new technologies in MEMS development. One of the main challenges previously identified in the literature lies in the nature of the physical variables measured by inertial sensors, which are susceptible to be affected by mechanical disturbances associated with the conditions established for the measurement, thus hindering the correct analysis of the main components of the target signals [11, 27, 28]. Therefore, the following specific objectives have been established for the development of this thesis:

1. To evaluate the feasibility of chronic cardiovascular monitoring of CVS using a novel minimally invasive implantable device for the estimation of hemodynamic parameters in HF patients.
2. To define strategies and methods that leverage the vast multimodal information of CVS in the task of identifying the parameters used to estimate hemodynamic markers.
3. To develop a cardiac signal acquisition system that incorporates the use of cutting-edge, ultra-low-power MEMS sensors for the preliminary evaluation of real-time detection of

cardiorespiratory events through the use of technologies such as machine learning applied on CVS.

Figure 1 shows a general outline of the study framework of the thesis, which is intended to fulfill the proposed objectives. This framework is divided into two main approaches, one of them focused on the evaluation of the feasibility of acquiring longitudinal CVS using an intra-gastric implant in a preclinical animal experimentation setup. The second approach focuses on the development of a cardiac signal acquisition system to preliminarily assess the feasibility of automatically detecting cardiorespiratory events on-the-edge using a MEMS sensor with an embedded machine learning core. Note that although the content of the green box in Figure 1 is outside the scope of this thesis, it is a good representation of the research intended to be developed as future work, based on the results obtained with the development of this thesis.

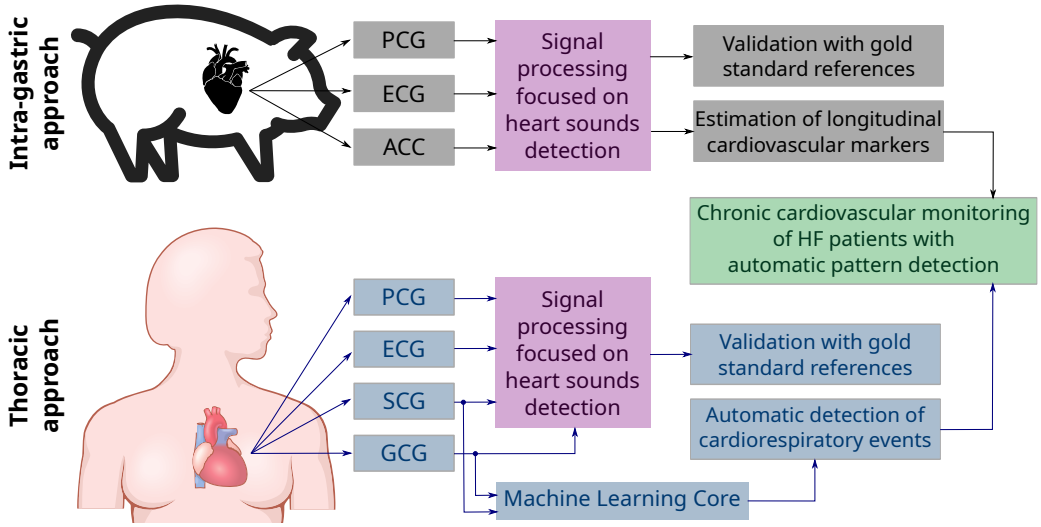

Figure 1 – General outline of the thesis study framework. The black arrows represent the flow of data through the intragastric approach, while the blue arrows represent the flow of data through the non-invasive, thoracic approach. The gray, purple and blue boxes are distributed according to their relationship to the first, second and third specific objectives of the thesis, respectively. The green box represents the intended purpose of the research subsequent to the completion of this thesis. The acronyms ECG, PCG, ACC, SCG and GCG stand for Electrocardiogram, Phonocardiogram, Accelerometry, Seismocardiogram and Gyrocardiogram, respectively; referring to the signals acquired for each of the approaches.

This thesis is organized as follows:

Chapter 1 presents an overview of the main anatomical parts and physiological functions of the cardiovascular system in the study context of HF. In addition, a state-of-the-art review of the most relevant methods for the acquisition, processing and analysis of CVS is presented.

Chapter 2 discusses the hypothesis that CVS may be captured from a small monitoring implant positioned at the gastric fundus, which could be delivered through gastroscopy, in a minimally invasive manner. It describes the characterization of the acquired signals in pre-

clinical experimentation and evaluates the feasibility to obtain useful hemodynamic markers from these signals.

Chapter 3 describes the design, calibration, operation and initial evaluation of a prototype acquisition system developed to measure the mechanical, electrical and phonographic signals of the heart using specialized sensors with high performance characteristics. The main feature of such a system is the integration of a machine learning core (MLC) that is intended to be used to automatically detect different cardiorespiratory events capable of generating hemodynamic variations, such as apnea and valsalva maneuver.

Chapter 4 presents the final conclusions and possible directions for future work, based on the results obtained with the development of this thesis.

Chapter 1

Fundamentals of cardiac function and cardiac vibration signals

The function of blood circulation is to meet the needs of body tissues by transporting oxygen, nutrients and hormones, removing waste products, and maintaining an appropriate environment in all tissue fluids of the body for optimal cellular functioning. The blood vessels and heart are controlled to provide the blood pressure and cardiac output necessary to cause blood flow through the tissues, since the local blood flow velocity is determined primarily by the nutritional needs of each type of tissue [35]. This chapter presents an overview of the main anatomical parts and physiological functions of the cardiovascular system in the study context of heart failure (HF). In addition, a state-of-the-art review of the most relevant methods for the acquisition, processing and analysis of cardiac vibration signals (CVS) is presented.

1.1 The cardiovascular system

Blood circulation occurs through an extensive system that can be roughly summarized as a pump represented by the heart and a network of tubes corresponding to the arteries, veins and capillaries. This complex anatomical structure is the cardiovascular system. The blood circulation process is divided into two parts known as the pulmonary circulation and the systemic circulation. The pulmonary circulation corresponds to the process in which oxygen-poor blood flows through the lungs to be oxygenated, while the systemic circulation is the flow of blood through the other tissues of the body to perform the exchange between oxygen and carbon dioxide, which is the process known as perfusion [35].

Figure 1.1 shows a representation of the cardiovascular system and the circulatory flow direction. The total amount of blood is distributed in different percentages among the different parts of the cardiovascular system. The systemic circulation concentrates the largest amount of blood (84%), where 13% is in the arteries that are responsible for carrying blood to the tissues at high pressure, 7% is in the arterioles (small branches of the arterial system) and capillaries, which perform the exchange of liquids, nutrients, electrolytes, hormones and other substances

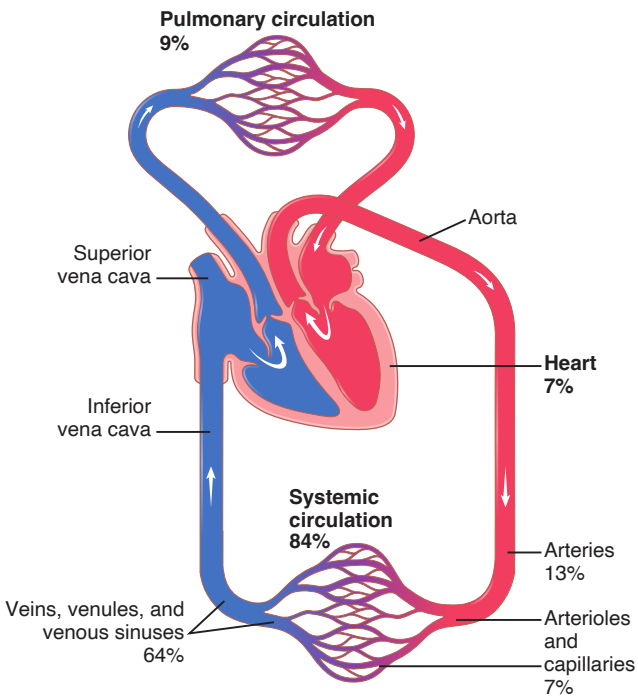

Figure 1.1 – Representation of the cardiovascular system with percentage of total blood distribution. Adapted from [35] with permission, copyright ©2015 Elsevier.

between the blood and the cells of the different tissues, and 64% is concentrated in the venous system, which is in charge of collecting blood from the tissues to transport it back to the heart at low pressure. The remaining percentage of blood is distributed between the heart (7%) and the pulmonary circulation (9%) [35].

1.1.1 The Heart

The mediastinum is the area between the two pleural sacs (sacs containing the lungs), extending vertically from the diaphragm to the thoracic inlet and bounded posteriorly by the thoracic vertebral column and anteriorly by the sternum. The heart is located in the middle mediastinum in an oblique position with respect to the planes of the body. It is surrounded by a double-walled sac called pericardium, which offers protection and stability. The heart has a base and an apex, and its surfaces are referred to as diaphragmatic (inferior), sternocostal (anterior) and right and left (pulmonary). The position of the heart in the thorax can be compared to a deformed pyramid, with the apex facing anteriorly and to the left and the base facing posteriorly and to the right [36].

The heart is an anatomical fusion of two muscular pumps that make blood flow in series. These two pumps are known as the “right heart”, in charge of pulmonary circulation, and the “left

heart", in charge of systemic circulation [36]. In turn, both the right and left heart are divided into two chambers called atrium and ventricle. The atria are responsible for collecting blood from the veins and pumping it to the ventricles in a weak preparatory action, while the ventricles, larger and stronger than the atria, are responsible for supplying the main pumping force to the pulmonary circulation (right ventricle) and the systemic circulation (left ventricle) through the arteries. The correct direction of blood flow in the heart is ensured by the presence of four valves corresponding to two atrioventricular valves and two semilunar valves. The atrioventricular (A-V) valves, defined as the tricuspid valve (TV) in the right heart and the mitral valve (MV) in the left heart, prevent blood flow from the ventricles to the atria. The semilunar valves prevent the backflow of blood from the arteries into the ventricles and correspond to the pulmonary artery valve (PV) in the right heart and the aortic valve (AV) in the left heart [35]. All the anatomical parts of the heart described above can be seen in Figure 1.2.

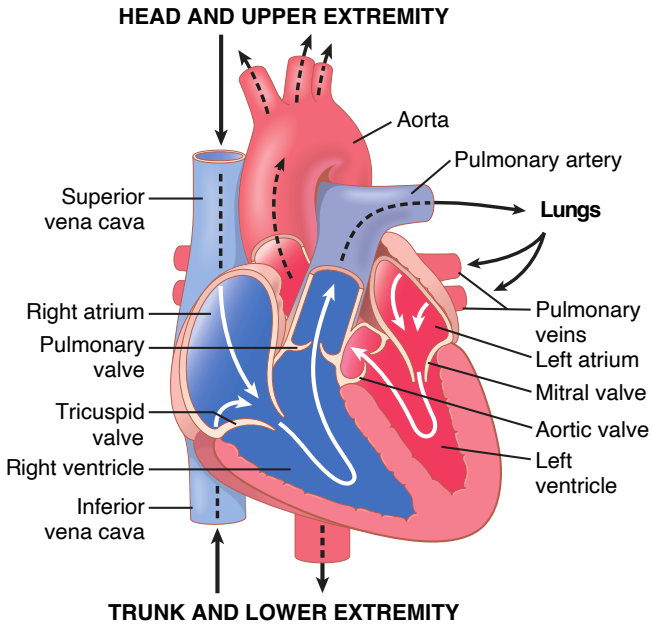

Figure 1.2 – Anatomy of the heart. The white arrows show the direction of blood flow within the heart while the black arrows show the direction of blood through the major blood vessels. Adapted from [35] with permission, copyright ©2015 Elsevier.

1.1.2 The major blood vessels

The thoracic aorta and its branches, the pulmonary artery, and the inferior and superior vena cava are the main blood vessels. They are also shown in Figure 1.2. Blood reaches the right heart through the superior and inferior vena cava, where the superior vena cava is approximately 7 cm long and returns blood to the heart from the tissues above the diaphragm, while the inferior vena

cava carries blood to the right atrium (RA) from the infradiaphragmatic tissues. The pulmonary artery, measuring approximately 5 cm in length and 3 cm in diameter, transports deoxygenated blood from the right ventricle (RV) to the lungs. The blood is oxygenated again in the lungs and returns to the heart in the left atrium (LA) through the pulmonary veins. Blood previously oxygenated is propelled out of the heart through the aorta, which is described in three stages: (1) the ascending aorta, 5 cm long, originates at the base of the left ventricle (LV) and ascends obliquely, curving anteriorly and to the right, (2) the aortic arch surrounds the pulmonary artery from the front to the back, featuring some branches that carry oxygenated blood to the head and upper extremities, and (3) the descending aorta is the segment located in the posterior mediastinum, descending to carry oxygenated blood to the trunk and lower extremities [36].

1.1.3 Normal cardiac function

The heart has an advanced system for rhythmic self-excitation that generates periodic electrical impulses which initiate contraction of the heart muscle and spread rapidly and synchronously through all the conductive tissues of the heart. Under normal operating conditions, the atria contract approximately 170 ms before the ventricles, allowing for better filling of the ventricles before pumping blood through the pulmonary and peripheral circulation. The simultaneous contraction of all parts of the ventricles is of utmost importance to ensure the proper functioning of this process, since the thrust force generated to push the blood through all the tissues of the body depends on it [35]. The main conductive tissues of the heart and their anatomical disposition are shown in Figure 1.3. These tissues are responsible for generating and controlling the rhythmic functioning of the heart.

Rhythmic activation of the heart

The electrical impulse that initiates the rhythmic functioning of the heart starts in the sinus node under normal conditions. This node controls the rate of beat of the entire heart and is located in the upper wall of the RA, just below the opening of the superior vena cava, and is approximately 15 mm long, 3 mm wide and 1 mm thick. The ends of the sinus node fibers connect directly with the surrounding atrial muscle fibers, causing the action potential to propagate throughout the atrial muscle mass to make it contract. The impulse generated by the sinus node is conducted to the atrioventricular (A-V) node through the internodal pathways located in the walls of the RA, where the electrical impulse is delayed to allow the atria to contract properly before the impulse reaches the ventricles. The A-V node is located in the posterior wall of the RA, just behind the tricuspid valve. Subsequently, the electrical impulse reaches the A-V bundle (also known as the bundle of HIS), where it splits to flow through the right and left bundle branches, connected to the right and left ventricle, respectively. The right and left bundle branches spread through the ventricles via small specialized fibers known as

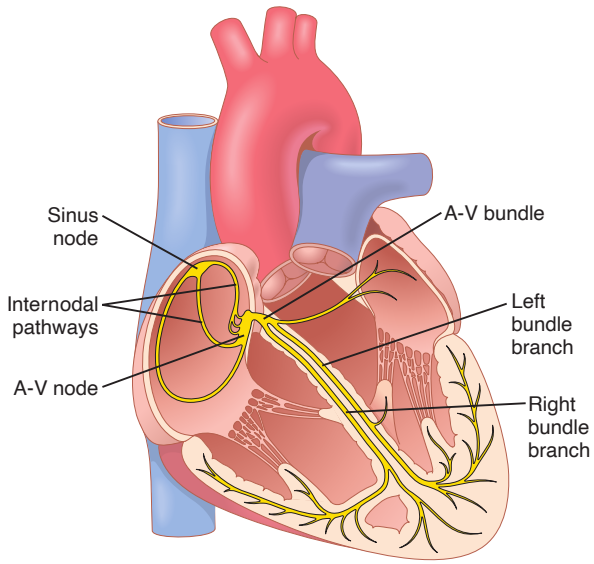

Figure 1.3 – Anatomical distribution of the main conductive tissues of the heart. Reprinted from [35] with permission, copyright ©2015 Elsevier.

Purkinje Fibers. These fibers exhibit rapid action potential conduction causing the muscle mass of the ventricles to contract almost simultaneously to achieve the higher pressure that ejects the blood from the heart [35].

Phases of the cardiac cycle

A cardiac cycle corresponds to the set of consecutive events that occur from the beginning of one heartbeat to the beginning of the next one. The cardiac cycle is divided into two main phases related to the filling and ejection processes of the ventricles of the heart, where the ventricular filling process is called diastole and the ventricular contraction is referred to as systole [36]. The systole phase begins with contraction of the ventricles leading to A-V valves closure. The short time period between the closing of the A-V valves and the opening of the semilunar valves is called isovolumic contraction because the volume of blood in the ventricles does not change even though ventricular contraction has already begun. Blood is ejected out of the ventricles until the semilunar valves close, terminating the systole phase. The diastole phase begins with the closure of the semilunar valves and, as in systole, there is a short period of time until the A-V valves open, in this case it is called isovolumic relaxation. Once the A-V valves open due to ventricular relaxation, blood begins to fill the ventricles suddenly, which is known as rapid inflow. Before the end of the systole phase, the atria contract slightly (atrial systole) to help ventricles fill completely and thus end the diastole phase with the closing of the A-V valves so that the cycle repeats again [35].

Cardiovascular hemodynamics

The characterization and analysis of flowing blood through the cardiovascular system is known as hemodynamics [37]. The main variables that define cardiovascular hemodynamics are pressure, flow and resistance, from which quantitative and measurable parameters such as blood pressure, stroke volume, ejection fraction and cardiac output are derived. The blood flow $\boldsymbol{F}$ through a blood vessel is determined by the pressure difference $\Delta\boldsymbol{P}$ between the two ends of the vessel and the resistance $\boldsymbol{R}$ or opposition to blood flow that occurs within the vessel due to friction between the blood and the vessel walls. This relationship is represented by Equation (1.1), well known as *Ohm's Law* [35].

$$\boldsymbol{F} = \frac{\Delta\boldsymbol{P}}{\boldsymbol{R}} \tag{1.1}$$

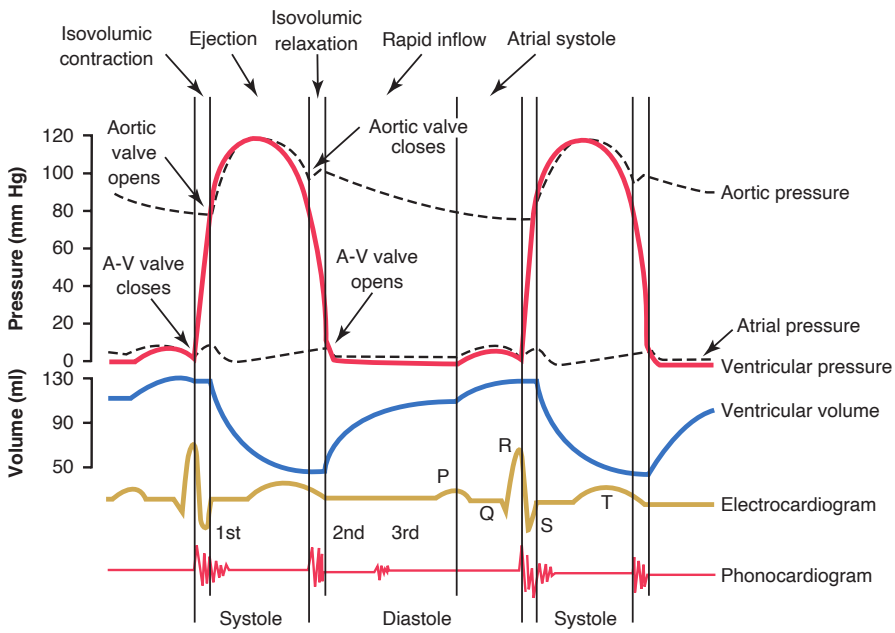

Figure 1.4 – Cardiac cycle events for left ventricular function, showing the evolution of the main hemodynamic parameters, the electrocardiogram and the phonocardiogram. Adapted from [35] with permission, copyright ©2015 Elsevier.

Figure 1.4 shows the evolution of the typical hemodynamic parameters of the left heart during a normal cardiac cycle, pointing out the main cardiac events previously described. **Blood pressure** is the force that blood exerts over any unit area of the vascular walls and is typically measured in millimeters of mercury (mm Hg). This unit of measurement has a historical origin dating back to 1846, when Jean-Léonard-Marie Poiseuille invented the mercury manometer, which was established as the standard reference for blood pressure measurement [35]. **Stroke volume** is defined as the volume of blood that is ejected by the contraction of the LV in one

cardiac cycle. It is calculated based on the velocity of blood flowing from the LV into the aorta and has a typical value of 70 ml. **Ejection fraction** (EF) refers to the percentage of blood that is ejected from the LV (stroke volume) in relation to the total blood volume that was in this ventricle at the end of the diastole phase. In general, a normal EF is approximately 60%. **Cardiac output** is basically defined as the amount of blood pumped by the heart in one minute. This is calculated by multiplying the stroke volume and heart rate to obtain a result typically reported in L/min, with typical values ranging from 5 to 6 L/min at rest [35].

1.1.4 Methods and tools for cardiac monitoring

Throughout history, different methods and tools have been developed for monitoring the state and functioning of the heart. Figure 1.4 also shows the depiction throughout the cardiac cycle of two of the most well-known and widely used techniques in the medical field for cardiac analysis (the electrocardiogram and the phonocardiogram). Although there is a wide variety of tools developed for this purpose, all of them can be classified according to the physical nature of the variable they measure and the level of invasiveness required for their use. The following is a description of some of the most common noninvasive techniques that represent a gold standard reference for cardiac monitoring due to their extensive study in the literature and their acceptance by the medical field in the context of this thesis.

Electrocardiogram (ECG)

An ECG records the electrical current that spreads to the surface of the body from the electrical impulse that makes the heart work. This phenomenon occurs because the electrical current that activates the heart muscle spreads through the surrounding tissues until reaching the body surface, thus it can be measured by using two electrodes attached to the skin on opposite sides of the heart [35]. Figure 1.5 shows a normal ECG highlighting the main waves and segments that compose it with detailed views of their duration and typical amplitude.

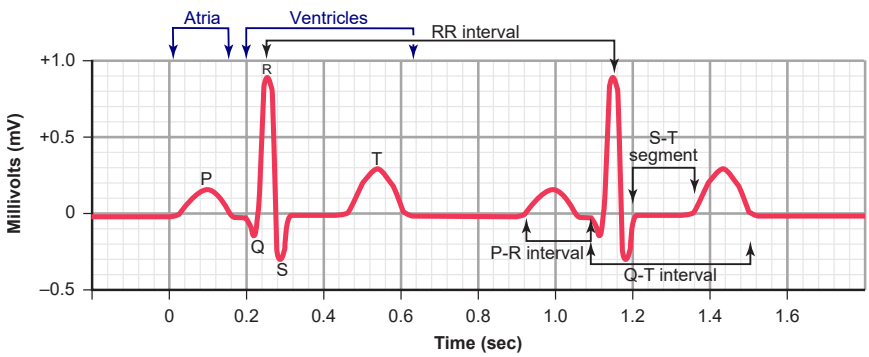

Figure 1.5 – Example of a normal ECG. Adapted from [35] with permission, copyright ©2015 Elsevier.

The normal ECG is composed of 5 main waves classified as depolarization waves and repolarization waves. The P wave is the first one displayed on the ECG and is generated by the depolarization of the atrial cells prior to atrial contraction. This wave has a typical duration of approximately 110 ms and an amplitude between 0.1 and 0.3 mV. The Q, R and S waves are generated by the electrical potentials associated with the depolarization of the ventricular cells prior to ventricular contraction and are usually grouped into a single ECG component called the QRS complex. The QRS complex presents the greatest amplitude in the ECG with about 1.0 to 1.5 mV and an approximate duration of 120 ms. Finally, the T wave is generated by the repolarization of the ventricles, which is a slower process with a smaller amplitude and longer duration in the ECG. The T wave has a duration of approximately 150 ms and an amplitude between 0.2 and 0.3 mV [38]. Figure 1.6 shows the relationship between the electrical potential in the conductive tissues of the heart and the different components of the ECG.

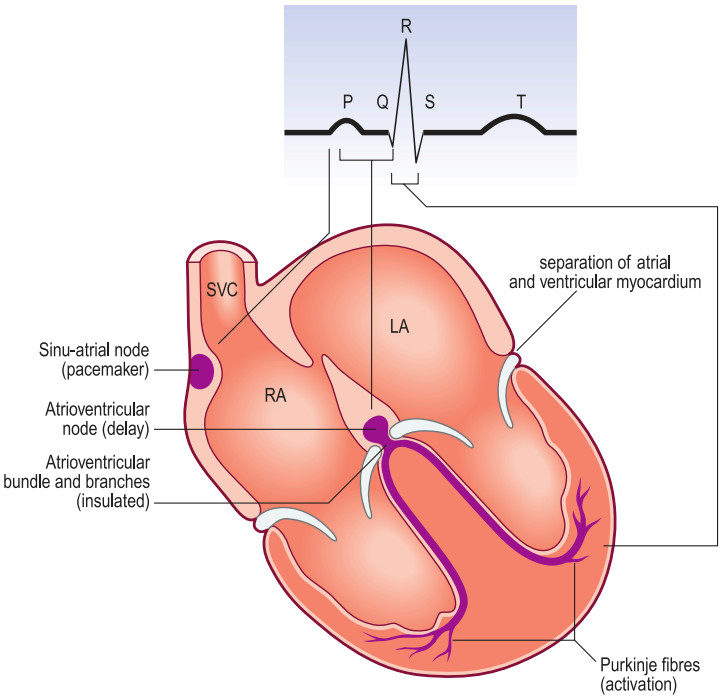

Figure 1.6 – Basic representation of the conduction system of the heart and its relationship with the ECG. Adapted from [36] with permission, copyright ©2016 Elsevier.

The repolarization of the atria occurs at the same time as the QRS complex, but since the QRS complex has a greater amplitude, it obscures the atrial repolarization wave, which is not reflected in the ECG. It is worth mentioning that the amplitude values in the ECG strongly depend on the location of the electrodes at the moment of measurement, and the values described here correspond to the ECG recorded with electrodes on both arms or on one arm and one leg, which is one of the most commonly used configurations [35].

Phonocardiogram (PCG)

The rapid closing and opening actions of the different cardiac valves generate sound signals that can be detected by the human ear, especially through the use of the traditional stethoscope [39], or recorded electronically by using a specialized microphone. The recording of these audio signals is referred to as PCG and is displayed as waves with different frequency levels. Figure 1.7 shows examples of PCG acquired under normal heart function conditions and under the influence of some cardiac pathologies. One of the main advantages of the PCG is that it can detect frequency bands that are not audible to the human ear, especially in the low frequency spectrum. The frequency band of heart sounds that can be detected by the human ear is between approximately 40 and 500 Hz, but a large part of the content of these signals is below that range, where even the highest energy peak is around 20 Hz [35].

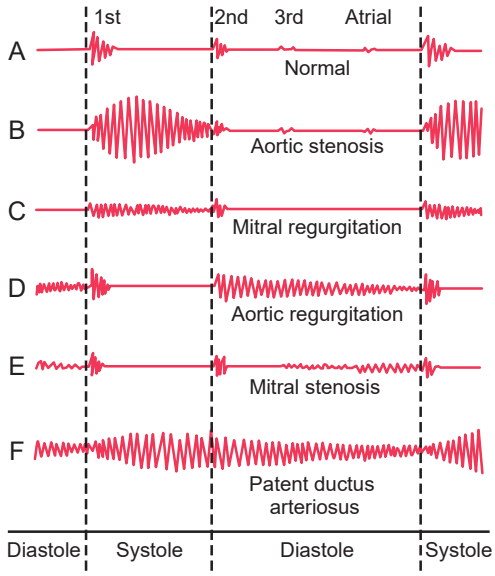

Figure 1.7 – Examples of PCG recordings from normal and abnormal hearts. Reprinted from [35] with permission, copyright ©2015 Elsevier.

There are two main components that can be visualized in a normal PCG called the first and second heart sounds, which are respectively associated with the typical "lub, dub" heard through the stethoscope. The first sound is produced mainly by the closure of the A-V valves at the beginning of the systole stage, and the second sound is generated by the closure of the semilunar valves at the end of systole. The typical duration of the heart sounds is 140 ms for the first sound and 110 ms for the second sound, and the second sound has slightly higher frequency components than the first sound. These discrepancies in the duration and composition of the two sounds are mainly due to the differences in tension and elasticity of the A-V valves compared to the semilunar valves. The different components of the PCG can be accentuated depending on

the location of the microphone on the chest. Figure 1.8 shows typical locations for emphasizing different cardiac phenomena during auscultation.

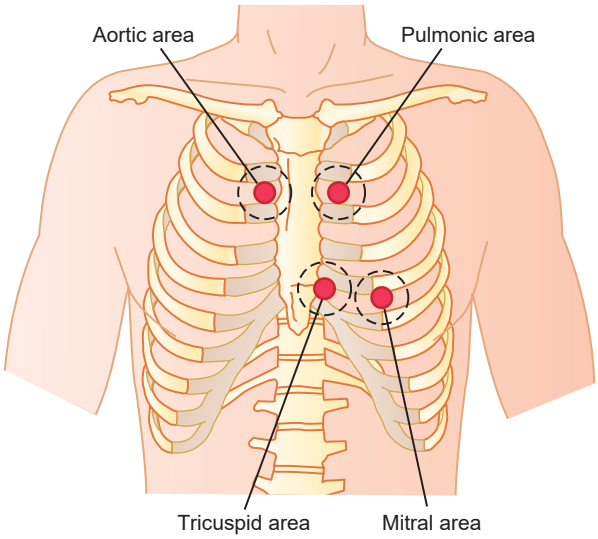

Figure 1.8 – Typical locations for cardiac auscultation. Reprinted from [35] with permission, copyright ©2015 Elsevier.

In some cases it is also possible to identify a third and fourth sound in the PCG with a weaker amplitude compared to the first two sounds (see Figure 1.7). The third sound occurs in the middle third of diastole and may be associated with the oscillatory movement of blood entering the ventricles, although some studies have also associated this sound with the occurrence of cardiac pathologies [40, 41]. The fourth sound appears right at the end of diastole and is caused by atrial contraction that generates a greater inflow of blood into the ventricles. When this sound becomes louder it may be associated with impaired ventricular filling that requires greater atrial contraction, which is why it tends to be more noticeable in older adults with left ventricular hypertrophy [35].

Echocardiogram (Echo)

Echocardiography is a method of cardiac monitoring that uses ultrasound waves from a transducer placed on the chest wall (transthoracic configuration) or passed into the esophagus of the patient to perform a detailed analysis of the anatomy of the heart. An echocardiogram is presented as a grayscale image created from a complex analysis and processing of the ultrasound waves that are reflected and backscattered by the different cardiac tissues on which the signal is focused [42]. The grayscale of the image indicates the intensity of the reflected ultrasound, where highly reflective structures, such as calcifications in the heart valves or pericardium, appear white, while fluid or blood appears black as it presents the least reflection of the ultrasound

waves. Muscle tissue such as the myocardium, which forms the middle and thickest layer of the heart wall, appears more gray and shows a unique speckle pattern [43]. The Echo allows detailed evaluation of the cardiac anatomy from three standardized planes shown in Figure 1.9. The four-chamber plane (Figure 1.9a) provides a clear view of the atria, ventricles, and the mitral and tricuspid valves. The long-axis plane (Figure 1.9b) is generated by placing the transducer in the left apicosternal position and allows detailed visualization of the mitral and aortic valves, left atrium, left ventricle and aorta. The short-axis plane (Figure 1.9c) is obtained by rotating the transducer 90° in a dextrorotatory direction and provides a detailed view of the chordae tendineae, papillary muscles, aortic valve and left atrium [36].

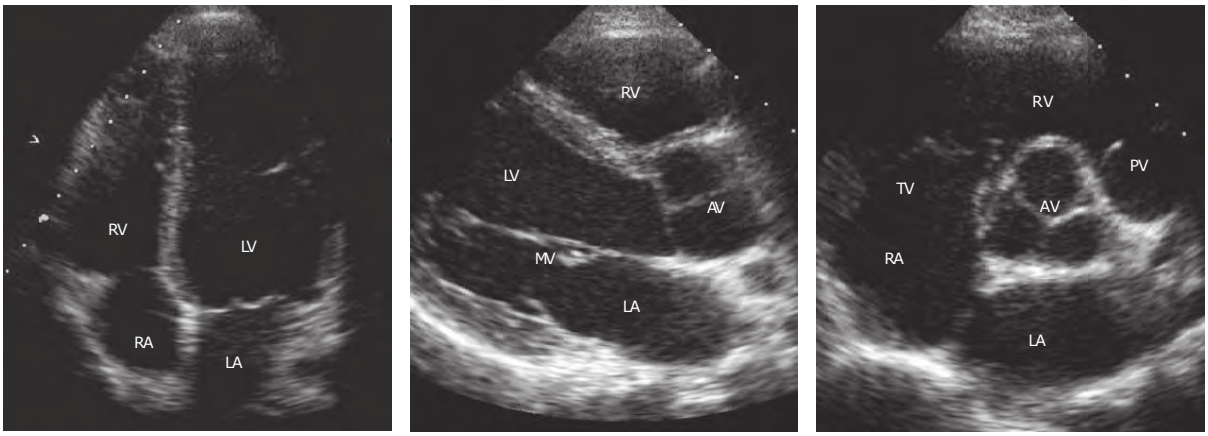

(a) Four-chamber view (b) Parasternal long-axis view (c) Short-axis view at AV level

Figure 1.9 – Cardiac anatomy shown by transthoracic echocardiography. Adapted from [36] with permission, copyright ©2016 Elsevier.

Considering the great detail that Echo can provide for the analysis of cardiac anatomy, even offering real-time visualization with recent technological advances, this technique has become the gold standard reference for the measurement of some hemodynamic cardiac parameters such as stroke volume, cardiac output and left ventricular EF. The Echo allows measurement of the velocity of blood flowing from the left ventricle into the aorta and the cross-sectional area of the aorta, from which the stroke volume can be calculated. In the same manner, the cardiac output can also be obtained by multiplying the stroke volume by the heart rate and the EF by measuring the left ventricular volume at the beginning and ending of the systole phase [35]. Although these hemodynamic parameters have great diagnostic utility for the evaluation of cardiac function, left ventricular function is a complex event that is partially described by clinical measures of diastolic filling and qualitative changes in regional wall motion [42]. For this reason, innovative techniques have been developed that make use of Echo technology to measure myocardial deformation, also known as strain.

Strain measurement by speckle-tracking echocardiography (STE) is an established echocar-

diographic modality for real-time quantitative assessment of myocardial function with clinical applications in the diagnosis and prognosis of many cardiac diseases [44, 45]. STE is based on tracking the movement of small bright spots (speckles) of the myocardium captured in the Echo image during the cardiac cycle. The ultrasound system tracks speckles between consecutively acquired Echo images and determines the distance between two defined myocardial region markers to plot this distance along the cardiac cycle. Thus, STE provides a direct and accurate measurement of myocardial strain from the three directions established for such analysis: the longitudinal direction (from the base of the heart towards the apex), the radial direction (walls thicken), and the circumferential direction (cavity size) [46]. Myocardial strain is a dimensionless measure that describes the fractional change in the length of a myocardial segment, reported as a positive or negative percentage with typical values defined by the European Association of Cardiovascular Imaging in the range of -20% (peak global longitudinal strain) in a healthy person measured by transthoracic echocardiography, with less negative values considered abnormal [47].

Echo has become one of the main techniques for the evaluation of cardiac function due to its diagnostic capability and the wide variety of parameters it can measure. However, one of its main limitations for use as a long-term monitoring method lies in the physical and technical characteristics of the equipment used. Typical echocardiographic equipment is often large, bulky, and expensive, which has long limited its exclusive use within medical facilities. Nevertheless, technological advances over the past decade have enabled the development of smaller ultrasound machines that can even be portable. These machines can provide diagnostic-quality images and are relatively inexpensive, but currently lack full diagnostic capabilities, always requiring an experienced operator, such as a cardiologist, to take advantage of their full potential [43].

1.2 Heart failure (HF)

Cardiovascular disease (CVD) is the leading cause of death worldwide and a major cause of disability [3], and HF is a condition within CVD that occurs when there is an alteration in the structure or functioning of the heart, reducing the ability of the heart to pump enough blood to meet the requirements of the body [43]. Although historically there has been a debate to establish a mechanistic definition for HF, in 2021, the leading medical and scientific bodies of the world proposed a consensus on a universal definition and classification of HF [48]. It was established that *"HF is a clinical syndrome with symptoms and or signs caused by a structural and/or functional cardiac abnormality and corroborated by elevated natriuretic peptide levels and/or objective evidence of pulmonary or systemic congestion"*, and classified HF in three different categories based on the left ventricular EF: HF with reduced EF ($\leq 40\%$), mildly reduced EF ($41 - 49\%$) and preserved EF ($\geq 50\%$).

1.2.1 Etiology

The etiology of HF refers to the different causes that can lead to the development of this disease, and it is easy to deduce that there are many conditions that can drive a patient to develop HF considering the large number of pathologies that can generate an impairment of LV function or structure. Some of these causes are listed below, bearing in mind the left ventricular EF [43].

Reduced EF ($\leq 40\%$)

- Ischemic heart disease
  - Myocardial infarction
  - Myocardial ischemia
- Chronic pressure overload
  - Hypertension
  - Obstructive valvular disease
- Chronic volume overload
  - Regurgitant valvular disease
  - Intracardiac (left-to-right) shunting
  - Extracardiac shunting
- Chronic lung disease
  - Cor pulmonale
  - Pulmonary vascular disorders
- Nonischemic dilated cardiomyopathy
  - Familial/genetic disorders
  - Infiltrative disorders
- Toxic/drug-induced damage
  - Metabolic disorder
  - Viral
- Chagas disease
- Disorders of rate and rhythm
  - Chronic bradyarrhythmias
  - Chronic tachyarrhythmias

Mildly reduced EF ($41 - 49\%$)

- Pathologic hypertrophy
  - Primary (hypertrophic cardiomyopathies)
  - Secondary (hypertension)
- Aging
- Endomyocardial disorders
- Restrictive cardiomyopathy
  - Infiltrative disorders (amyloidosis, sarcoidosis)
  - Storage diseases (hemochromatosis)
- Fibrosis

Preserved EF ($\geq 50\%$)

- Metabolic disorders
  - Thyrotoxicosis
- Nutritional disorders (beriberi)
- Excessive blood flow requirements
  - Systemic arteriovenous shunting
  - Chronic anemia

1.2.2 Diagnosis

HF can be easily diagnosed when there are evident symptoms that have been documented in relation to this cardiac condition, and even more when the patient presents risk factors that can help to guide the diagnostic process. However, it has always been emphasized that the best way to make an accurate diagnosis is to maintain a high suspicion index, because the symptoms of HF are often non-specific and non-sensitive. There are several standardized procedures that should be followed in order to determine an accurate diagnosis when HF is suspected. These procedures range from a detailed physical examination to the use of laboratory tests for patients with high risk factors [43].

Physical examination

When HF is suspected, the first step in making a diagnosis is to perform a physical examination to estimate the cause and severity of the disease. Respiratory distress at rest is one of the main signs of severe HF, as the patient feels the need to sit upright and is unable to finish a sentence without feeling suffocated. In the case of moderate HF, the patient does not suffer respiratory complaints at rest but may feel discomfort in breathing if he/she remains lying down for several minutes. Similarly, systolic blood pressure is also determined as a sign of interest since it is reduced in patients with advanced HF due to severe deterioration of left ventricular function [43].

Other factors that may help to identify HF in patients are the elevation in jugular vein pressure that provides information on right atrial pressure, the detection of pulmonary rales caused by the accumulation of fluids in the lung tissues, the audible detection of a third heart sound that may be related to volume overload in patients with tachycardia or tachypnea, an enlargement of the liver as a consequence of increased pressure in the hepatic veins, the appearance of edema in the lower extremities due to right ventricular malfunction, and finally, considerable weight changes of the patient as a consequence of severe HF [43].

Standard validation exams

Detection of HF-associated biomarkers is performed by conducting routine laboratory tests such as complete blood count (CBC), urinalysis, serum creatinine, blood urea nitrogen, and electrolyte panel, among other specific tests for selected patients. The main biomarkers that these tests seek to analyze and that constitute useful tools for the diagnosis of HF are circulating levels of natriuretic peptides such as B-type natriuretic peptide (BNP) and N-terminal pro-BNP (NT-proBNP). These biomarkers are released by the failing heart. Other biomarkers that have been recently being used in this context are galectin-3 and soluble ST-2 [43].

It is always recommended to record a 12-lead ECG to identify important factors such as

left ventricular hypertrophy or alterations in the Q wave that may indicate a prior myocardial infarction. In the case of a normal ECG, left ventricular malfunction can be discarded. In addition, further details can be obtained to improve diagnostic certainty by performing other exams such as a thoracic x-ray to obtain information about the shape and size of the heart and to rule out other non-cardiac conditions that may be causing the symptoms in the patient. Regarding noninvasive cardiac imaging methods for the evaluation and diagnosis of HF, 2D Doppler echocardiography represents the most useful method to obtain accurate information on the shape, size and function of the different cardiac chambers and valves, considering also that it allows the measurement of the left ventricular EF, which is one of the most relevant hemodynamic parameters in the analysis of HF. Magnetic resonance imaging (MRI) is also used to analyze the cardiac anatomy and physiology, representing the gold standard for the evaluation of ventricular mass and volume, despite its reduced implementation compared to other techniques, especially due to its high economic cost and long acquisition time [43].

1.2.3 Left-sided and right-sided HF

HF can be classified according to the side of the heart that is affected by the disease, in which case it is referred to as left-sided HF and right-sided HF. Although left-sided HF is statistically more common than right-sided HF, it is important to consider the different pathophysiologies associated with each classification. Left-sided HF appears through the backup of blood in the pulmonary circulation caused by the inefficiency of the left ventricle to eject blood, resulting in the accumulation of blood in the lungs and the increase in pulmonary artery pressure leading to pulmonary vascular congestion and pulmonary edema. On the other hand, right-sided HF is presented by the backup of blood in the systemic circulation because the right ventricle fails to send to the lungs the same amount of blood that arrives from the venous system, thus generating an increase in central venous pressure that leads to the accumulation of fluids in places such as the feet, legs and organs such as the liver and kidneys [35].

1.2.4 New York Heart Association Classification

The functional status of patients is an extremely important marker for determining an appropriate prognosis for the level of medical care and treatment required by each patient. The New York Heart Association developed a classification system related to this aspect that allows patients to be easily classified according to their functional capacity. Table 1.1 shows the characteristics of this classification. Although it is still difficult to determine a precise prognosis of the possible evolution of the patient's condition, this classification has shown a high efficacy in this task, since statistically it has been found that, for instance, patients with Class IV characteristics have a higher annual mortality rate (between 30 and 70%) than Class II patients (between 5 and 10%). This type of classification seeks to address the results of mortality studies in the HF

community, which indicate that 30 to 40% of patients die within the first year of diagnosis and 60 to 70% die within five years, mainly from worsening of the HF due to inadequate treatment [43].

Functional capacity	**Objective assessment**
Class I	Patients with cardiac disease but without resulting limitation of physical activity. Ordinary physical activity does not cause undue fatigue, palpitations, dyspnea, or anginal pain.
Class II	Patients with cardiac disease resulting in slight limitation of physical activity. They are comfortable at rest. Ordinary physical activity results in fatigue, palpitation, dyspnea, or anginal pain.
Class III	Patients with cardiac disease resulting in marked limitation of physical activity. They are comfortable at rest. Less than ordinary activity causes fatigue, palpitation, dyspnea, or anginal pain.
Class IV	Patients with cardiac disease resulting in inability to carry on any physical activity without discomfort. Symptoms of heart failure or the anginal syndrome may be present even at rest. If any physical activity is undertaken, discomfort is increased.

Table 1.1 – New York Heart Association classification for HF [43].

1.2.5 Compensated and decompensated HF

When a sudden event occurs that can severely damage the normal functioning of the heart, such as a heart attack, it results in an immediate reduction in cardiac output and pooling of blood in the venous system, leading to an increase in central venous pressure. The black line in Figure 1.10 depicts the progression in cardiac output following an event such as an acute myocardial infarction. Point A shows the normal state of blood circulation under resting conditions, where cardiac output is 5 L/min and right atrial pressure is 0 mm Hg. Point B illustrates cardiac performance just a few seconds after infarction occurs, with a sharp drop in cardiac output that usually produces fainting. Point C represents the compensation of cardiac output as a response of the sympathetic nervous system, which occurs mainly within the first 30 seconds to 1 minute after the heart attack. Finally, point D shows a recovery of cardiac output to near-normal function at rest that occurs after several days or even weeks, where an increase in right atrial pressure can be noted, mainly caused by fluid retention generated during the abnormal cardiac event. This final stage of the process is known as compensated HF, where the patient presents a positive recovery but the symptoms of acute HF may still reappear depending on the lifestyle of the patient [35].

The state of compensated HF can be reached not only due to a sudden event that causes

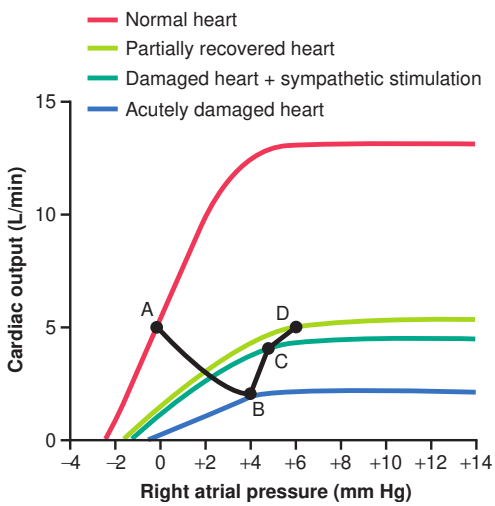

Figure 1.10 – Progressive changes in heart pumping effectiveness after an acute myocardial infarction. Reprinted from [35] with permission, copyright ©2015 Elsevier.

damage to the heart, such as cardiac arrest, but can also be due to the sum of several progressive events that can slowly deteriorate the functioning of the heart. Unhealthy lifestyle or simply reaching an advanced age can generate small decreases in cardiac output, causing slight but frequent physiological responses of the body related to the activation of the sympathetic nervous system and fluid retention. As a result, a normal cardiac output at rest is achieved at the cost of an increase in right atrial pressure (point D in Figure 1.10). For this reason, many people can live with compensated HF without even realizing it, experiencing some of its symptoms when they exercise or engage in demanding physical activity [35].

When the damage to the heart is significant enough that compensatory processes are not sufficient to restore a balanced cardiac output state, it is called decompensated HF. Decompensated HF is characterized by an excessively weak functioning of the heart, which in most cases causes the kidneys not to excrete enough fluid, generating an imbalance between the amount of fluid entering and leaving the body. This imbalance generates excessive fluid retention which in turn causes the compensatory mechanisms of the heart to remain activated without reaching a point of stability. The result of this loop of events is an overstretched heart that cannot achieve sufficient cardiac output for the kidneys to function properly, so the patient is very likely to die if not intervened in time [35].

Figure 1.11 shows the evolution of cardiac efficiency over time when there has been severe damage that has left the heart in a state of extreme weakness. Point A represents the state of cardiac output just before the compensation processes begin, and point B shows the performance of the heart when compensation by sympathetic stimulation is initiated after a few minutes, achieving an increase in cardiac output before fluid retention begins. The horizontal

straight line in Figure 1.11 represents the approximate critical level for the cardiac output to be sufficient for the kidneys to maintain normal fluid balance in the body. Although it may appear that compensatory mechanisms will allow the patient to improve his condition, the cardiac output is still not sufficient for the kidneys to reach their valance point, continuing with excess fluid retention. Subsequently, right atrial pressure rises because the progressive increase in fluid volume forces increased blood flow from the peripheral veins of the patient into the right atrium. After about a day, the cardiac performance reaches point C, where it can be noted that the right atrial pressure has increased due to fluid retention but has not yet reached a point of stability in terms of cardiac output. A short time later (about one more day) point D is reached, where the right atrial pressure continues to increase but it is clear that fluid retention no longer has a positive effect on cardiac output. This point in the evolution of the patient's condition is crucial to determine the final effect of the decompensation, because it becomes mandatory to perform an intervention by means of medication or adjustment of the treatment that allows reversing this chain of events. Unless adequate treatment of the patient is carried out, after a few more days cardiac performance will reach point E, where cardiac output has already begun to decrease and the concentration of edema continues to increase in the tissues, until finally reaching point F where cardiac output is simply unsustainable for the survival of the patient [35].

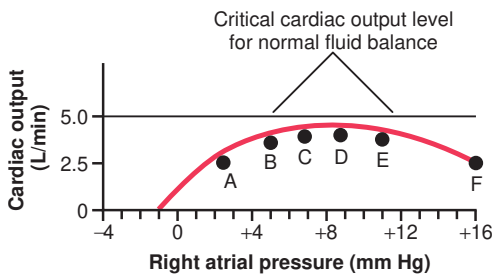

Figure 1.11 – Significant decrease in cardiac output indicating decompensated HF. Reprinted from [35] with permission, copyright ©2015 Elsevier.

One of the main challenges regarding the management of patients with HF is the early detection of decompensation events, considering that decompensated HF often results in the need for hospitalization with excessively high morbidity and mortality. Nearly half of patients must be readmitted for treatment within 6 months of the acute decompensation event, while short-term cardiovascular mortality is 5% (in-hospital) and long-term is 20% (1 year). Additionally, long-term combined outcomes remain deficient, with a joint incidence of hospitalizations, cardiovascular deaths, myocardial infarction, stroke, and sudden death reaching 50% at 12 months after the initial hospitalization [43]. Adequate and early treatment of a patient diagnosed with decompensated HF is extremely important, as decompensation is usually related to non-compliance with therapy or non-optimized therapy.

1.2.6 Management and treatment

It is clear that HF is a rather extensive syndrome characterized by a wide presentation of phenotypes ranging from chronic HF with preserved or reduced EF to acute decompensated and advanced HF. Early management has been prioritized as a research topic throughout the world, bringing an evolution in the management of HF ranging from symptom control to disease-modifying therapy. Early asymptomatic left-sided HF is susceptible to preventive care and its natural progression is modifiable by neurohormonal drug treatments. Therapeutic goals in HF with preserved EF evolve around efforts to improve exercise tolerance by controlling congestion, stabilizing heart rate and blood pressure, since experience has shown that blood pressure reduction relieves symptoms more effectively than targeted therapy with specific agents. In contrast, advanced heart failure, which is typical of HF with reduced EF, causes the patient to remain markedly symptomatic, requiring increasing doses of diuretics (drugs that help eliminate salt and water from the body by making it easier for the kidneys to release more sodium through the increased production of urine [49]) due to persistent renal failure with frequent episodes of decompensated HF that imply the need for recurrent hospitalizations [43].

During a decompensation process such as the one described above in Figure 1.11, the main objective of the treatment is to restore the balance between the amount of fluids entering and leaving the body. Usually, decompensation can be stopped by using diuretics that increase renal excretion and concurrently reducing water and salt intake to reach a fluid balance despite the low cardiac output [35]. Another method used to stop and reverse the decompensation process is by strengthening the heart, especially by administering cardiotonic agents such as Digitalis to reinforce the contraction of the heart, which is known as a positive inotropic action, so that the contractile force of the myocardium increases to pump more blood and consequently increase cardiac output [50].

Although symptom management and strategies to improve the prognosis of HF have largely relied on pharmacological treatments, some patients with HF may also show signs of electrical dyssynchrony, which are associated with increased hemodynamic compromise. Cardiac resynchronization therapy (CRT) is an accepted treatment for patients with wide QRS complex generated by asynchronous contraction between left ventricular walls (intraventricular) or between ventricular chambers (interventricular). CRT basically consists of placing a pacing lead via the coronary sinus to the lateral wall of the ventricle for the purpose of generating coordinated electrical impulses to normalize synchronized cardiac contraction and achieve higher cardiac output. This method has been revolutionary for patients with advanced HF whose only previous option was cardiac transplantation [51, 43]. Additionally, in terms of HF management using implantable cardiac devices (ICD), the use of implantable cardioverter-defibrillator has been strongly recommended in HF patients with substantially reduced EF, considering that they are at increased risk of sudden cardiac death. Furthermore, if those patients meet the QRS

criteria for CRT, a combined treatment of CRT with implantable cardioverter-defibrillator can also be used [52, 53].

The prognosis, symptoms and quality of life of patients with HF have improved markedly with the latest advances in pharmacological treatments, as demonstrated by the combined treatment with the "fantastic four" [54, 55], which includes an angiotensin receptor/neprilysin inhibitor (ARNI), a beta-blocker, a mineralocorticoid receptor antagonist (MRA), and a sodium–glucose co-transporter 2 (SGLT2) inhibitor, providing benefits of 2.7 additional years (for a 80-year-old person) to 8.3 additional years (for a 55-year-old person) without cardiovascular death or first hospital admission for HF [56]. However, these pharmacological treatments should be accompanied by the advancement of device therapies and interventions for the personalized treatment of patients to gain a better understanding of the causes of hospital admission and readmission in patients living with HF [57, 54]. An example of this concern is the high rate of nonresponders to treatments such as CRT, for which it has been shown that 33% of patients receiving therapy do not have a favorable hemodynamic response [51]. Therefore, it has become evident the need to develop new studies focused on the development of treatments based on obtaining markers that allow to optimize the therapy in a regular and patient-specific manner, thus increasing the efficacy of therapies and improving outcomes.

1.3 Cardiac vibration signals (CVS)

The signals generated from the mechanical motion caused by the functioning of the cardiovascular system, primarily associated with the contraction and relaxation action of the cardiac chambers, the opening and closing of the heart valves, and the flow of blood within the heart and through the multiple blood vessels, are known as CVS [27]. These signals can be measured from different parts of the body with different types of instruments and sensors, changing their definition, shape, composition and general characterization according to the location and configuration of the sensors used to record them.

1.3.1 Clinical relevance of CVS

As discussed in the previous section, patients suffering from chronic pathologies involving the cardiovascular system, such as HF, may benefit from a long-term remote monitoring of the main cardiovascular parameters in order to early diagnose decompensation events or to adapt their therapy in a personalized and continuous fashion [6, 7]. In addition, long-term remote monitoring of the patient could significantly reduce treatment costs by preventing the possible worsening of health status that may lead to hospitalization, which has proven to be the main cause of increased health care costs [4]. It is clear that there is currently a wide variety of well-studied and extensively documented methods and tools that provide detailed information

on the mechanical and electrical conditions of the heart within the clinical setting, such as those introduced in Section 1.1.4. However, these cardiac assessment modalities present some limitations against which CVS may present new opportunities and advantages.

Listening to heart sounds represents the oldest method of assessing the mechanical contraction of the heart, since auscultation was used even before these sounds could be electrically recorded for the first time in 1894 in what could be recognized as the first recorded PCG signal [58]. Although the PCG provides useful information regarding the closure of the heart valves and a skilled physician can use this information to determine the operating conditions of the heart, it is almost impossible to use the PCG to extract accurate information about the opening of the heart valves, thus precluding the use of a large number of hemodynamic parameters that depend on the time intervals associated with the opening and closing of the heart valves. Additionally, PCG is not usually recorded in the clinical setting, as physicians usually directly interpret the content of this type of signal through auscultation [59]. The ECG is the best known and most widely used method of cardiac evaluation and monitoring in the clinical setting since the publication of the first results obtained from the use of an ECG recording device in 1903 [60, 61]. However, this method only records the electrical variations associated with the functioning of the heart, which do not adequately reflect the cardiac mechanical variations, which are fundamental for the hemodynamic analysis of the patient [59]. Lastly, Echo is one of the most advanced and relatively recent methods for cardiac assessment, with its invention in 1954 [62]. It offers the possibility of measuring a wide range of hemodynamic parameters, even as a gold standard reference in this aspect compared to other methods. Nevertheless, the main problem with Echo lies in the difficulties related to the development of devices that can be used by patients for continuous, out-of-hospital, long-term monitoring; besides the fact that this method requires trained and skilled physicians to leverage the advantages it offers [63, 43].

On the other hand, the analysis of CVS, interesting sources of information about the cardiac mechanical activity, has already shown remarkable results in the context of long-term remote cardiac monitoring, mainly because the main components of these signals have been associated with some useful hemodynamic markers [64, 65, 9]. In addition, although CVS can naturally present significant inter-subject variability, depending also on the instrumentation used and the location of the sensors, it has been shown that the variability of the intra-subject measurements is actually low, unless there are changes in the cardiovascular health of the subject [66]. Therefore, in recent decades, the idea of using CVS to monitor the health status of the same patient over time has been reinforced [11]. Furthermore, Micro-Electro-Mechanical Systems (MEMS) sensor technology, commonly used to measure cardiac vibration, has significantly improved during the last two decades in terms of size, cost, and resolution, becoming one of the main reasons for the growing interest on the study of CVS for the analysis and monitoring of different pathologies associated with the cardiovascular system [67].

Strong evidence of the growing clinical interest in the analysis and study of CVS is the recent special research topic titled "Cardiac Vibration Signals: Old Techniques, New Tricks and Applications", which has been published in the journal Frontiers in Physiology and has generated a great impact from the moment of its announcement. Figure 1.12 shows the growing interest in this research topic during the last 12 months (based on the date of writing this thesis document). This research topic was organized with the intention of compiling recent findings in the field of cardiac vibrations and addressing current challenges in bringing these techniques into actual clinical or nonclinical use [67], and our team has been pleased to be able to contribute to this research topic with an article that will be further discussed in Chapter 2 of this document [29].

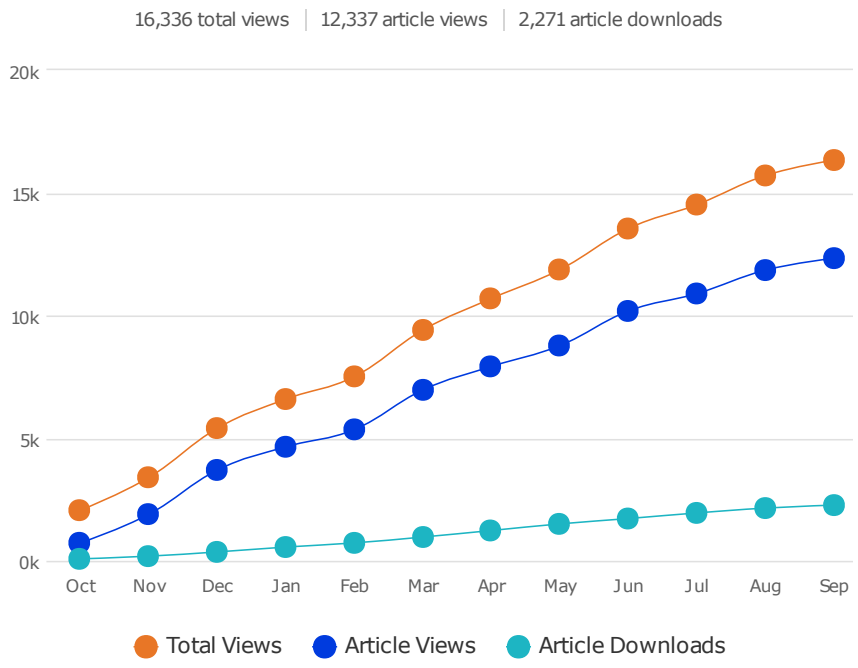

Figure 1.12 – Impact of the research topic "Cardiac Vibration Signals: Old Techniques, New Tricks and Applications" during the last 12 months (October 2021 - September 2022). Reprinted from [68], copyright ©2022 Frontiers Media S.A.

This research topic consists of a collection of seven articles with the participation of more than 40 authors who are specialists in the field. It is primarily focused on the following research areas:

— Clinical applications of CVS in heart failure, coronary artery disease, myocardial ischemia, cardiac valvular dysfunction, hemorrhage, etc [29, 69, 70].

— Non-clinical application of CVS in health and exercise assessment [71].

— Proposition of novel signal processing algorithms and advanced feature-dependent machine learning models and deep learning methodologies to identify cardiac abnormalities from

these signals [72].

— Development of mobile and portable technologies for recording these signals and also new instrumentation for recording the signals [29, 71].

— Modeling of the signals and investigation of the genesis of the waves in these vibration signals and their correspondence with hemodynamic parameters [73, 74].

1.3.2 Noninvasive measurement of CVS

Minimizing invasiveness is one of the main challenges related to the development of medical systems and devices for monitoring physiological variables, and naturally it is a research topic that has been extensively addressed by the CVS field. Mechanocardiogram (MCG) is the definition given to the whole set of CVS that can be measured and recorded in a noninvasive manner regardless of the sensor type and location [28]. The three types of signals that constitute the MCG are described below.

Ballistocardiogram (BCG)

BCG is the oldest of the three components of the MCG, as it was discovered in 1877 and the term was officially established in 1938 [75, 76]. The BCG registers the repetitive movements that the beating of the heart induces in the human body via the flow and acceleration of the blood through all the blood vessels. The movement of the mass of circulating blood and beating heart is measured by the BCG to obtain information associated with the overall functioning of the cardiovascular system [77]. The nature of the BCG addresses the detection of vibrations in a three-dimensional space, where lateral plane relates to right-to-left measurements, transverse plane to dorsoventral measurements and the longitudinal plane to head-to-foot measurements, with this third plane representing the largest projection of the ejection forces of the heart. The main methods currently used to record BCG are the use of sensors placed in the seat of a chair or in a scale, positioning the subject in such a way that the torso remains in an upright position [11].

Figure 1.13 shows a typical BCG signal taken in the longitudinal plane during a cardiac cycle in a healthy subject, with a normal ECG signal as reference. The main peaks and valleys of this signal are denoted by the letters H through L in a standard way, with the highest amplitude peak always denoted by the letter J. Although a verifiable relationship between each of these waves and specific cardiac events has not been defined, it is believed that this waveform generally represents the vasculature of the whole body in response to the ejection of blood by the heart in order to maintain overall momentum [78]. In this regard, one of the main subjects of discussion related to the study of BCG is the development of computational models to determine and simulate the characteristics of the cardiovascular system that give rise to BCG signals. In the

research topic "Cardiac Vibration Signals: Old Techniques, New Tricks and Applications" for instance, two papers have addressed this problem using advanced modeling techniques: in [73] a computational BCG model was presented that includes a closed-loop multiscale representation with 0D elements including cardiac chambers, cardiac valves, arterioles, capillaries, venules and veins, and 1D elements including 55 systemic and 57 pulmonary arteries to consider the contributions of the cardiac chambers and pulmonary circulation. While in [74], a mathematical model based on physiology and the use of evolutionary algorithms is presented to estimate cardiovascular parameters in a personalized manner, combining ECG and BCG signals to capture amplitudes and times of BCG peaks and valleys to estimate arterial pressure and parameters related to ventricular function.

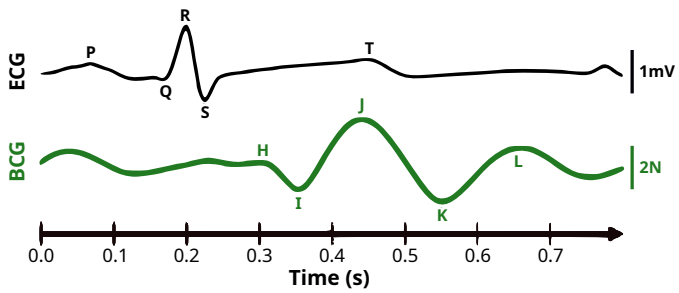

Figure 1.13 – Typical BCG signal during a cardiac cycle in a healthy subject. Adapted from [11], copyright ©2015 IEEE.

Considering that the study of BCG has a long history, and this added to the recent increase in the interest to leverage advances related to the use of MEM systems for the monitoring of CVS, a large number of studies have been developed applying different types of sensors, systems and processing methods related to the use of BCG. A detailed review of the sensors used to obtain BCG signals is presented in [79], in addition to the most relevant signal processing methods applied to analyze the BCG signal and extract physiological parameters such as heart rate, respiratory rate, as well as determine sleep stages. Another aspect of great relevance is the study of the correlation between the content of BCG signals with different hemodynamic parameters, including results that correlate BCG with myocardial contractility [80], cardiac output [81], pre-ejection period [82, 83, 84], diastolic filling time [66] and blood pressure variability via pulse transit time [85] and R-J interval (with the combined use of ECG and BCG signals) [86, 87]. For a more in-depth discussion of the clinical and non-clinical applications of BCG, a detailed review of the main advances, advantages and challenges associated with BCG is presented in [11].

Seismocardiogram (SCG)

CVS can be acquired non-invasively from the chest, in a similar fashion as cardiologists apply the stethoscope for listening to the PCG [10]. The acquisition of accelerometry signals

from the chest of the patient using in particular MEMS devices, leads to the observation of the SCG signal, that is characterized by the presence of two main components, S1 and S2, which correspond to the first and second heart sounds in the PCG, respectively [27]. Although the term SCG was officially established in 1961 [88], the phenomena that give rise to the SCG signal were first studied in 1957, by considering recordings from healthy patients and patients with a history of cardiac disease to make a comparison in the waveform of the two signal types [89].

SCG represents the local measurement of thoracic vibrations generated by the contractile function of the heart to eject blood through the systemic and pulmonary circulation. These vibrations are transmitted from the valves and chambers of the heart to the outside of the chest with components in all three displacement axes that can be captured with a 3D accelerometer [11]. Figure 1.14 shows a typical SCG signal captured with a multi-axial accelerometer in a healthy subject, taking the normal ECG signal as a reference. The X, Y, and Z axes of the SCG in this figure indicate the right-to-left lateral axis, the head-to-foot axis, and the dorso-ventral axis, respectively. The greater amplitude in the SCG signal is normally reflected in the dorso-ventral axis (Z axis), which has generated that most of the published works that study this type of signals concentrate only on the variations represented in this axis [11].

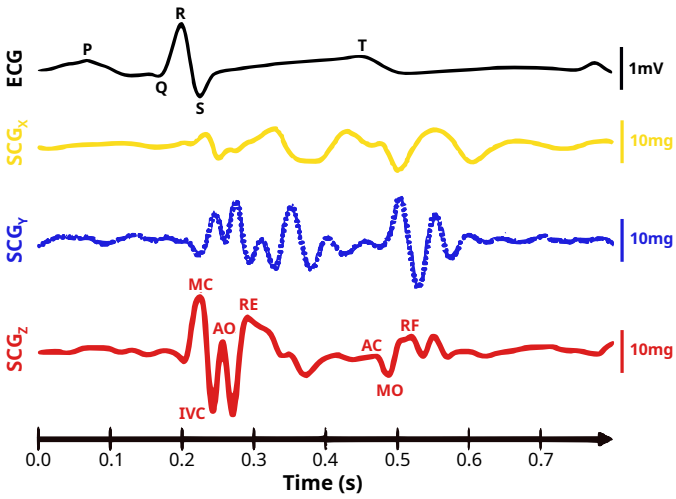

Figure 1.14 – Typical SCG signal captured with a 3D accelerometer during a cardiac cycle in a healthy subject. Adapted from [11], copyright ©2015 IEEE.

One of the main discussions regarding the study of CVS has focused on the definition of points of interest for the accurate detection of cardiac events, especially related to the opening and closing of the heart valves. Figure 1.14 also shows the labels on the SCG Z-axis commonly associated with mitral valve closure (MC), isovolumic contraction (IVC), aortic valve opening (AO), rapid ejection (RE), aortic valve closure (AC), mitral valve opening (MO), and rapid filling (RF). Nevertheless, these labels are based on the intuitive coincidence of these cardiac

events with the peaks and valleys of the SCG signal and do not have a quantifiable statistical validity that would allow their standardized acceptance. The only work that has addressed this issue directly from a deep statistical analysis for the definition of fiducial points in the SCG was recently presented in [90], and has been well received by the scientific community considering the strictness of the experiments performed to support the obtained results. However, the extraction of time intervals based on SCG fiducial points in patients diagnosed with cardiac disease can be difficult, because cardiac patients may have a SCG waveform that is not suitable for fiducial point estimation. Therefore, a preliminary verification by simultaneous measurement of SCG and Echo has recently been suggested before starting SCG-based monitoring of cardiac patients to verify the applicability of the methodology to a specific patient [70].

The main components of the SCG have also been related in multiple studies to different hemodynamic parameters such as myocardial contractility [9, 91, 92], cardiac output [93, 94], stroke volume [95, 92, 96], pre-ejection period and LV ejection time [95, 97, 98, 99, 100, 101]. Therefore, SCG signals acquisition and processing have been widely developed with applications ranging from ischemic heart disease (IHD) characterization, to cardiac stress and HF monitoring [59], even inspiring the development of new techniques such as Forcecardiography (FCG), which is based on the use of force-sensitive resistors and piezoelectric sensors, with the novelty of being able to acquire a new low frequency component (known as LF-FCG) that cannot be appreciated in the common SCG and seems to carry information on the dynamics of ventricular filling and emptying [102, 71]. Furthermore, recent developments of wearable or connected devices offer the possibility to monitor the SCG-based CVS in ambulatory monitoring [12, 13], paving the way toward the development of commercially available portable systems capable of longitudinally monitoring CVS to detect early pathological signatures and assess the appropriate care required by the patient. The most recent and relevant studies describing in detail the main advances, advantages and challenges associated with the processing and use of SCG are [103, 11, 27].

Gyrocardiogram (GCG)

The latest and newest component of the MCG is the GCG, which has emerged as a result of the growing interest in the use of MEMS in the analysis of CVS over the past few decades. GCG was first studied in a 2015 patent and the term was established in 2016 [104, 105]. Similar to SCG, GCG is measured by placing the sensor on the thorax of the patient, but in this case a gyroscope is used to measure the angular velocity (rotation) of the cardiac vibrations transmitted from the heart to the outside of the chest.

GCG is also typically measured by accounting for angular velocity variations in the three-dimensional space, where the axes of rotation are coincident with the axes of the SCG, i.e., the X-axis represents rotation around the right-to-left lateral axis, Y-axis rotation on the head-to-foot axis and Z-axis rotation around the dorso-ventral axis. In this case, it is the Z-axis

that presents the lowest amplitude of detection of CVS compared to the other two axes. The morphology of the GCG is closely related to that of the SCG because both signals are generated from the same principles of cardiovascular functioning. However, GCG signals have been shown to be more robust to inter and intra-subject variations [105], mainly because the rotational signals keep about 60% of the total energy associated with the local cardiac vibrations of the heart [106].

Figure 1.15 shows the two highest amplitude axes of a typical GCG signal taken in a healthy subject, with a normal ECG as a reference of the cardiac cycle. The labels shown in this figure have been designated based on BCG and SCG labels. The main valleys and peaks of the GCG are named with the letters I to L by considering the shape of the signals in both axes simultaneously and based on the BCG labels. Likewise, the cardiac events (MC, AO, AC and MO) are assigned intuitively according to the sequence of events of the cardiac cycle and based on the events defined in the SCG that have been most extensively studied. Although these labels carry a logical justification for their assignment, they have not been quantitatively validated to the level of being defined and accepted by the scientific community as fiducial points [107, 108].

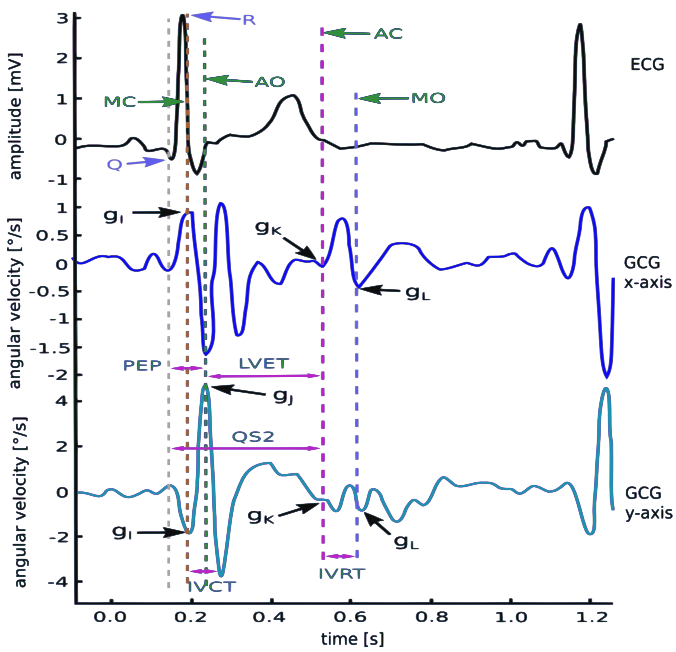

Figure 1.15 – Typical GCG signal captured with a 3D gyroscope during a cardiac cycle in a healthy subject. Note the next acronyms only defined for this figure: isovolumic contraction time (IVCT), isovolumic relaxation time (IVRT), systolic time interval (STI), total electromechanical systole (QS2), left ventricular ejection time (LVET), and pre-ejection period (PEP). Adapted from [107] under a Creative Commons Attribution 4.0 International License .

Although GCG represents an emerging field of research in terms of global spread of knowledge, a large number of works have already been developed to explore different applications of

this type of technology in relation to its close connection with the characterization of hemodynamic parameters, such as myocardial contractility estimation through STE curves [105, 107], LV ejection time and pre-ejection period [109, 110, 12]. Some of the most outstanding applications involve the combined use of GCG and SCG, applying machine learning techniques to detect conditions such as coronary artery disease [111, 72], atrial fibrillation [111, 112], acute decompensated HF [112], myocardial infarction [113], aortic stenosis [114], among others. This growing interest in the development of applications that exploit CVS through the use of computational tools has promoted the creation of public databases, such as the one recently published by Yang et al. in the research topic "Cardiac Vibration Signals: Old Techniques, New Tricks and Applications", presenting an open-access database that includes ECG, SCG and GCG records of 100 patients with different valvular heart diseases, such as aortic and mitral stenosis [69]. For a more in-depth discussion of GCG, a detailed review of the most outstanding advances, advantages and challenges associated with the study and use of GCG can be found in [108, 28].

1.3.3 Invasive measurement of CVS

Although external methods of CVS measurement have proven to be quite useful, they struggle to obtain high-quality, chronic, longitudinal cardiac vibration data because of the difficulties they can present in ensuring both patient comfort and reliability of signals acquired on a long-term continuous basis, as they involve devices that a clinician or the patient must frequently remove and reinstall in the context of daily life. Implantable systems may be a solution to this observability challenge. Bearing this in mind, several studies have examined how accelerometric signals can be acquired to measure cardiac vibration from within the heart chambers in an invasive manner [64, 8, 115, 16, 14, 116, 15]. These endocardial acceleration (EA) signals have two main components known as EA1 and EA2, which are associated with the first and second heart sounds, respectively. These studies are mainly focused on the analysis of the peak endocardial acceleration (PEA) measured on the two main components of the signal, designated PEA1 and PEA2. The main objective of this CVS measurement technique is to develop strategies for the monitoring of hemodynamic parameters that may be useful in the optimization of implantable cardiac devices (ICD) with transvenous pacing leads installed inside the heart, such as pacemakers and CRT devices.

Other studies have focused on the measurement of CVS by using accelerometers attached to the epicardium (outer wall of the heart) [65, 117, 118, 22, 119, 120, 121], usually over the ventricular zone. One of the main drawbacks related to this type of measurement technique is the fact that the sensors must be installed during a highly invasive procedure, usually through open chest surgery such as sternotomy. Therefore, this condition represents a major limitation for the implementation of this technique, generating that the studies performed so far are only intraoperative in humans, during the realization of surgeries requiring sternotomy, and postop-

erative only in animal experimentation. Some studies have also been interested in the direct comparison between EA and epicardial acceleration signals [122, 123], finding that these signals are highly correlated despite differences in shape and spectral content.

Considering the risks associated with the highly invasive procedures that must be performed to capture acceleration signals in direct contact with the heart, such as sternotomy for epicardial acceleration and the risk of infection or complications in the installation and replacement of transvenous catheters for EA signals [20, 21], new types of implants have begun to be explored with the purpose of requiring the use of minimally invasive procedures. The subcutaneous space has been considered as a suitable site for the measurement of CVS [40, 124, 125, 126], since it can preserve the advantages offered by an implantable system in terms of long-term monitoring of hemodynamic parameters, without the risk associated to the application of high-risk surgical interventions.

Correlation with hemodynamic parameters

Acceleration measurements containing the different types of CVS can be mathematically manipulated by integrating the values in the recordings to obtain indirect measurements of cardiac muscle velocity and displacement [127]. These measurements should be able to reflect the hemodynamic performance of the heart by intuiting that damage caused by heart disease should affect and modify the mechanical behavior of the entire cardiovascular system. For this reason, as was also evident in the study of noninvasively acquired CVS, one of the main objectives in the study of cardiac vibrations has been to demonstrate and validate the fact that the components of these signals have a high correlation with different types of hemodynamic parameters.

Table 1.2 shows a compilation of the main papers that have found in their results a high correlation between EA signals and different hemodynamic parameters, while Table 1.3 shows the main papers that have studied this same type of correlation using epicardial acceleration signals instead. These tables include a brief summary of the experimental context of each work and the type of instrumentation used to measure the analyzed signals, which reflects the scope and validity of the results obtained in each of these works and allows to make a direct and easy comparison between all of them. All the results obtained in the works shown in both tables demonstrate a high correlation rate between CVS and different hemodynamic parameters, which include amplitude, time and frequency analysis of the main components of the accelerometric cardiac vibrations and their mathematical variations, in relation to hemodynamic parameters associated with intracardiac and major vessel pressure, and other markers such as the A wave measured from the echocardiogram and associated with atrial contraction [128], and the cardiac index calculated from cardiac output and body surface area.

Ref.	Compared cardiac variables		Correlation	Experimental context	Instrumentation
	Vibrational	Hemodynamics			
[64]	PEA1	Positive peak of RV dP/dt	r=0.97, P<0.001	3 patients with normal ventricular function during dobutamine and pacing interventions.	Accelerometer inside the tip of a pacing lead inserted in the RV. Catheter tip micromanometer inserted into the RV apex.
[8]	PEA1	Positive peak of LV dP/dt	r=0.83, P<0.001	9 anesthetized sheep at baseline and during hemodynamic interventions by nitrate, metaraminol and dobutamine infusions.	Accelerometer in the tip of pacing lead fixed to the apex of the RV. Aortic and LV Millar catheters.
	PEA2	Aortic diastolic pressure	r=0.91, P<0.001		
		Negative peak of LV dP/dt	r=0.92, P<0.001		
[115]	PEA1	First heart sound amplitude (VDD mode)	r=0.81, P<0.001	10 patients underwent dual chamber pacemaker implantation during A-V delay scan in VDD and DDD modes.	Ventricular lead containing accelerometer at its tip. PCG system placed on the mitral area.
		First heart sound amplitude (DDD mode)	r=0.89, P<0.001		
[16]	PEA1	Positive peak of LV dP/dt	r=0.91, P<0.001	9 healthy, anesthetized pigs. Myocardial contractility increased by infusion of dobutamine and depressed by infusion of esmolol.	PEA sensor-embedded pacing lead in the RA (SonRtip^{TM}), and RV pacing lead at the apex. Millar catheter tip micromanometer into the LV cavity.
[116]	EA4 timing	A wave timing (atrial contraction)	r=0.76, P=0.019	15 patients indicated for CRT. Tests performed under different A-V delay programming.	Accelerometer in the tip of pacing lead in the RA (SonRtip^{TM}). Echo Doppler acquisition.
[15]	EA1 energy	Positive peak of LV dP/dt	r=0.78, P<0.05	6 anesthetized sheep with myocardial infarction under artificial respiration modified to provoke Valsalva-like maneuvers.	Accelerometer in the tip of pacing lead in the RV (SonRtip^{TM}). Millar multi-sensor lead inserted into the LV.
[123]*	PEA	Echo acceleration	r=0.89, P<0.01	1 anesthetized sheep underwent sternotomy connected to a volume-controlled respirator.	Accelerometers inserted through the RV wall and sutured to the RV surface. Echocardiographic records processed by speckle tracking algorithms.
	Peak epicardial acceleration		r=0.97, P<0.001		

Table 1.2 – Correlation between EA signals and hemodynamic parameters. *Note that the last reference also includes an epicardial acceleration signal approach.

Ref.	Compared cardiac variables		Correlation	Experimental context	Instrumentation
	Vibrational	Hemodynamics			
[65]	Circumferential peak systolic velocity	Circumferential systolic strain (Echo)	r=-0.76, P<0.001	10 patients with significant left anterior descending coronary artery stenosis underwent off-pump coronary artery bypass grafting.	3D accelerometer sutured onto the left anterior descending coronary artery–perfused region of LV. Echocardiography scanner with transesophageal transducer.
[117]	Circumferential peak systolic velocity	Cardiac output	r=0.81, P<0.001	14 anesthetized pigs underwent sternotomy. LV function modified by infusing esmolol, nitroprusside, epinephrine, and colloid fluid.	3D accelerometers sutured to the LV outer wall. Ultrasonic 16 mm flow-probe placed on the aorta. Millar micromanometer catheter in the LV apical region.
		Positive peak of LV dP/dt	r=0.73, P<0.001		
[118]	Epicardial 3D peak systolic velocity in the apical region of the LV	Positive peak of LV dP/dt	r=0.77, P<0.001	13 anesthetized closed-chest pigs. Experiments were performed 30 minutes after surgery (sternotomy), by exerting changes in global LV function (unloading, fluid loading, esmolol, dobutamine).	3D accelerometers sutured to the epicardium in the LV apical and basal regions and to the RV basal region. A fourth 3D accelerometer placed subepicardially in the LV apical region. One PiCCO catheter into the left femoral artery and two Millar micromanometer into the LV and RV.
		Cardiac index	r=0.74, P<0.001		
	Epicardial 3D peak systolic velocity in the basal region of the LV	Positive peak of LV dP/dt	r=0.63, P<0.001		
		Cardiac index	r=0.69, P<0.001		
	Epicardial 3D peak systolic velocity of the RV	Positive peak of RV dP/dt	r=0.72, P<0.001		
		Cardiac index	r=0.73, P<0.001		
	Subepicardial 3D peak systolic velocity of the LV	Positive peak of LV dP/dt	r=0.86, P<0.001		
		Cardiac index	r=0.82, P<0.001		
[22]	3D peak energy of the LV acceleration	Positive peak of LV dP/dt	r^2=0.94	2 healthy, anesthetized pigs with inotropism variations induced by the infusion of dobutamine.	3D accelerometer ligated on the epicardium of the LV free wall. Millar micromanometer catheter in the LV.
[120]	Frequency of myocardial acceleration	End-diastolic volume	r^2=0.81	9 anesthetized pigs at baseline and fluid loading, and phlebotomy in a closed chest condition.	3D accelerometer placed on the anterior LV apical region. Sonomicrometry crystals subendocardially in long axis pair and short axis pair.

Table 1.3 – Correlation between epicardial acceleration signals and hemodynamic parameters.

Applications in implantable cardiac devices (ICD)

ICD such as CRT defibrillators, cardioverter-defibrillators and pacemakers are normally used in the treatment and follow-up of chronic heart diseases as HF. Some of these ICD already integrate accelerometer sensors to observe and analyze cardiac accelerometry signals from subcutaneous or intra-cardiac sites [129], with the objective to predict future HF events [17, 18], for instance, the increasing study of CVS for the development of ICD in the field of HF has led to the proposal of candidate markers of the progression of this disease, such as the presence of an S3 component [40, 41]. CRT is one of the treatments on which most of the applied research of invasively acquired CVS has been carried out. CRT is a treatment widely studied and accepted by the medical community for its implementation in patients with symptomatic heart failure with reduced left ventricular EF and abnormal QRS complex morphology. In CRT, intracardiac leads are typically implanted in both ventricles to electrically stimulate the RA, RV and LV at controlled times, with the purpose of improving ventricular filling and contraction by re-synchronizing the biventricular mechanical function [130].

Although CRT has been shown to be effective for the treatment of HF, not all patients may benefit from an active cardiac implantable device [25, 26]. For this reason, several studies have been developed with the purpose of defining automatic optimization protocols of the ICD parameters that allow treatment to be tailored to the needs and conditions of each patient [19, 131, 132]. One of the main results of the progress of this research is the invention of the SonRtip^{TM} lead, which is so far the only commercially available atrial pacing lead that includes an integrated microaccelerometer [133]. Many of the works up to this point mentioned in this document have implemented this lead and its previous versions for the analysis of correlation between CVS and hemodynamic parameters and the development of optimization algorithms for ICD configuration, which has allowed the continuous improvement of this device. Figure 1.16 shows a schematic representation of the SonRtip^{TM} probe.

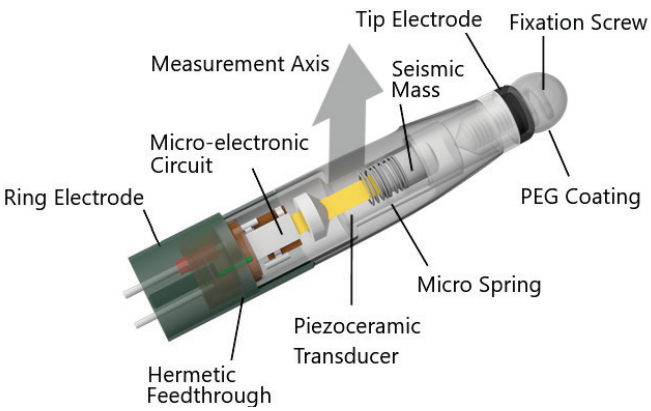

Figure 1.16 – SonRtip^{TM} atrial pacing lead for CRT. Reprinted from [126].

1.4 Conclusion

HF is a multifactorial syndrome that alters the structure and function of the heart, reducing its capacity to pump the blood needed to meet the requirements of the organism and consequently compromising the overall functioning of the cardiovascular system. Despite major advances in the pharmacological treatment of this syndrome, it is necessary to complement such advances with new studies focused on the development of device therapies based on obtaining markers that allow to optimize treatments regularly and in a patient-specific manner, aiming to increase the efficacy of therapies and reduce the hospital admissions and readmission of patients living with HF.

The analysis of CVS, interesting sources of information about the cardiac mechanical activity, has already shown remarkable results in the estimation of useful hemodynamic markers. These signals can be acquired externally, giving rise to the MCG, or invasively using techniques that can be exploited in the development of ICD for chronic CVS acquisition without requiring continuous intervention of the patient. However, the use of highly invasive methods can lead to other types of consequences and risks for the patient. In addition to the challenge posed by the high noise content in CVS associated with the nature of the measured physical phenomena, which can be generated by mechanical disturbances associated with the different activities that the patient may perform when the signals are measured. Therefore, in the field of chronic cardiovascular diseases, it is necessary to develop remote CVS monitoring systems based on minimally invasive devices that offer integrated management of multimodal parameters with sufficient robustness against the different measurement conditions.

Chapter 2

Acquisition of cardiac vibration signals using a novel gastric implant

The analysis of cardiac vibration signals (CVS) has proven to be an interesting tool for monitoring chronic pathologies involving the cardiovascular system, such as heart failure (HF). However, methods remain to be developed to obtain high quality longitudinal and real-world data, which do not require patient involvement to correctly and regularly acquire these signals. Implantable systems may be a solution to this observability challenge. This chapter discusses the hypothesis that CVS can be captured from a small monitoring implant positioned at the gastric fundus, which could be delivered via gastroscopy in a minimally invasive manner. This anatomical site seems a good candidate site for long-term cardiovascular monitoring, as it is physically close to the heart (see Figure 2.1). This chapter describes the characterization of the acquired signals in pre-clinical experimentation and evaluates the feasibility to obtain useful hemodynamic markers from these intra-gastric signals.

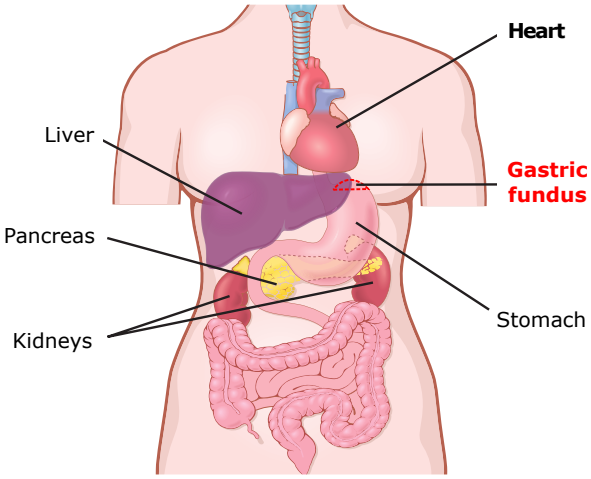

Figure 2.1 – Anatomical localization of the gastric fundus and the main surrounding organs. The gastric fundus corresponds to the area of the stomach enclosed by the red dashed line. Adapted from [35] with permission, copyright ©2015 Elsevier.

The content of this chapter is strongly based on our article that was published within the special research topic "Cardiac Vibration Signals: Old Techniques, New Tricks and Applications" in the journal Frontiers in Physiology [29]. This work was developed within the framework of the project entitled "Digital Implantable Gastric Stethoscope (DIGS)" of the Agence Nationale de la Recherche (ANR) [34], whose main objective is to validate a data extraction process for early detection of HF decompensation in real-life conditions. The DIGS project is developed in direct collaboration between LTSI, the TIMC team, the company SentinHealth and the LRB. This multidisciplinary consortium brings the necessary expertise from the clinical field to ensure the relevance of selected pre-clinical models and selected pathophysiological parameters (LRB partner), the scientific skills in the field of cardio-respiratory parameters monitoring techniques and associated information processing methods (LTSI and TIMC partners), and the knowledge in the industrial fields of electronics and mechatronics to ensure the valorization of the results (SentinHealth partner).

2.1 Presentation of the gastric implant

Existing implantable cardiac monitoring devices allow the acquisition of relevant physiological parameters that, if properly analyzed, can lead to early detection of decompensation events in HF patients. However, these devices can be highly expensive or may require complex implantation procedures with associated potential risks for the patient [21, 134, 135]. Among this type of devices, the CardioMEMS Heart Sensor stands out, consisting of a compact implantable device installed in a branch of the pulmonary artery, allowing direct measurement of pulmonary arterial pressure for hemodynamic monitoring in chronic HF [136]. Even so, in addition to being a highly invasive device, the CardioMEMS operates under a monoparametric measurement concept, which is a major disadvantage considering that HF is a multiparametric syndrome, and multiparametric approaches have already proven to offer better results in HF monitoring [137, 17]. Other implantable devices consider the measurement of multiple cardiovascular parameters to improve the outcomes of their approaches [138, 139], but such devices become relevant for a small portion of HF patients because they are equipped with cardiac defibrillators such as those used in cardiac resynchronization therapy (CRT) [51].

The company SentinHealth has recently developed an innovative gastric implant prototype to acquire electrophysiological and mechanical cardiac data from the gastric fundus [140], with the aim of recording various cardiovascular parameters to address the multiparametric concerns in the monitoring of HF. Most of the gastric implants commercially available are prescribed to treat gastric dysmotility syndromes and obesity. Several papers have demonstrated the safety and tolerability of these devices, as well as recent developments in minimally invasive techniques to place these implants, improving patient comfort and adherence [141, 142]. The implant developed

by the company SentinHealth can be as well tolerated as other gastric implants and could be administered using similar minimally invasive implantation techniques such as gastroscopy [143]. Three prototype versions of the device have been used in this work: one semi-implantable version (V0) and two fully implantable versions (V1 and V2).

2.1.1 Prototype V0

This is the first prototype of the gastric implant and is the only semi-implantable version of the device. Figure 2.2a shows the schematic design of this version of the implant. It is composed of two modules: 1) a 30 mm long, 9 mm wide, 7 mm high gastric module, with each end corresponding to a titanium electrode of 35 mm^2 surface area and 20 mm electrode spacing, where the electrodes are connected to an ECG chip embedded in the capsule. This module is shown in Figure 2.2b. 2) The second module corresponds to a reference ECG unit composed of two external electrodes attached to the thorax: one on the anterior thorax and one on the posterior thorax. These electrodes are connected to an external electronic board encapsulated in a pig jacket as shown in Figure 2.2c. Both ECG signals are acquired synchronously with a sampling rate of 1 kHz. Both modules are linked through a wired connection that passes across the skin barrier. The acquired data is stored in the external module and then transmitted to a computer via Bluetooth for further processing. This prototype device was used to validate the acquisition of electrophysiological signals from the heart by comparing the acquisitions from both modules.

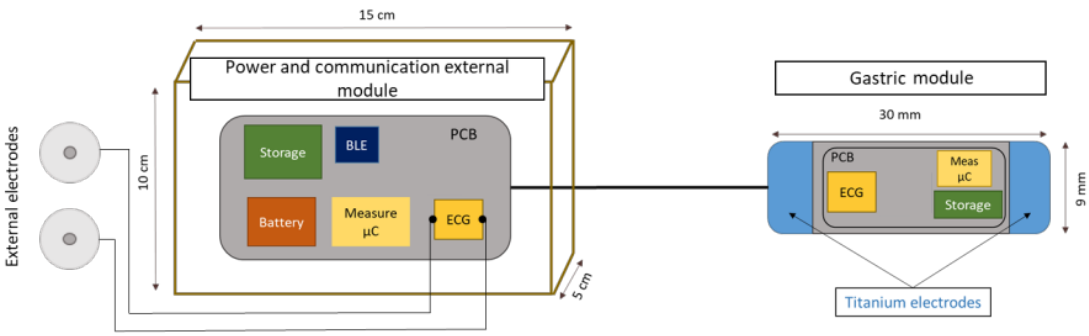

(a) Schematic representation

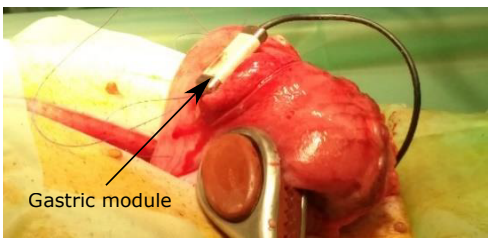

(b) Physical design of the gastric implant

(c) Physical design of the external module

Figure 2.2 – Gastric implant prototype V0.

2.1.2 Prototype V1

This prototype is shown in Figure 2.3 and consists of two implantable modules interconnected by a wire: the first module (located in the gastric fundus) is $35 \times 9 \times 5.5$ mm and incorporates a 3D accelerometer, as well as an ECG acquisition device with two titanium electrodes, with the same geometry as the V0 prototype, located at each end of the capsule and electrically isolated from each other by a body in polyetheretherketone (PEEK). The second module, implanted subcutaneously in the abdomen, measures $70 \times 30.5 \times 16$ mm and is connected to the first module by a 30 cm wire. It incorporates two AA batteries, as well as the Bluetooth low energy chip (2.4 GHz) that allows data to be communicated to an external gateway for further processing. The ECG sampling rate in this version is 1 kHz, while the sampling rate of accelerometry (ACC) data is 4 kHz acquired in the 0 to 1 kHz bandwidth. The weight of the gastric module is 3.3 g.

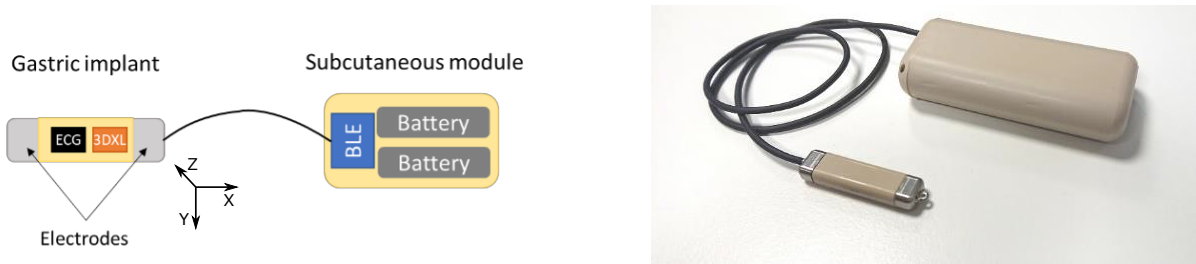

(a) Schematic representation (b) Physical design

Figure 2.3 – Gastric implant prototype V1.

2.1.3 Prototype V2

Figure 2.4 shows the V2 prototype of the implant, which differs from the previous one in two main aspects: first, the geometry, size and material of the gastric capsule were redesigned to approximate the final design idea of the device built in one piece (for future development). One of the electrodes is a part of the housing that is made of titanium. To ensure electrical isolation from the rest of the housing, an epoxy resin coating was applied to the titanium surface. The other electrode is an insulated piece of titanium (see Figure 2.4b). Secondly, the communication components have been transferred inside the gastric module. For this purpose, a specific antenna was designed to optimize the performance of Bluetooth transmission from the stomach. The antenna is located at one end of the gastric capsule and is overmolded in epoxy resin. The geometry and material of the subcutaneous module is unchanged from the V1 prototype. This module incorporates only the AA battery. In terms of technical aspects, the gastric module in this version is $40 \times 13.5 \times 5.5$ mm and its weight is 7 g. The ECG chip was also changed to optimize current consumption with a sampling rate of 498 Hz.

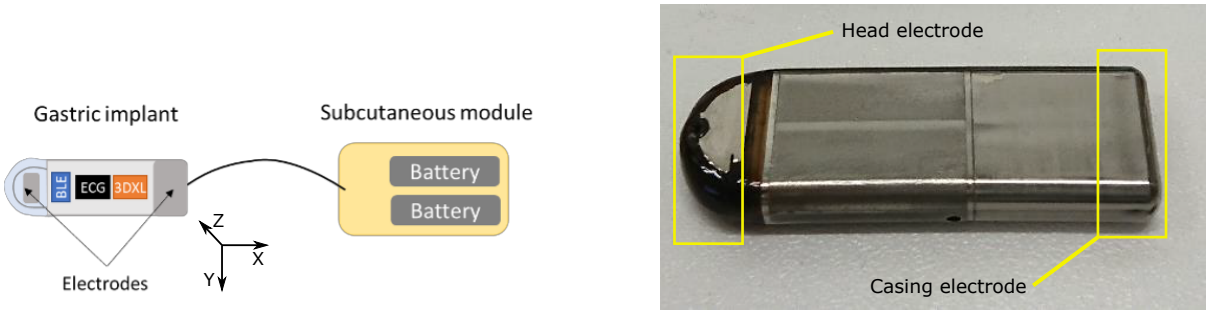

(a) Schematic representation

(b) Physical design

Figure 2.4 – Gastric implant prototype V2.

All versions of the implant used a setting that allows the implant to remain in low battery mode while no signal is being measured to extend battery life. This setting also allows the device to automatically switch to active mode for a duration of 30 seconds to acquire simultaneous ECG and ACC signals. The 30-second acquisition time duration has been selected to optimize the relationship between power consumption and the minimum number of cardiac cycles required to obtain a stable representation of the mean cardiac cycle observed from the intragastric ECG and ACC signals. In addition, the final device is intended to incorporate a classic battery in a first generation, but the final purpose of the last generation of the device aims to incorporate a rechargeable battery to be powered wirelessly, in order to increase device lifetime and patient follow-up time.

2.2 Acquisition of ECG and ACC cardiac signals

The experiments developed in this work consisted of the acquisition of ECG and ACC signals from 9 pigs using the three different versions of the gastric implant described above. The experimental framework for data acquisition was adapted according to the purpose for which the data were acquired. Data acquisition process is divided into two phases: phase 1 focuses on the comparison of signals acquired from the gastric fundus with reference data acquired through standard thoracic site sensors. A set of cardiovascular markers is extracted from the reference and gastric signals to be quantitatively compared. Phase 2 was concerned with assessing the feasibility of estimating longitudinal cardiovascular markers from the gastric site. All animal experiments were previously submitted to an ethics committee in accordance with French regulations and were performed in specialized structures with the approval of the dedicated site, by a team composed of qualified staff who completed regulatory training in animal testing and experimental surgery.

2.2.1 Data acquired for phase 1

ECG and ACC data were acquired simultaneously from standard thoracic locations to validate measurements taken from the gastric site. Measurements taken superficially were used as the gold standard using two experimental setups, one to validate ECG data and one for ACC data:

1. The first setup was focused on the validation of ECG data. A total of 459 recordings each of 30 seconds duration were acquired using the V0 prototype over a 14-day period from one pig. Each recording consisted of synchronous data from a standard bipolar surface ECG (gold standard reference) and the gastric ECG.
2. The second setup was dedicated to the validation of the ACC data. Two recordings were acquired simultaneously from a second pig, with prototype V1 and an external digital stethoscope (3M^{TM} Littmann, USA), used as the gold standard PCG. A Valsalva-like respiratory maneuver was applied during data acquisition to evoke hemodynamic modifications that can be observed from both acquisition sites. Data acquisition was performed acutely, under anesthesia, with ventilator-assisted breathing and consisted of a continuous 30 cmH_2O positive inspiratory pressure (CPP) stage of 15 seconds duration, followed by 10 seconds of apnea at atmospheric pressure [15]. The main objective of this setup was to validate whether the evolution of markers obtained from gastric and reference sites during the valsalva-like maneuver are correlated.

2.2.2 Data acquired for phase 2

In the second phase of data acquisition the prototype V1 and V2 implants were used to acquire the electrophysiological and CVS from the gastric fundus of 4 healthy pigs and 3 pigs with induced chronic ischemic heart failure resulting in acute decompensated heart failure. Each device was implanted for a minimum period of one week, and a maximum of 2 weeks. During this period of time, the animals were kept in individual cages with controlled temperature and normal feeding conditions. Caretakers provided dedicated attention to the pigs on a daily basis to ensure that they were healthy and the device did not cause any problems, such as pain or loss of appetite.

The gateway used for data collection was located above the cages at an approximate distance of 1 meter from the pig. Data were recorded from the implant for 30 seconds every hour, with random acquisition cessation periods related to some technical problems (sometimes the scheduled acquisition was not performed or sometimes the device was unable to communicate with the server). The entire acquired database results in a total of 999 recordings of 30 seconds each, with the distribution shown in Table 2.1.

Pig ID	1	2	3	4	5	6	7
Total recordings	95	163	232	316	70	73	50
Time frame in days	7	14	14	14	13	14	12
Class	healthy	healthy	healthy	healthy	induc. HF	induc. HF	induc. HF
Implant version	V1	V1	V1	V1	V2	V2	V2

Table 2.1 – Description of the data distribution.

2.3 Processing applied to acquired signals

It is to be expected that ECG and ACC data acquired from the gastric fundus may have specific characteristics and noise conditions, particularly related to the location and orientation of the device, as well as interference from electrical and mechanical activities of the gastric system. For this reason, it is necessary to apply a processing chain to reduce the noise present in the signals in order to exploit both electrophysiological and mechanical target content.

Figure 2.5 presents a schematic summarizing the signal processing chain applied to cardiac data: 1) noise removal from ECG and ACC data, 2) noise robust real-time QRS detection from ECG signals and cardiac cycle segmentation, 3) cardiac cycle correlation analysis and calculation of coherent mean from aligned ECG and ACC segmented cycles, 4) segmentation of cardiac vibration components (S1 and S2) from coherent mean ACC data, and 5) estimation of signal context and signal-to-noise ratio (SNR) in both types of signals.

2.3.1 ECG and ACC Data denoising

Baseline removal

ECG and ACC signals are affected by low-frequency noise from two different main sources. The first source of noise comes from the instrumentation. In fact, each transition from low-power consumption mode to active mode generates a low-frequency transient state during the first 5 seconds of data acquisition. In order to exploit as much as possible the signal content, a baseline elimination process is applied to the signals, managing to process 29 seconds of each signal, and having to eliminate only the first second, where the transient state generates a saturation of the amplifiers and completely impedes the acquisition of any useful data. The second source of noise corresponds to the electrophysiological and mechanical components of the electrogastrographic and respiratory activity, which are captured by the electrodes and the accelerometer.

Accordingly, a baseline elimination process is applied to ECG and ACC data and is based on a locally weighted linear regression algorithm [144]. To reduce the computational cost of the

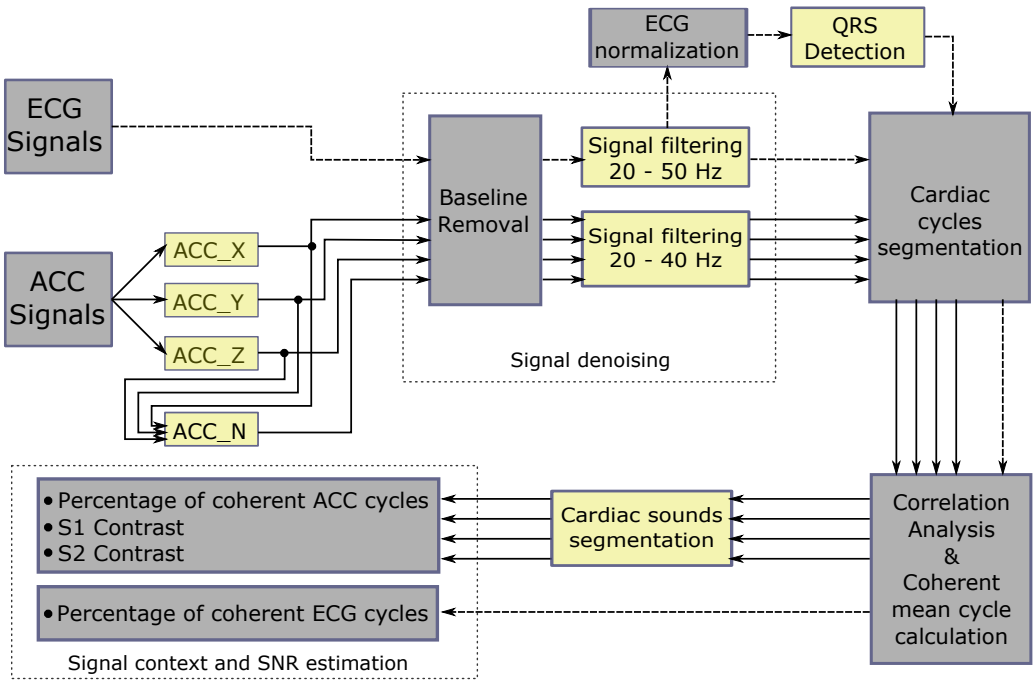

Figure 2.5 – Global diagram of the processing chain applied to the acquired data. Dashed-line arrows represent the ECG signal pipeline and solid-line arrows represent the ACC axes pipeline.

baseline removal process, the linear regression algorithm is applied in 4-second windows and each signal is reduced to 400 Hz in each window. The output of the linear regression algorithm is the representation of the signal baseline, which is directly subtracted from the original signal, thus preserving its main features [144]. The norm of the 3D ACC vector is calculated before applying the baseline removal process and is treated as a new ACC axis from this point, representing an ACC component independent of the direction of acceleration.

Signal filtering

Frequency-based filtering methods are widely documented in the literature for ECG and cardiac vibration signal analysis. The combination of independent high-pass and low-pass fifth-order Butterworth filters is applied to the signals using direct and inverse zero-phase digital IIR filtering, and defining different cutoff frequency values depending on the type of signal. The band selected for ECG signals is from 20 to 50 Hz in order to reduce the T-wave amplitude and emphasize the R peak to facilitate the subsequent QRS detection process. The band for ACC signals is 20 - 40 Hz, considering the frequency bands that contain most of the signal energy in local cardiac accelerometer signals [24, 126]. Figures 2.6a and 2.6b show representative examples of filtered ECG and ACC signals, respectively.

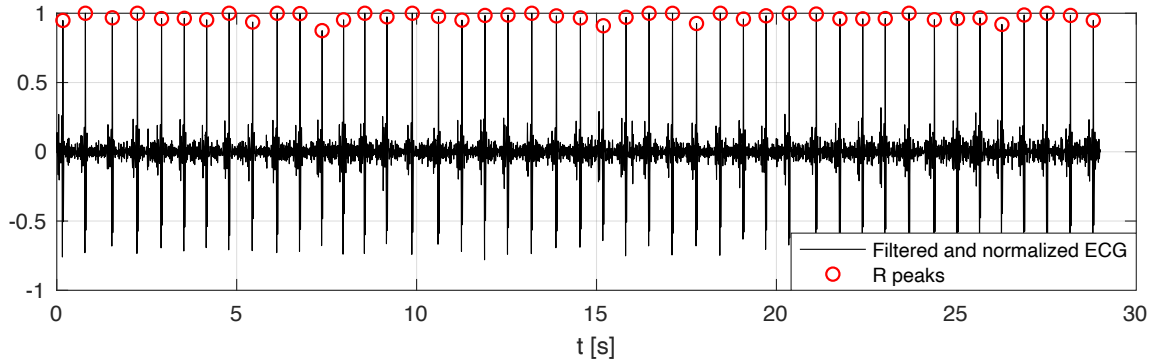

(a) ECG signal after applying baseline removal, filtering, normalization, and QRS detection processes

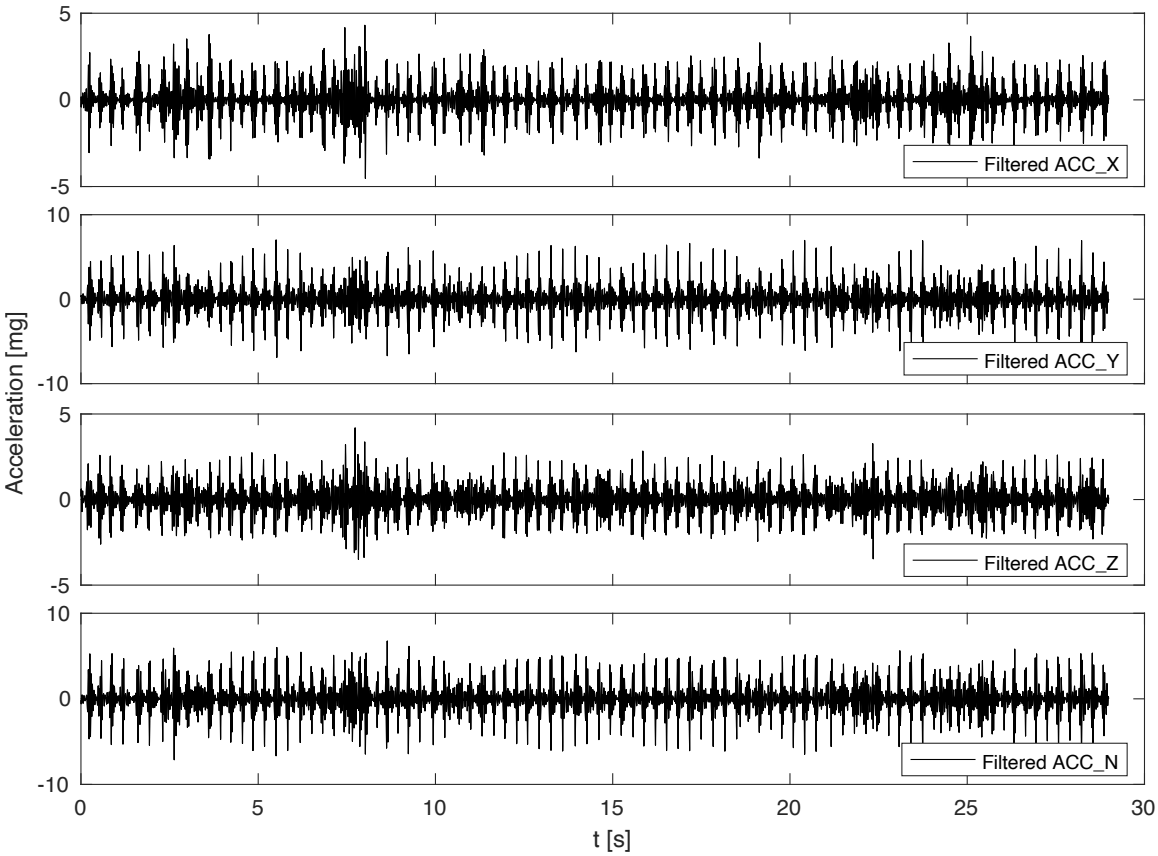

(b) ACC axes after applying the baseline removal and filtering processes, the N-axis represents the norm

Figure 2.6 – Example of the denoising result of ECG and ACC cardiac signals.

2.3.2 QRS detection from ECG signals

Aiming to facilitate the QRS detection process, a locally performed normalization based on the local minima/maxima values was applied to the filtered ECG signal. This normalization algorithm is presented and described in detail in [144]. The only modification applied in this work to the original normalization algorithm is the use of the median value instead of the mean to clip the lowest values of the normalization signal. This change corresponds to the robustness presented by the median value to outliers, improving the stability of the algorithm even in the presence of some particularly noisy signals. After normalizing the ECG signals, a robust real-time QRS detector based on a probabilistic multiple function method was used to identify the locations of the R-peaks of the ECG signal [145]. This detector was used because the target signals were suspected to have many artifacts and needed to be handled with a detector designed for such conditions. Figure 2.6a shows an example of the normalized ECG with its respective R peaks highlighted.

After applying the QRS detection algorithm to the ECG signals, the heart rate (HR) is calculated using the median duration of all cardiac cycles. The cardiac cycles are segmented by taking $0.05 * 60/HR$ seconds before the R peak as the starting point of each cardiac cycle. This is a dynamic delay set to preserve the complete waveform of the QRS complex, regardless of the heart rate variation between signals in the entire data set. The cardiac cycle segmentation process is applied directly to the ECG signal and subsequently projected to all axes of the ACC signal because both signal types were acquired simultaneously.

2.3.3 Correlation analysis of cardiac cycles

Once the cardiac cycle start points are defined, the median cycle length is used to resize all cycles through a zero-padding technique. This is applied to ECG and ACC signals. Subsequently, for ECG signals, the normalized cross-correlation between each pair of cycles is calculated, and the dominant group of cycles with a correlation coefficient greater than 0.6 is used to calculate a coherent mean cardiac cycle. It is possible to directly apply this process because all ECG cycles are aligned by the time of occurrence of each R peak and the result of the maximum correlation value. Figure 2.7 shows an example of the ECG cardiac cycles aligned and the corresponding coherent mean cardiac cycle.

Correlation analysis for ACC signals is somehow more complex because the exact starting point of S1 and S2 varies independently of the time of occurrence of the R-peak, mainly due to beat-to-beat modifications of the inotropic state and preload and afterload conditions. Therefore, it is necessary to apply independent phase correction steps for S1 and S2 to increase the correlation between cycles when calculating the mean coherent cardiac cycle [23, 24]. After applying phase optimization to each ACC cycle, the dominant group of cycles with a correlation coefficient greater than 0.6 is used to calculate the mean coherent cardiac cycle independently

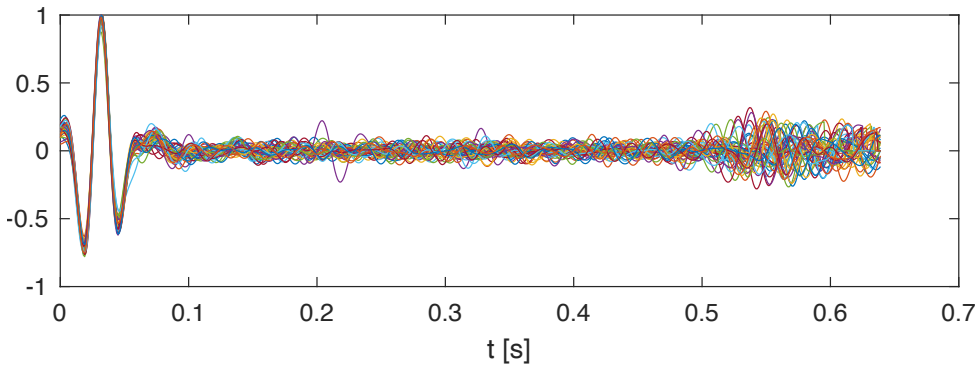

(a) Segmented and aligned ECG cardiac cycles

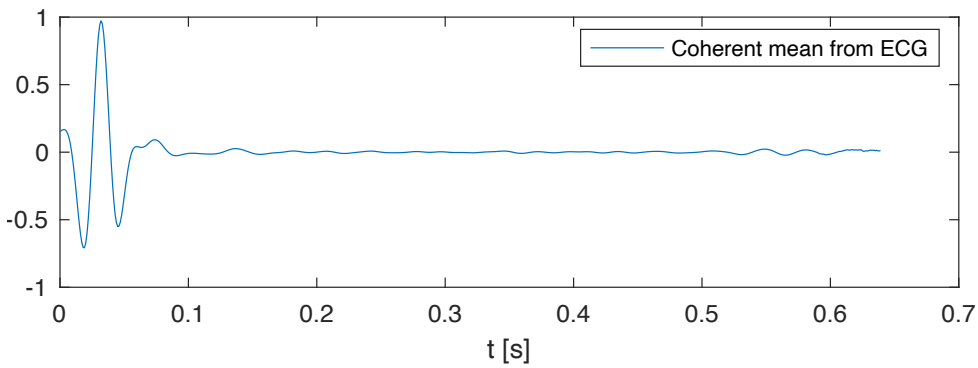

(b) Coherent mean cardiac cycle

Figure 2.7 – Correlation analysis of cardiac cycles.

over each ACC axis. Considering that ACC signals cannot be normalized because it would affect the relationship between cardiac vibration components and hemodynamic markers, outlier cycles are removed according to their energy (an outlier is a value that is more than three scaled median absolute deviations away from the median), in order to eliminate cycles containing distinctive noises, such as pig grunts, gastric sounds, or vibrations that could disturb the coherent mean cycle calculation.

2.3.4 Cardiac sound segmentation (S1 and S2)

An effective algorithm for estimating the S1 and S2 times using the coherent mean of the ACC signals is provided in [24]. First, the coherent mean cycle is normalized and the absolute (Abs) and squared (Sqr) envelopes are calculated. Then, a dynamic threshold between 0.1 and 0.7 is used to identify S1 in the first half of the cycle. S1 is detected by looking for the points where Abs or Sqr cross the threshold (setting the R-peak time as the earliest possible time to define the starting point of S1). Similarly, S2 is identified in the cycle segment between the end of S1 and the end of the cycle. The result of implementing this algorithm is the start and end times of S1 and S2. These values can be defined as follows:

— $t0$ = Reference instant for the start of cardiac cycle (obtained from ECG).

— $t1$ = Start of S1

— $t2$ = End of S1

— $t3$ = Start of S2

— $t4$ = End of S2

— $t5$ = End of cardiac cycle

Hence, S1 corresponds to the signal segment between $t1$ and $t2$, S2 corresponds to the signal segment between $t3$ and $t4$, and finally, the union of the signal segments $t2$-$t3$ and $t4$-$t5$ are considered as the signal background. This process is applied on each ACC axis as well as the norm. An example of the result of this process is shown in Figure 2.8.

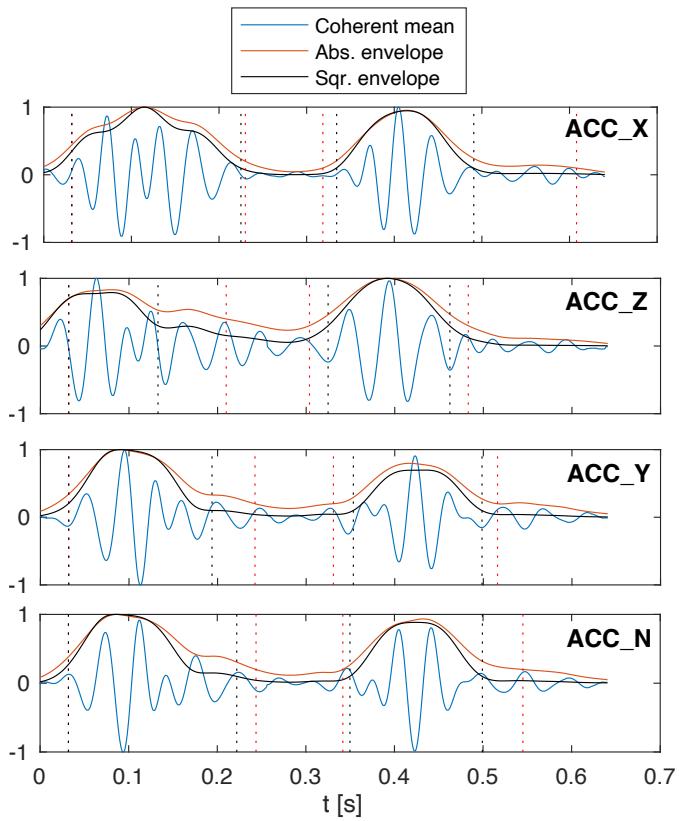

Figure 2.8 – Coherent mean cardiac cycle on each ACC axis with their respective envelopes, including candidate detections for S1 and S2. The vertical dotted lines represent t1, t2, t3, and t4 in red color for Abs and black for Sqr.

2.3.5 Signal context estimation and SNR

In order to quantitatively evaluate the quality of the signals, different features are considered to estimate the SNR. Based on the context variables presented by [24] to configure the control algorithm that automatically recognizes the context of the ACC signals to segment S1 and S2, the following quality measures are proposed in this work:

— The percentage of coherent ECG cycles.

— The percentage of coherent ACC cycles over each axis.

— The S1 contrast, defined as the ratio between the standard deviation of S1 and the standard deviation of the signal background.

— The S2 contrast, defined as the ratio between the standard deviation of S2 and the standard deviation of the signal background.

To estimate the overall quality of the data for each recording, three successive stages of classification were applied, using the quality measures defined above.

1. The first stage is related to the analysis of coherent cardiac cycles in ECG and ACC signals. In fact, in stable cardiovascular conditions and sinus rhythm, the relative number of coherent cardiac cycles can be considered as a marker of signal quality. At this stage, only recordings with three or more coherent cycles in the ECG and at least one from the ACC axis were retained. This relatively low threshold for the number of coherent cardiac cycles was considered appropriate since two other quality assessment phases follow this classification phase.
2. The second stage is based on the detection of S1 and S2 in the ACC signals. In this stage only signals with S1 and S2 contrast greater than 2 were retained. This value was selected because it means that the S1 and S2 content can stand out against the signal background by having twice the standard deviation.
3. The third stage concerns the estimation of the duration and peak-to-peak values of S1 and S2. Since the different envelopes will provide multiple S1 and S2 detection instants for each ACC axis (as shown in Figure 2.8), an algorithm must be applied to merge the local detections from each axis and envelope to obtain the final detection instants for S1 and S2. Algorithm 1 was used to define the final S1 and S2 detection instants by using the contrast measurements described above. Figure 2.9 shows a representative example of the estimated final detection instants for the recording shown in Figure 2.8. After estimating the final values of $t1$, $t2$, $t3$, and $t4$ for each recording, records where the duration or peak-to-peak value of S1 or S2 represent an outlier were removed.

Algorithm 1: Algorithm to define the global detection times of S1 and S2. ACC_{mean} contains the coherent mean with length L for each of the four ACC axes (including the norm). D_{S1} and D_{S2} represent the number of candidate detections for S1 and S2, respectively. Each candidate detection consists of two values corresponding to the start and end of the cardiac event. The *round()* function rounds each element of a vector to the nearest integer, the *min()* function returns the minimum value of a vector, and the *sum()* function computes the sum of the elements in a vector. $\odot$ represents the element-wise product (Hadamard product) between two vectors. The notation $M_{[i]}$ represents the $i-th$ column of the matrix M.

Data: ACC coherent mean $\boldsymbol{ACC_{mean}} : \mathbb{R}^{\boldsymbol{4}} \times \mathbb{R}^{\boldsymbol{L}}$, S1 candidate detections $\boldsymbol{S1_{cd}} : \mathbb{R}^{\boldsymbol{D_{S1}}} \times \mathbb{R}^{\boldsymbol{2}}$, S2 candidate detections $\boldsymbol{S2_{cd}} : \mathbb{R}^{\boldsymbol{D_{S2}}} \times \mathbb{R}^{\boldsymbol{2}}$

Result: S1 global detection $\boldsymbol{S1_{gd}} : \mathbb{R}^{\boldsymbol{2}}$, S2 global detection $\boldsymbol{S2_{gd}} : \mathbb{R}^{\boldsymbol{2}}$

```
→ Identify the best detection candidates
for each candidate detection in S1_cd :
    for each candidate detection in S2_cd :
        for each ACC axis in ACC_mean :
            compute S1 and S2 contrast values;
            if S1 contrast ≥ 2 and S2 contrast ≥ 2 :
                stack S1 candidate in S1';
                stack S1 contrast in W_S1;
                stack S2 candidate in S2';
                stack S2 contrast in W_S2;
→ Transform contrast values into weights
W_S1 = round(W_S1/min(W_S1));
W_S2 = round(W_S2/min(W_S2));
→ Calculate the final detection times
t1 = sum(S1'_[1] ⊙ W_S1) / sum(W_S1);
t2 = sum(S1'_[2] ⊙ W_S1) / sum(W_S1);
t3 = sum(S2'_[1] ⊙ W_S2) / sum(W_S2);
t4 = sum(S2'_[2] ⊙ W_S2) / sum(W_S2);
→ Save the global detection for S1 and S2
S1_gd = {t1, t2};
S2_gd = {t3, t4};
```

Additional SNR estimators were used to validate the quality analysis and to obtain quantitative results that can be compared with the literature. The SNR for a given heartbeat in ECG signals is calculated by considering the power of the R peak amplitude as the signal portion and the power of the segments between the QRS complex, the T wave and the P wave as the noise-only portion in the signal, as shown in Figure 2.10a. This analysis is performed similarly on ACC signals, considering two different signal portions (the absolute amplitude of S1 and the absolute amplitude of S2), and the noise-only portion is the segment between S1 and S2, as shown in Figure 2.10b. The SNR for a given beat was calculated using Equation (2.1). Then, the analysis is performed on all available heartbeats considering an average SNR.

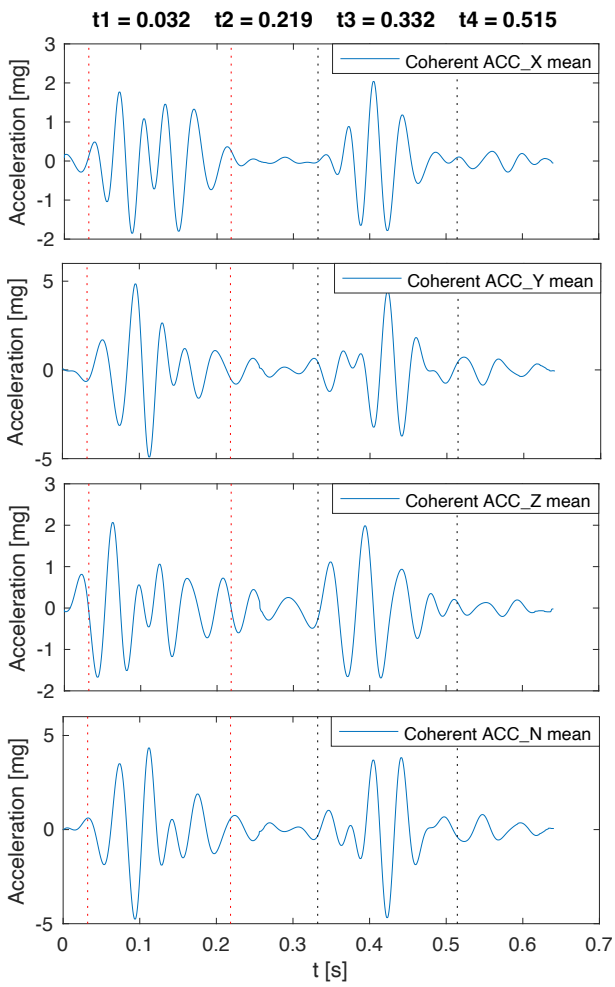

Figure 2.9 – Example of the final detection instants estimated for S1 and S2 on a representative recording. Vertical dotted lines represent the start and the end of S1 in red and S2 in black.

$$SNR = 10 \times \log_{10}\left(\frac{S^2}{\frac{1}{N}\sum_{n=1}^{N}|x_n|^2}\right) \tag{2.1}$$

where S is the signal portion value and x_n is a particular sample of the total N samples making up the noise-only portion of the signal.

Note that ECG signals were initially filtered to reduce the amplitude of P and T waves in the previously described processing framework. To facilitate comparison with other works in the literature, an alternative bandpass filter between 5 and 50 Hz was applied to the raw ECG signals, allowing visualization of the T and P waves. ECG signals filtered between 20 and 50 Hz are referred to as 'QRS-ECG', while ECG signals filtered between 5 and 50 Hz are referred to as 'TP-ECG'.

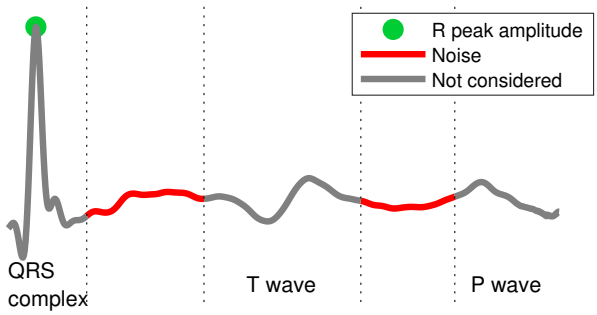

(a) Cardiac cycle in ECG signal

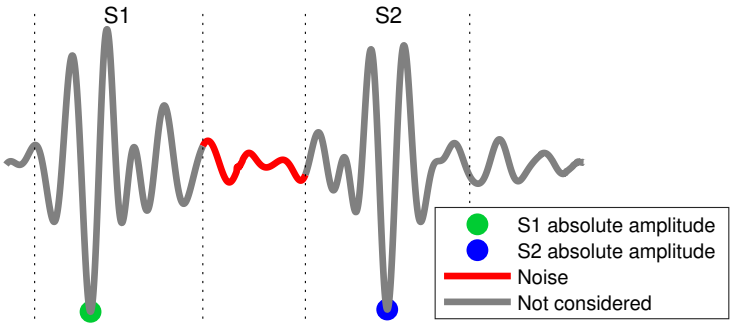

(b) Cardiac cycle in ACC signal

Figure 2.10 – Representation of the signal of interest and noise segments of the cardiac cycle to compute the SNR.

2.4 Validation with gold standard references

2.4.1 Validation of the ECG signals from the implant

In addition to the data processing chain explained above, other evaluation measures were applied to the surface and gastric data, with the aim of validating the gastric signals and obtaining results comparable with the literature in the field. Regarding ECG signals, comparisons were mainly focused on QRS detection and heart rate estimation. In a first step, QRS detection was applied to the reference surface signals and subsequently the obtained detections were manually reviewed to correct possible detection errors, in order to constitute the set of reference QRS instants. The quantitative QRS detection performance from the gastric site was estimated by calculating the sensitivity and positive predictive value (+P), compared to the reference QRS instants. A QRS detection from the implant signal is considered a true positive (TP) if it is within a 50 ms centered window from the corresponding reference QRS instant. All remaining implant QRS detections are considered false positives (FP). False negatives (FN) occur when no detection of the gastric site is found within the coincident reference window [145]. In addition, the time difference between a TP detection and its corresponding reference QRS instant (Jitter) is reported. All recordings acquired with the V0 prototype of the implant were used for this

comparison. A Wilcoxon rank-sum test was applied to statistically compare markers obtained from reference and gastric sites. In these analyses the significance level was set at 0.05.

2.4.2 Validation of the ACC signals from the implant

Regarding the ACC signals, all measurements were calculated with respect to S1 and S2 separately. The main objective is to compare the evolution of the derived markers acquired from the baseline PCG signal with those obtained from the intragastric ACC signals during the application of the Valsalva-like maneuver. Therefore, the quantitative marker used for comparison is the correlation of the time profiles of the main sound variables (duration and peak-to-peak values) with respect to those obtained from the reference PCG. The time profiles are created by measuring the heart sound variables throughout the entire recording. Time profiles associated with heart sound duration were calculated using a sliding window of four cardiac cycles. Concerning the implant ACC data, an average cycle per axis within the window was calculated and the global duration of the heart sounds was calculated by applying Algorithm 1 to estimate the final instants of detection for S1 and S2, yielding a global duration time-profile of the implant to be compared with the duration time-profile of the reference PCG. Moreover, time profiles of peak-to-peak values were calculated independently on each ACC axis of the implant by calculating the mean of the peak-to-peak values for each heart sound in a sliding window with the size of two cardiac cycles. Each peak-to-peak time profile of the implant was compared with the peak-to-peak time profile obtained from the PCG reference.

2.5 Results

2.5.1 Comparison of gastric and thoracic data

Validation of ECG signals

Figure 2.11 shows an example of ECG signals acquired from the thoracic (reference) and gastric sites. The ECG signals in this figure were bandpass filtered between 5 and 50 Hz and the mean coherent cycle of a representative recording is shown. The differences in signal morphology and amplitude between the surface and gastric devices are mainly explained by the significantly different dipoles observed. However, even in the shorter gastric dipole, the main ECG waves are easily identifiable and correct QRS detection can be expected for instantaneous heart rate estimation.

Table 2.2 shows the results of a quantitative comparison between ECG signals captured with the implant and external ECG signals taken as a gold standard reference. The estimated SNRs are significantly lower in the implant data with respect to the reference. This is to be expected, due to the different noise sources associated with the gastric site. In addition, sig-

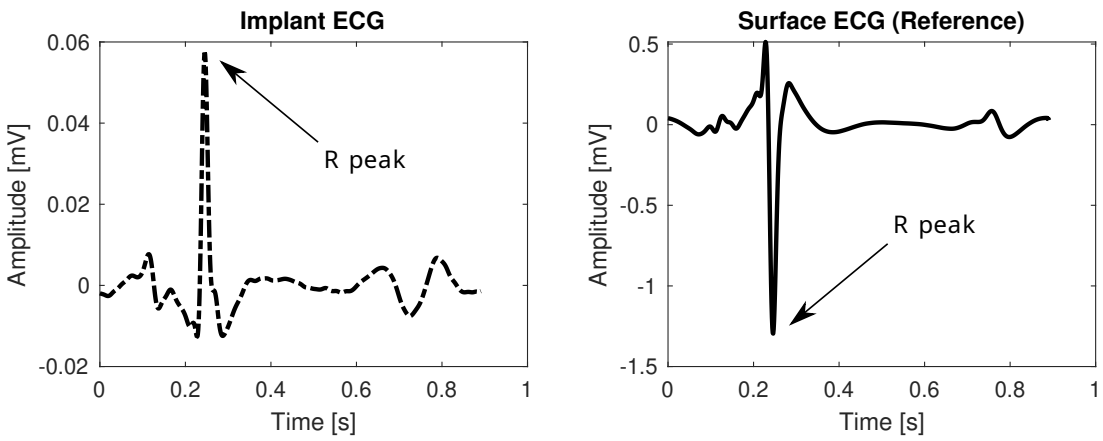

Figure 2.11 – Example of implant and gold standard ECG signals comparison. Dash-dotted lines correspond to the implant signals and solid lines correspond to the gold standard reference signals. Note that the differences in signal morphology and amplitude between the surface and gastric devices are mainly explained by the significantly different dipoles that are observed.

nificant differences are also observed between the values of the percentage of coherent cycles and the inter-cycle correlation, although both signals provide similar high and acceptable values for these markers. Finally, the sensitivity and positive predictive value for QRS detection are satisfactory, with a jitter lower than 10 ms. These results suggest that an adequate estimation of HR can be made from the gastric implant.

		Surface ECG	**Implant ECG**
TP-ECG SNR [dB]		28.4±3.4	21.6±7.5 *
QRS-ECG SNR [dB]		38.4±6.1	30.3±5.8 *
Coherent cycles percentage [%]		100.0±0.1	99.2±2.9 *
Inter-cycle correlation		0.98±0.01	0.94±0.05 *
QRS detection	**Sensitivity [%]**	97.6±4.7	
	+P [%]	98.2±3.5	
	Jitter [ms]	6.0±3.4	

Table 2.2 – Validation of ECG recordings with a gold standard reference. *p<0.05 vs. reference.

Validation of ACC signals

Figure 2.12 shows an example of the ACC cardiac signals taken from the gastric fundus and the respective reference PCG. The signals in this figure were bandpass filtered between 20 and 40 Hz. The reference PCG sensor observes cardiac vibrations at a different site, at a different angle and with a different transducer than the gastric site. This explains the differences in morphology between the PCG and ACC signals. However, from this first qualitative analysis we can hypothesize that the instant of occurrence of the heart sounds, as well as the relative variation of their amplitudes or energies between the CPP and apnea phases, could be correctly estimated from the gastric site.

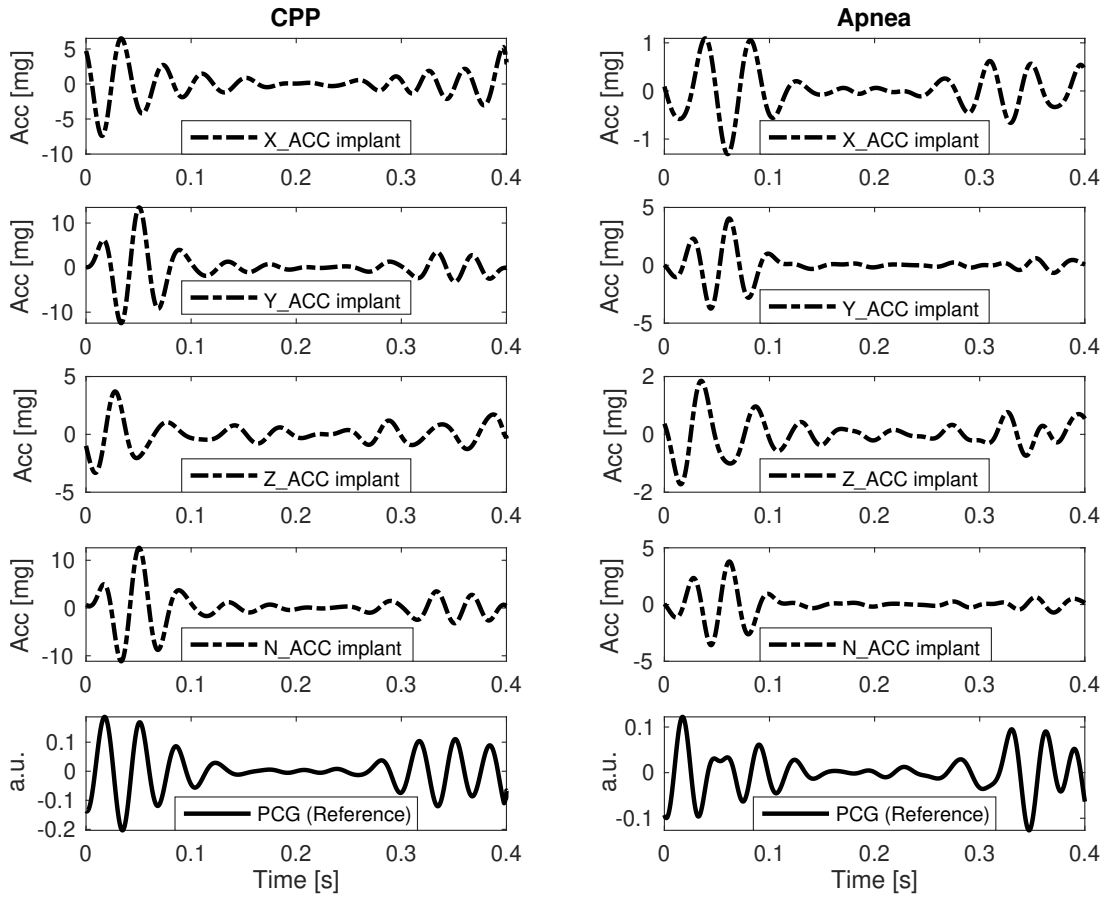

Figure 2.12 – Example of implant ACC and gold standard PCG signals comparison. Dash-dotted lines correspond to the implant signals and solid lines correspond to the gold standard reference signals. Coherent mean cycles of ACC and PCG signals during both respiratory phases taken from the recording 2.

The evolution of S1 and S2 duration from the CPP phase to the apnea phase is presented in Figure 2.13, while the evolution of peak-to-peak amplitude is shown in Figure 2.14. Similar dynamics can be observed between the ACC data acquired from the gastric site and the reference

PCG. However, it is possible to see how the similarity between the temporal profiles is perturbed mainly during the transition moment between the CPP and apnea phases, more precisely, around second 16. This perturbation is caused by a sudden increase in the noise picked up by the sensors during the transition moment between phases, and is more evident over S2 both in duration and peak-to-peak values, but mainly reflected over the Z-axis.

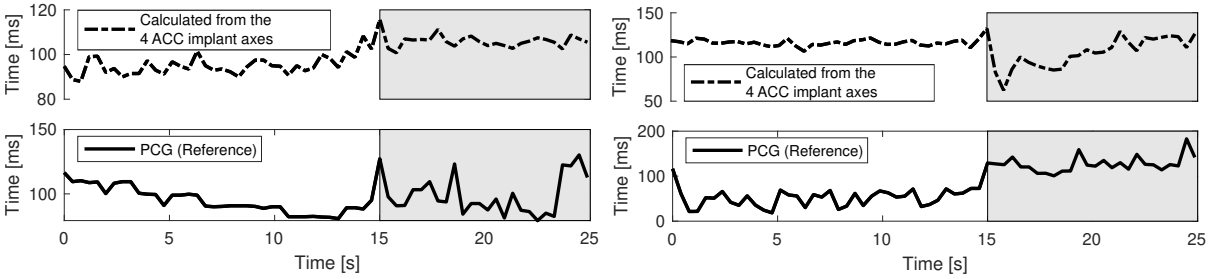

(a) Time-profile of S1 duration (b) Time-profile of S2 duration

Figure 2.13 – Evolution over time of heart sounds duration measured on the recording 1. Dash-dotted lines correspond to the implant signals and solid lines correspond to the gold standard reference signals. The white background corresponds to the CPP stage and the gray background corresponds to the apnea stage.

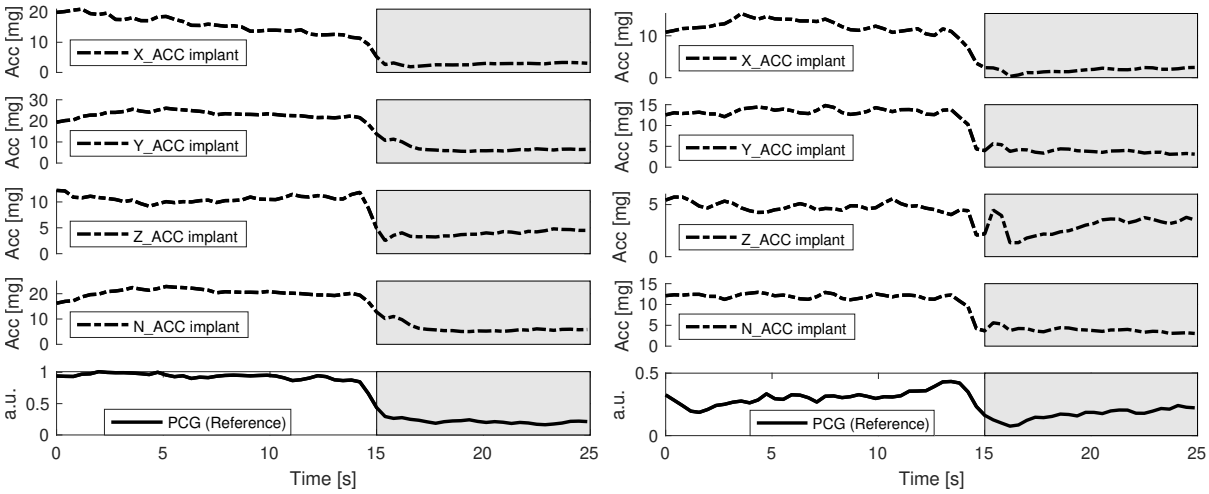

(a) Time-profile of S1 peak-to-peak value (b) Time-profile of S2 peak-to-peak value

Figure 2.14 – Evolution over time of heart sounds peak-to-peak value measured on the recording 1. Dash-dotted lines correspond to the implant signals and solid lines correspond to the gold standard reference signals. The white background corresponds to the CPP stage and the gray background corresponds to the apnea stage.

Table 2.3 shows quantitative results of the comparison between the implant ACC signals and the PCG reference. The correlation values between the temporal profiles of the duration of S1 and S2 are high and acceptable for both recordings, always presenting a higher correlation for S1 compared to S2. The algorithm proposed to estimate the final detection instants of S1 and

S2 by merging the local detections of all ACC axes of the implant (Algorithm 1) is of utmost importance in these results because it allows estimating the global times of S1 and S2, even if it is not possible to detect one of the heart sounds in any axis. Similarly, the time profiles of the peak-to-peak values show highly correlated values for all the implant axes, and mainly for the Y and Z axes, showing how the measurements made by the implant are highly correlated with the PCG reference during the entire recording time. These results suggest that an adequate measurement of the variation of CVS can be performed using the ACC data from the implant.

Time-profile	**Heart sound**	**Correlation between the implant and the PCG reference**							
		Recording 1				**Recording 2**			
		X	**Y**	**Z**	**N**	**X**	**Y**	**Z**	**N**
Duration	**S1**	0.991				0.961			
	S2	0.874				0.950			
Peak-to-peak value	**S1**	0.988	0.996	0.989	0.994	0.959	0.975	0.987	0.975
	S2	0.918	0.956	0.971	0.958	0.877	0.888	0.962	0.887

Table 2.3 – Validation of ACC recordings with a gold standard reference.

2.5.2 Estimation of longitudinal markers from gastric ECG and ACC data

Evaluation of signal quality

Table 2.4 shows the results of the recordings removed at each stage of the quality analysis, and the recordings saved for further analysis. These results show that it was possible to identify coherent cycles in most of the signals, with only 1.8% of the recordings having to be removed because they did not have enough coherent cycles in the ECG or ACC signals. This low rejection rate reflects a good QRS detection process and correlation analysis, which opens the possibility of performing basic heart rate variability analysis using this technology. Most of the deleted recordings corresponded to stages 2 and 3, with rejection rates of 12.0% and 18.1%, respectively. These percentages mainly reflect the complexity to identify and suppress all the different types of noise sources present in the ACC data (such as pig growls and digestive sounds and movements), basically because stages 2 and 3 removed recordings where the noise level is so high that it prevents detecting S1 and S2 correctly. After this quality assessment process, 68.1% of the total data were preserved. For these preserved recordings, the quality of the data allowed successful detection of S1 and S2 in all four axes, favoring the possibility of identifying useful and reliable hemodynamic markers from these signals by having more reliable information sources.

Pig ID	Total number of recordings	Removed at stage 1		Removed at stage 2		Removed at stage 3		Recordings finally preserved	
		#	%	#	%	#	%	#	%
1	95	0	0.0%	18	18.9%	18	18.9%	59	62.1%
2	163	7	4.3%	22	13.5%	23	14.1%	111	68.1%
3	232	2	0.9%	16	6.9%	39	16.8%	175	75.4%
4	316	7	2.2%	40	12.7%	61	19.3%	208	65.8%
5	70	1	1.4%	10	14.3%	12	17.1%	47	67.1%
6	73	0	0.0%	4	5.5%	18	24.7%	51	69.9%
7	50	1	2.0%	10	20.0%	10	20.0%	29	58.0%
Total	999	18	1.8%	120	12.0%	181	18.1%	680	68.1%

Table 2.4 – Summary of the signal quality results.

Although these results reveal challenges in exploiting a larger percentage of the acquired data, it is worth noting that continuous data acquisition throughout the day in the context of monitoring chronic diseases such as HF is unnecessary. Figure 2.15 shows the distribution of rejected and retained recordings over time, revealing that the rejected signals are spread across all acquisition days for all pigs, allowing several useful recordings to be retained during each day. Furthermore, it can be seen how the percentage of retained recordings exceeds 60% for 6 of the 7 pigs regardless of whether they are healthy or pathological. Where the lowest percentage was obtained by the last pig (58%), but it is still comparable with the other pigs in terms of the distribution of preserved recordings over time, considering also that pig 7 had the lowest amount of available recordings.

Analysis of heart rate variability (HRV)

Estimation of the final instants of detection of S1 and S2 allows analysis of the duration of the different phases of the cardiac cycle, such as systole, diastole and S1 and S2 duration, where systole begins at $t1$ and ends at $t3$, and diastole corresponds to the total duration of the cycle minus systole [23]. Table 2.5 presents the mean and standard deviation of these variables for each pig. These results justify the procedure to detect S1 in the first half of the cardiac cycle because the mean S1 duration is statistically lower than half of the total mean cycle duration for all pigs, ensuring that the S1 duration is not restricted by the searching space.

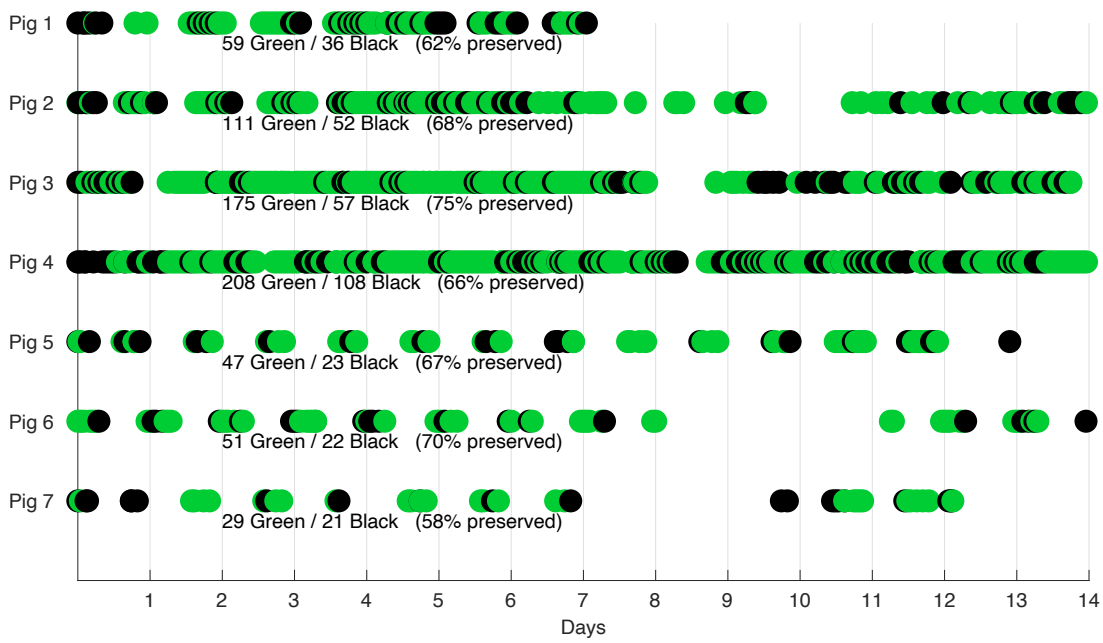

Figure 2.15 – Signal acceptance distribution over time. Green dots represent the recordings finally preserved, black dots represent all discarded recordings.

Pig ID	**Heart rate** [BPM]	**Total Cycle duration** [ms]	**Systole duration** [ms]	**Diastole duration** [ms]	**S1 duration** [ms]	**S2 duration** [ms]
1	92±19	675±124	291±51	384±102	168±31	184±38
2	89±22	711±155	297±67	414±124	152±31	170±41
3	92±16	668±99	297±64	371±93	142±33	167±42
4	98±17	629±95	276±45	352±76	153±28	172±36
5	77±20	819±174	366±113	453±149	189±36	192±49
6	63±9	966±132	358±71	608±137	199±34	173±34
7	74±17	849±169	383±100	466±175	199±27	191±43
Total	89±20	704±155	303±73	401±127	159±36	174±40

Table 2.5 – Statistics of cardiac cycle duration.

Additionally, it is possible to discern a HR-related pattern between healthy and pathological pigs, where the 4 healthy pigs exhibit a higher HR than the 3 pathological pigs. This pattern is best observed in Figure 2.16 through the scatter plot of the recordings relating HR, systole and diastole duration. A graphical representation of the mean and standard deviation of each of these variables is also included. Although this pattern is evident in the data, it is not statistically

supported to classify the pigs as healthy or pathological, considering all the variables that can influence HRV such as age, gender, weight, etc., and the limited number of pigs involved in the experiment.

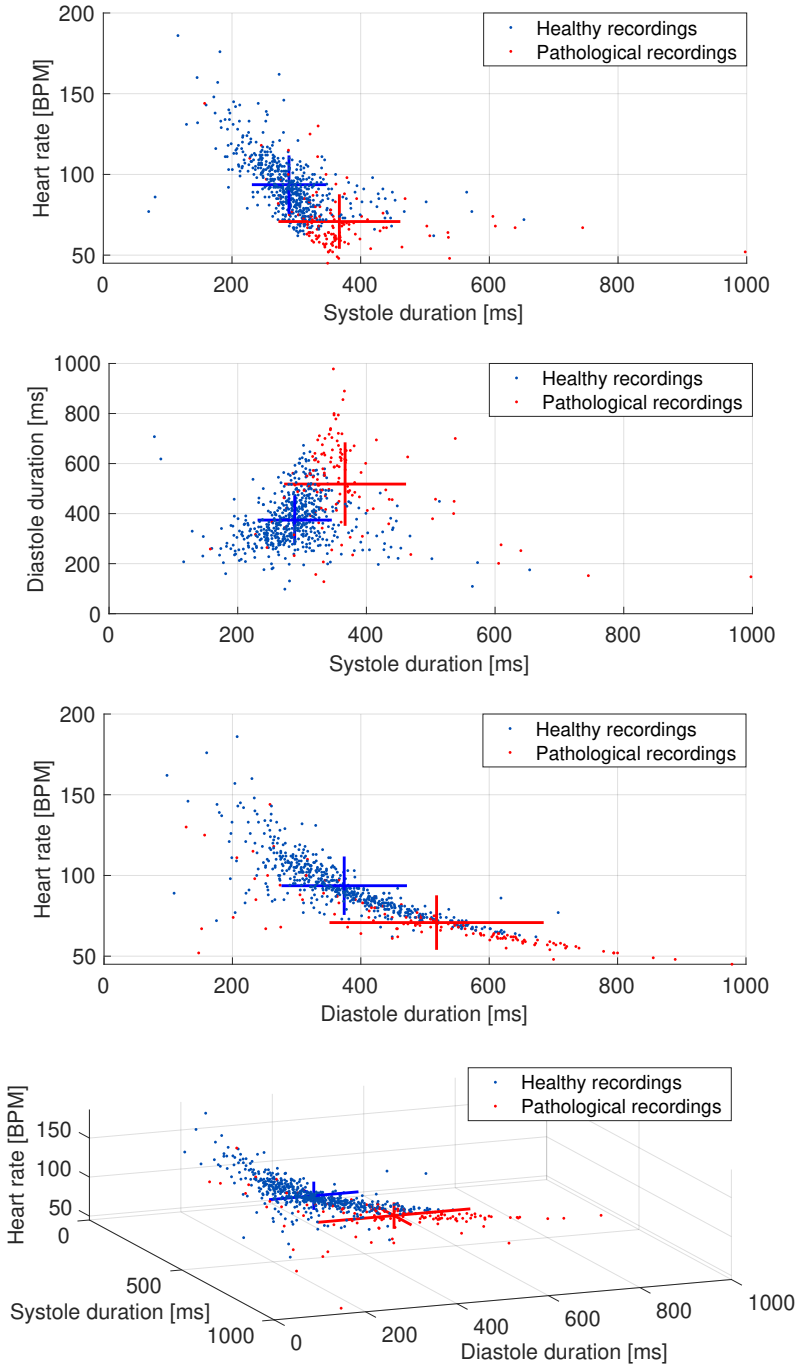

Figure 2.16 – Scatter plot of the cardiac cycle duration between healthy and pathological pigs. The crosses represent the mean and standard deviation of each population along the two axes.

Analysis of S1 and S2 morphology

The most relevant aspect to analyze regarding the estimation of hemodynamic markers is the morphology of S1 and S2, i. e., the duration and amplitude of these cardiac components. Figures 2.17 and 2.18 show through box plots and scatter plots the statistical distribution of the data according to the peak-to-peak values and the duration of S1 and S2, respectively. In order to condense the information of the peak-to-peak values of the 4 ACC axes, it was decided to calculate a magnitude measure using the Euclidean norm of the peak-to-peak values of the 4 ACC axes. Furthermore, this process ensures that even recordings missing one or more of their ACC axes can be included in the analysis.

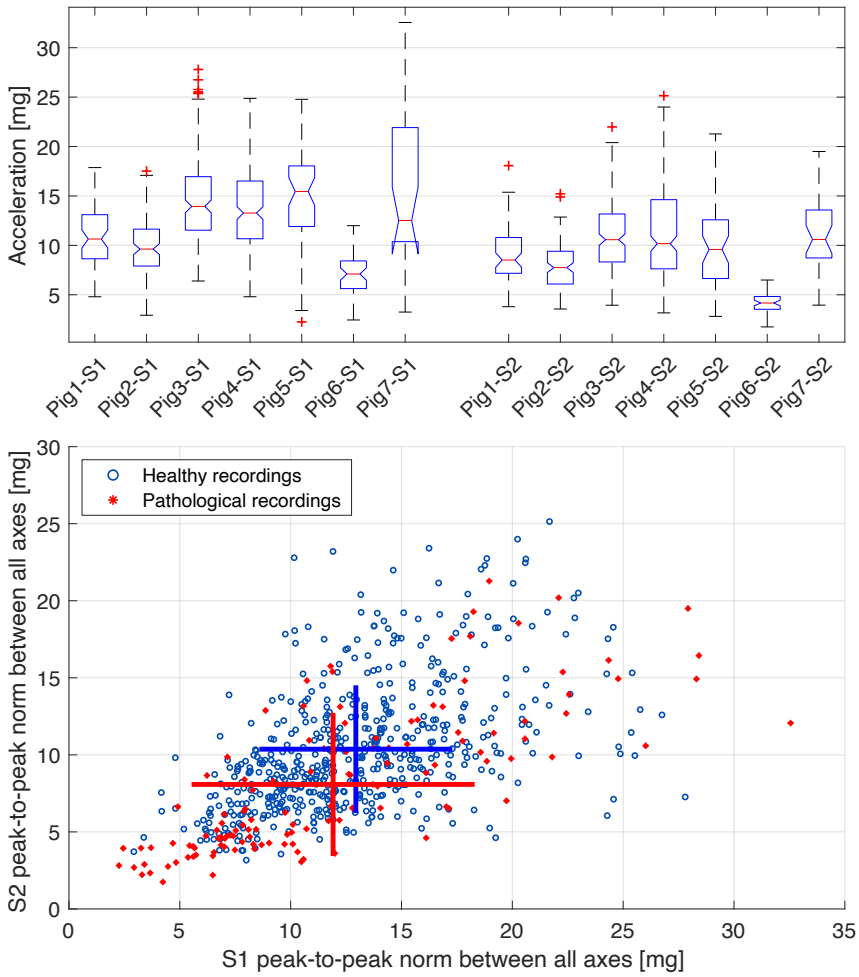

Figure 2.17 – Statistical distribution and scatter plot of the norm of peak-to-peak values between all ACC axes of S1 and S2 between healthy and pathological pigs. The crosses in the scatter plot represent the mean and standard deviation of each population.

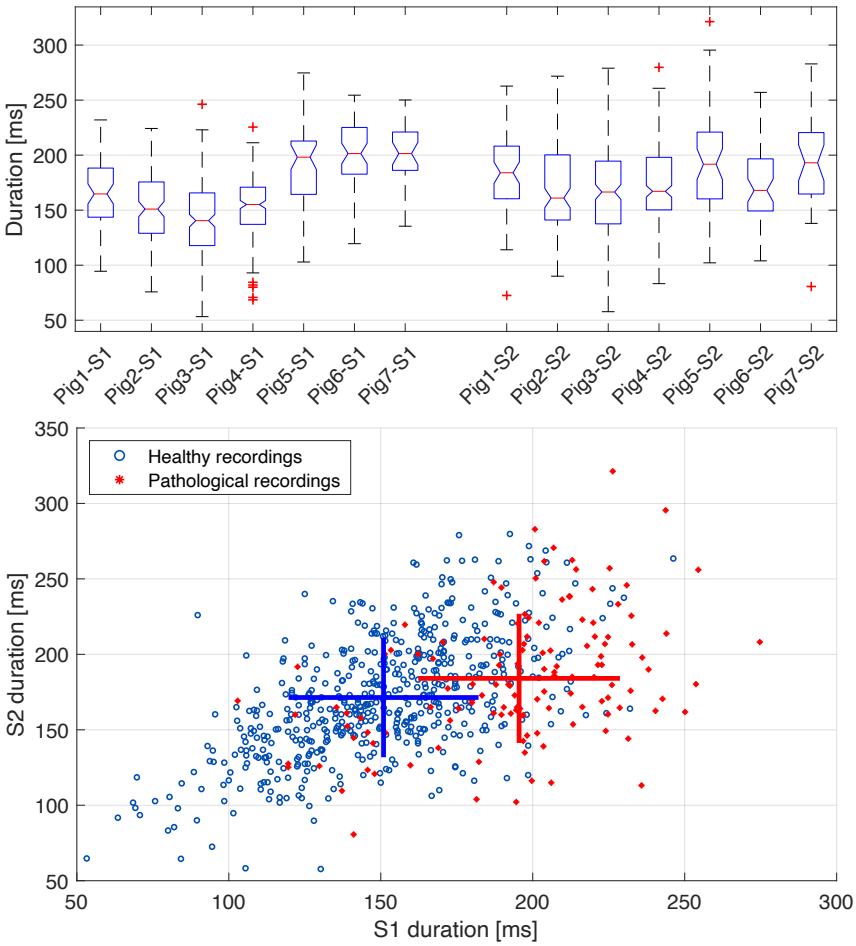

Figure 2.18 – Statistical distribution and scatter plot of the duration of S1 and S2 between healthy and pathological pigs. The crosses in the scatter plot represent the mean and standard deviation of each population.

The results in Figure 2.17 show that the median peak-to-peak values of S1 are slightly higher than those of S2 for all pigs, which is consistent with the literature in both PCG and SCG [40, 146, 90]. The scatter plot of peak-to-peak values suggests a reduction in the magnitude of pathological recordings, and is shown in S1 and S2. The difference between healthy and pathological pigs is most notable concerning the duration of S1 and S2 shown in Figure 2.18, especially for S1, where the notches in the box plot do not overlap, concluding with 95% confidence, that the true medians of S1 duration between healthy and pathological pigs do differ. These differences in peak-to-peak values and heart sound duration are expected between healthy and pathological pigs. Indeed, it has been previously reported that modifications of the inotropic state, which is particularly affected in HF, have a direct consequence on the amplitude and duration of S1 [8, 17].

Analysis of SNR results

Table 2.6 shows the mean value and standard deviation of the SNR measurements of all cardiac cycles in the ECG and ACC signals. The SNR measurements obtained for the ECG signals show the highest values in the QRS-ECG configuration, which was also presented with the SNR values of the gold standard signals in Table 2.2. Such phenomena are evident because the cutoff frequency values used for the QRS-ECG configuration were more restricted than the values used for the TP-ECG, thus suppressing more of the noise in the signals and highlighting the R peak, which was the purpose of using both configurations at different stages of the processing pipeline. These values are also comparable with those found in the literature [147, 148].

Pig ID		**1**	**2**	**3**	**4**	**5**	**6**	**7**	**All**
ECG	**TP**	14.7±5.3	17.3±6.1	15.8±6.1	16.2±5.7	15.8±6.6	22.2±6.2	21.6±5.9	17.6±6.0
[dB]	**Rpeak**	21.0±4.0	22.9±5.1	22.3±4.3	21.2±3.8	23.5±5.7	31.0±6.3	25.4±5.3	23.9±4.9
	X	13.2±5.3	15.3±5.7	14.9±5.8	14.5±5.9	15.4±6.4	17.7±5.3	16.7±6.6	15.4±5.9
S1	**Y**	14.3±5.5	16.0±6.1	14.4±5.5	15.8±5.8	15.9±6.4	18.2±5.5	18.2±6.7	16.1±5.9
[dB]	**Z**	14.3±5.7	15.7±5.8	15.9±5.5	15.5±6.1	16.7±6.9	17.9±5.3	17.9±6.2	16.3±5.9
	N	15.1±5.4	15.8±6.0	15.1±5.5	15.4±5.8	15.8±5.8	17.2±4.7	19.4±6.3	16.3±5.6
	X	9.7±5.3	11.0±6.0	10.6±5.6	9.8±5.7	10.8±6.3	13.7±5.7	13.1±6.5	11.3±5.9
S2	**Y**	10.3±5.4	12.5±6.1	10.7±5.8	11.9±6.4	11.9±6.8	13.0±6.2	14.7±7.3	12.1±6.3
[dB]	**Z**	10.1±5.3	11.6±5.8	11.4±5.5	11.9±6.2	12.2±6.6	11.8±5.6	13.7±5.9	11.8±5.8
	N	11.2±5.4	12.0±6.0	11.5±5.9	11.4±6.0	11.7±5.8	12.5±5.1	14.7±6.2	12.1±5.8

Table 2.6 – SNR of ECG and ACC signals.

The SNR results of the ACC signals represent a satisfactory signal quality compared to the literature [149, 150, 126]. Although there are some differences in the equations used to calculate SNR in ACC signals in the literature, the results may be comparable in terms of the ratio given in dB. The mean SNR of S1 is higher than the SNR of S2 because the absolute amplitude of S1 is usually larger than the absolute amplitude of S2 and both values are measured against the same signal background noise.

2.6 Discussion

This chapter presented, to our knowledge, the first characterization of electrophysiological and 3D accelerometer cardiac data acquired from the gastric fundus in preclinical experimentation. The results obtained in Phase 1 showed satisfactory levels of correlation between markers obtained from the gastric implant and those obtained from standard surface sites. In particular, the time variation of markers such as heart rate and heart sound duration and amplitude were

highly correlated with the reference, which is the main focus of the proposed device for long-term monitoring of chronic diseases such as HF [6, 151, 26]. Although these results were obtained from a limited number of observations and may warrant further comparisons, we consider them sufficient to move forward with the feasibility study in Phase 2.

Results related to the estimation of longitudinal digital markers from the implant showed that the electrophysiological sensors contain a mixture of different bioelectrical sources, mainly ECG, electromyographic, electrogastrographic and impedance modifications at the electrode-tissue interface due to respiratory, gastric and general animal movement. In general, the SNR is high enough to perform robust QRS complex detection and basic HRV analysis from these electrophysiological signals. Concerning the acquired CVS, the main sources of noise are pig growls, as well as digestive sounds and movements. These sources cause an abrupt reduction in the SNR and signal contrast of the ACC data that can drop below 5 dB and 2, respectively. This fact is directly reflected in the high percentage of rejected recordings in the second stage of the quality assessment process, which depend on a contrast level higher than 2. Respiratory movement and general motor activity of the pig are also observable, but can be more easily attenuated or cancelled. Therefore, a data quality assessment phase has been proposed to select a subset of the acquired data that contains exploitable information.

When SNR values higher than 6 dB or heart sound contrast higher than 2 are observed, the S1 and S2 components can be correctly segmented from the accelerometer signal and hemodynamic markers can be estimated from these data. The values obtained associated with the morphology of S1 and S2 are in agreement with the literature in the field, in terms of the duration [152, 24] and amplitude [40, 140] of both cardiac components. Furthermore, considering that previous studies have correlated S1 amplitude with left ventricular dP/dt [8, 9, 16, 17], it is worth noting that S1 showed a lower mean peak-to-peak value and longer duration in HF pigs relative to healthy pigs, indicating a possible negative inotropic function of HF pigs. Modifications in S2 between HF and normal pigs are also observed. However, these results have no statistical significance at this stage and further preclinical evaluations should be performed, using exactly the same instrumentation in both groups. Nevertheless, the qualitative correspondence between the results obtained and those in the literature, highlights the feasibility of deriving reliable and traceable markers related to hemodynamic alterations associated with heart failure from the gastric fundus.

Regarding the information obtained from the implant, the change in orientation over time represents an interesting aspect, which was considered as a prospective source of information (results not included in this work). Since the device is correctly fixed to the gastric fundus, these orientation changes are not related to the movements of the device inside the stomach (which would be an important source of error), but to the movements of the coupling between the heart, the diaphragm, and adjacent gastric structures. In addition to compensating for these movements, the accuracy of an implantable 3D accelerometer can be used to extract potentially

valuable information. Further work is being done in this direction. It is worth mentioning that some technical issues related to the construction of the implant prototypes need to be addressed in future versions. Some of the main issues identified are listed below:

— Occasionally, the implant was restarted for reasons unrelated to the acquisition protocol and the schedule was no longer available.

— The application on the gateway was not robust enough. It was necessary to restart the gateway to restart the application. If this action was performed too late, some data was lost.

— The cloud infrastructure was only in the first release for proof of concept and was not continuously stable.

2.7 Conclusion

This chapter shows initial preclinical evidence on the feasibility of chronic cardiovascular monitoring from a minimally invasive implantable cardiac device placed in the gastric fundus. The main challenge remains in optimizing the signal-to-noise ratio, in particular for handling some noise sources that are specific to the gastric acquisition site. Ongoing work is aimed at proposing adaptive methods that will trigger data acquisition at the implant when specific noise level criteria are met and in further preclinical evaluation.

Furthermore, an efficient and easy-to-implement algorithm based on context features was designed to obtain the final detection instants for S1 and S2 from the fusion of multiple candidate detections of the main ACC events from a 3D accelerometer (Algorithm 1), with the additional advantage of allowing the easy incorporation of other CVS sources such as PCG and gyrocardiogram (GCG). This algorithm uses the contrast measurements of the cardiac events to define the final detection instants for S1 and S2 as follows: 1) each detection instant is replicated in the four ACC axes to analyze its overall performance by calculating the corresponding contrast of that detection in each axis. 2) Detections with a contrast value lower than 2 are discarded on the corresponding axis. 3) Two relevance vectors are created using the contrast measures, one for S1 and one for S2, where the higher the contrast measure, the higher the relevance value assigned to the corresponding detection. 4) A weighted average is calculated between the detection instants using the relevance vectors as weights. The result of this weighted average operation is used as the final detection of S1 and S2.

Chapter 3

Cardiorespiratory event detection using a MEM system with an embedded machine learning core

As previously stated, a great interest has aroused in the last decade for the analysis of cardiac vibration signals (CVS) [79, 27, 108]. Specific signal processing and machine learning methods have been proposed to exploit this type of signals, that carry a large amount of information about the cardiorespiratory function. Signal processing and machine learning pipelines start to emerge in the literature to address some of the most sensitive cardiovascular pathologies, such as HF [153, 113, 112]. However, the implementation of these pipelines in real-time and "on-the-edge" (the closest possible to the patient, into the sensors), still remains a major challenge. This chapter describes the design, development, calibration, operation and preliminary evaluation of a prototype acquisition system developed to synchronously measure the mechanical, electrical and phonographic signals of the heart, using specialized sensors with high performance characteristics. The main feature of such a system is the possibility to integrate a machine learning core (MLC) into the MEM sensor, that is intended to be used to automatically detect different cardiorespiratory events "on-the-edge". Initial feasibility tests for the evaluation of such on-the-edge implementation are also reported in this chapter.

3.1 Design and development of the cardiac signal acquisition system prototype

There is no doubt that the modern world is awash in an ocean of data, and new data continues to be constantly acquired in huge quantities through the use of all kinds of sensors and IoT (Internet of Things) devices. This trend has been reflected in all fields of industry, science and research, including the medical field, leading to the development of new technologies that seek to better manage data in terms of storage, speed, security and overall efficiency. The

term "on-the-edge" has been established as part of these new developments, referring to a new distributed data architecture called "edge computing", where information is processed as close as possible to the source of the data [154]. Additionally, the use of artificial intelligence, or more specifically the use of machine learning algorithms, has also exploded as part of this trend towards the era of data, producing a large number of new approaches every day that demonstrate the enormous potential that this type of technology offers when dealing with the need to process large amounts of information with high performance results [155].

Many works involve the use of machine learning algorithms in the context of remote monitoring of cardiac patients, most notably those that leverage the use of sensors commonly embedded in smartphones (such as accelerometers and gyroscopes) to develop what so far look more like on-the-edge approaches [27, 108]. However, these approaches still lack features that should be considered for chronic and longitudinal monitoring of patients with diseases such as HF, especially those who require the use of implantable devices or who simply cannot adjust to the manipulation of a device such as a smartphone [156]. In this work, we propose the development of a cardiac signal acquisition system that will incorporate the measurement of CVS through the use of a cutting-edge MEM sensor, which has the special feature of integrating an MLC that allows deploying machine learning applications on-the-edge. Such a feature raises the hypothesis that this type of technology could be exploited for the future development of implantable or wearable devices for monitoring cardiac patients, with the advantage of enabling the use of machine learning on-the-edge to improve the efficiency of such devices in terms of real-time processing, speed, memory, size, power consumption, and even accuracy.

The developed cardiac signal acquisition system is capable to measure mechanocardiographic (MCG), electrocardiographic (ECG) and phonocardiographic (PCG) signals synchronously in a noninvasive manner. The system consists of a main board and three independent modules associated with each of the three types of measured signals. The main board is in charge of data storage and synchronization control of the different signals. The MCG module consists of the cutting-edge MEM sensor used to measure the CVS, which is composed of a 3D seismocardiogram (SCG) and a 3D gyrocardiogram (GCG). The ECG is primarily taken to accurately determine the trigger of major cardiac events by detecting R-peaks, while the PCG is measured to be used as a gold standard reference to validate the effective correlation between the cardiac vibrations captured by the MCG and the main heart sounds, which are widely studied in the literature.

Figure 3.1 shows a general diagram of the system design. An important detail in this figure is the clear representation of the on-the-edge definition to different extents. For instance, the PCG sensor (corresponding to the electronic stethoscope) only sends the measured signal to the main board without receiving any programming information that can configure the parameters of this signal. The ECG chip, on the other hand, receives programming data that allows configuring

the parameters of the signal while returning both the measured ECG and the R-peak detection, through on-the-edge ECG processing. Finally, the MCG sensor also receives the programming data from the main board, while playing the role of transducer and returning the measured signals as well as the MLC output, which is produced by processing the SCG and GCG signals on-the-edge.

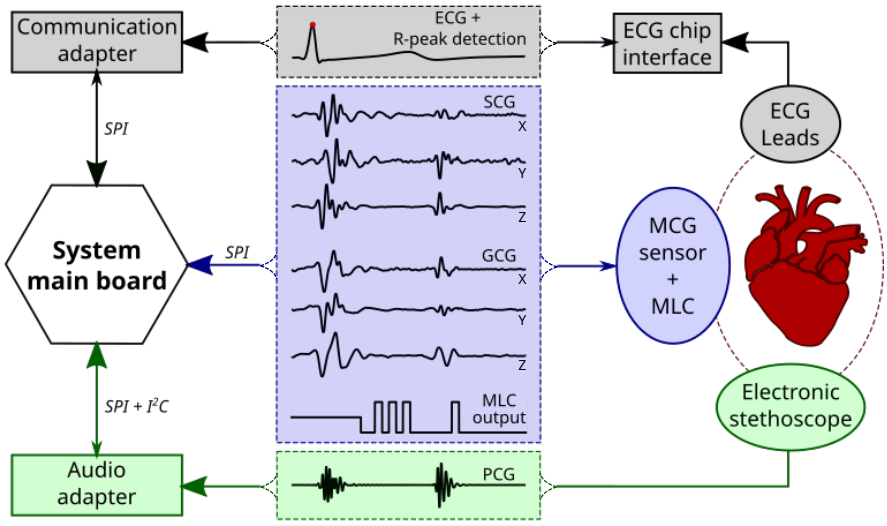

Figure 3.1 – Global diagram of the system design. The small arrows represent the flow of programming data to the system peripherals, while the large arrows represent the flow of data from the signals acquired by the sensors. The gray, blue and green colors represent the components of the ECG, MCG and PCG modules, respectively. The dotted rectangular shapes provide a visualization of the signals transmitted by each module, while the solid rectangular and oval shapes represent the adapters and transducers, respectively.

The system prototype is designed to be as compact as possible, so that it can be easily transported and installed within the different data acquisition environments for which it may be required. The main challenges in the design of the system are associated with this aspect, since the choice of a compact and practical design poses limitations in terms of computational and hardware capacity of the main board, considering that it must be able to receive all the data coming from the different modules in real time, in a synchronized manner, without loss of information, and in a reliable manner. The communication protocols used to connect the main board with the different modules were selected according to the following considerations:

— The hardware availability of the main board and of each of the sensors.

— The sampling frequency required by each module, which varies between each type of sensor due to the nature of the measured signals.

— The requirements for the synchronization of all signals acquired by the system. In fact,

a particular effort has been given to the correct temporal synchronization of the signals, acquired through different sensors, with different protocols and heterogeneous resolutions.

3.1.1 System main board

The acquisition system has a centralized configuration with a main board and 3 different modules assigned to specific functionalities. All modules are connected to the central board where the data is stored. The board used is a Raspberry Pi version 3 model B+ (see Figure 3.2), which belongs to a series of low-cost single board computers developed by the Raspberry Pi Foundation. The Raspberry Pi 3 B+ features a 1.4Ghz 64-bit quad-core ARMv8 processor, Wi-Fi and Bluetooth wireless connectivity without the use of additional adapters. The Wi-Fi connection features dual-band 2.4GHz and 5GHz, plus a 300 Mbit/s Ethernet port.

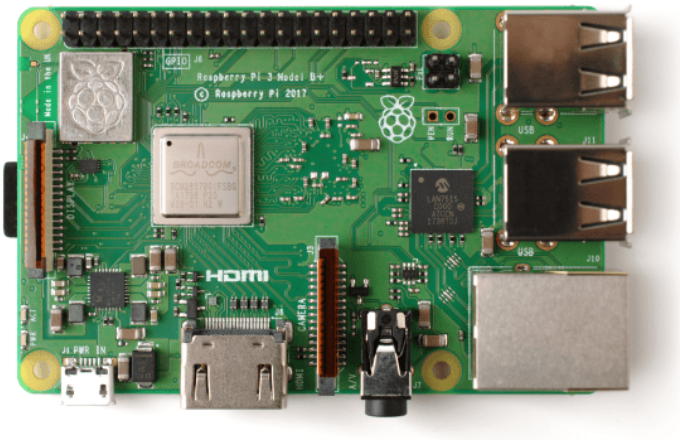

Figure 3.2 – Raspberry Pi version 3 model B+. Reprinted from [157], copyright ©2022 Raspberry Pi.

The main reasons for using this board in this project are its versatility and ease of use with the ability to integrate sensors using low-level communication protocols such as I^2C, SPI, UART and GPIO pin control. Additionally, this board allows the use of high-level programming languages such as Python, which is an open source language that offers high interpretability of the code structure, with a large number of libraries supported and updated by the developer community and applied to numerical operation, peripheral control and machine learning, which is in line with the main objective of this project.

3.1.2 PCG acquisition module

This module corresponds to the audio acquisition interface that captures the phonographic signals from the heart (outlined in green in Figure 3.1). Considering that the default 3.5 mm connector of the Raspberry Pi board only provides output functionality, it was necessary to use

an additional adapter that integrates an audio input functionality to capture the signals coming from the sensor. The best option to consider was the specialized HifiBerry DAC+ ADC Pro board (see Figure 3.3). The HifiBerry DAC+ ADC Pro is a high-resolution digital-to-analog and analog-to-digital converter for Raspberry Pi models with 40-pin GPIO connector such as Raspberry Pi 3 B+. This sound card is specifically optimized for applications that need not only playback but also recording functionalities [158], meeting the requirements of this project.

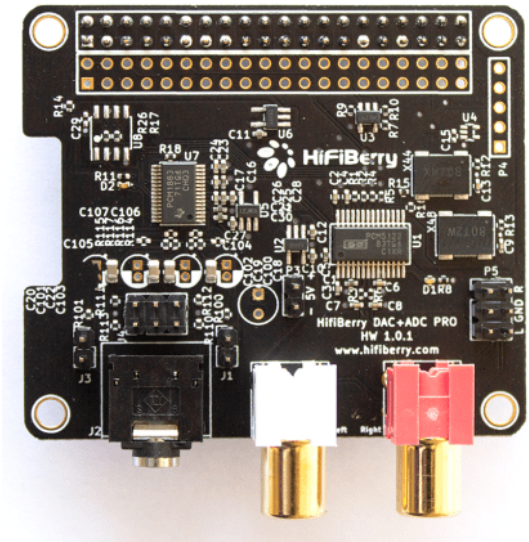

Figure 3.3 – HifiBerry DAC+ ADC Pro. Reprinted from [158], copyright ©2022 HiFiBerry.

The HifiBerry DAC+ ADC Pro comes as a pre-built kit and can be connected directly to the Raspberry Pi because it complies with the Raspberry Pi hardware-attached-on-top (HAT) specification. This board requires exclusive use of the I^2C bus and one of the two SPI buses of the Raspberry Pi main board, leaving only one SPI bus free to connect to the other sensors. Despite this limitation, the HifiBerry DAC+ ADC Pro was chosen as the audio input adapter for the project because it was still possible to connect the other sensors using the remaining communication ports. Following the premise of developing a handy and compact system, it was decided to implement an electronic stethoscope featuring a 3.5 mm connector that would be practical to transport and use in any signal acquisition environment (see Figure 3.4).

3.1.3 ECG acquisition module

The second module is designed to measure the ECG signals (outlined in gray in Figure 3.1). The sensor was carefully selected to meet the requirements needed to be used in a clinical setting, this sensor is the MAX30003. This sensor is a complete biopotential analog front-end solution for portable applications, offering high performance for clinical and fitness applications.

Figure 3.4 – Electronic stethoscope.

The MAX30003 provides ECG waveforms and automatic, embedded, R-peak detection based on the Pan Tompkins algorithm for heart rate analysis [159]. The MAX30003WING expansion board was used to create the interface connection between the MAX30003 and the Raspberry Pi (see Figure 3.5a). This board provided a 3.5 mm connector for prototyping with ECG leads compatible with this interface. Additionally, an FT232H adapter was used to create a new SPI port through one of the USB ports of the Raspberry Pi with the purpose of preserving SPI bandwidth and minimize conflicts with other SPI communications. The FT232H is a high-speed (480 Mb/s) single-channel USB 2.0 to UART/FIFO IC adapter (see Figure 3.5b), it has the ability to be configured on a variety of industry standard serial or parallel interfaces such as SPI, I^2C, UART and GPIO pin control.

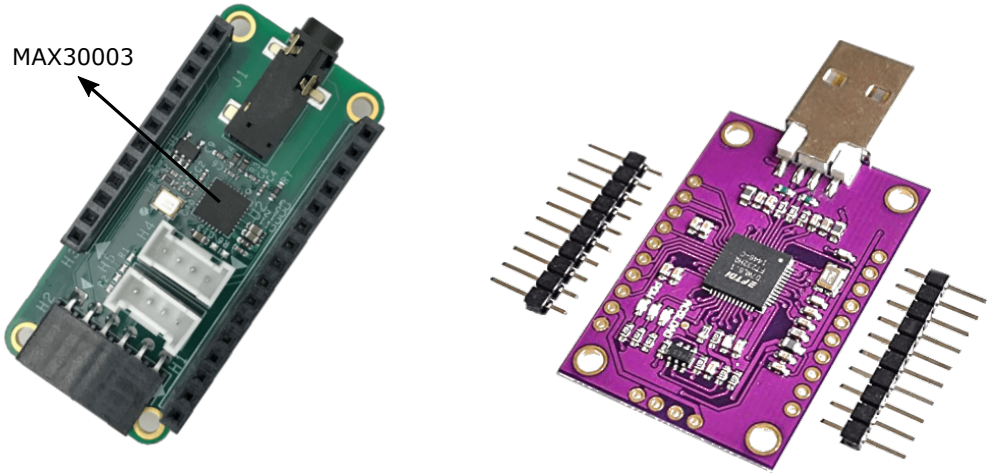

(a) MAX30003WING expansion board (b) FT232H USB to UART/FIFO IC adapter

Figure 3.5 – Main components of the ECG acquisition module.

3.1.4 MCG acquisition module

The third module corresponds to the sensor for measuring CVS (outlined in blue in Figure 3.1), and following the proposal to use sensors that stand out for their high performance and measurement accuracy, the LSM6DSOX was chosen. The LSM6DSOX is a MEM sensor featuring a 3D digital accelerometer and a 3D digital gyroscope with a current consumption of 0.55 mA in high performance mode. It also offers the possibility to connect and process data from external sensors (such as a magnetometer) using the "Sensor Hub function". The LSM6DSOX is developed by STMicroelectronics [160], offering real, virtual and batch sensors with 9 kbytes for dynamic data batching. This sensor can be configured from the Auxiliary SPI and primary interface (SPI / I^2C & MIPI $I3C^{SM}$).

The main reason for choosing the LSM6DSOX in this project is because it has an embedded machine learning core (MLC), opening the possibility to develop some machine learning applications that could be executed by the sensor instead of the microprocessor. This functionality offers benefits in terms of processing time, power consumption, size, cost and complexity in the development of a final implantable or external cardiac device. The MLC integrated into the LSM6DSOX allows identification of whether a data pattern (e.g., motion, pressure, temperature, magnetic data, etc.) matches a user-defined set of classes. The MLC works with data patterns from accelerometer, gyroscope and external sensors. Input data can be filtered using a dedicated configurable computation block containing filters and functions calculated in a fixed user-defined time window without overlapping. Machine learning processing is based on logic processing composed of a series of configurable nodes characterized by "if-then-else" conditions where feature values are evaluated against defined thresholds (decision tree logic).

One of the main issues raised at the beginning of the project was the need to design a custom lead to connect the LSM6DSOX sensor in a manner that would be comfortable for the patient, easy to install and would not limit its measurement sensitivity. The evaluation or acquisition boards available on the market with the sensor already installed were too large to fit the requirements of the project, because a too large board would imply the addition of an extra mass that would limit the sensitivity of the sensor. For this reason, it was decided to design and build a custom board with a minimum size to take full advantage of the LSM6DSOX sensor features. The custom board was designed following the recommendations of the manufacturer, taking special care to install the decoupling capacitors as close as possible to the power pin of the sensor. The board design includes eight through-hole connection terminals to connect the board via low-stiffness wires that allow the sensor to retain its high sensitivity in vibration measurement. Figure 3.6a shows the printed circuit board (PCB) layout, which has dimensions of 10.38×12.27 mm. The PCB was printed by contracting the services of a company specialized in printing this kind of circuits (see Figure 3.6b), and the components were soldered in the lab facility. The resulting final board is shown in Figure 3.6c.

(a) PCB design (b) Printed custom board (c) Mounted custom board

Figure 3.6 – LSM6DSOX custom board design.

After mounting the components on the customized board, a female snap for the connection of an electrode was glued to the back of the board. This was for the purpose of being able to easily attach the sensor to the chest of the patient by using a traditional electrode like the ones used for ECG leads, but in this case without electrical conduction, only to easily fasten the sensor. Subsequently, the board with the electrode snap was coated with a two-part liquid silicone composition especially designed for electrical protection in medical applications. The liquid silicone is formed by thoroughly combining the two components, which do not present any risk of generating an exothermic reaction. The encapsulated custom board is 18 mm in diameter, 8 mm thick and weighs approximately 4 grams. It is shown in Figure 3.7.

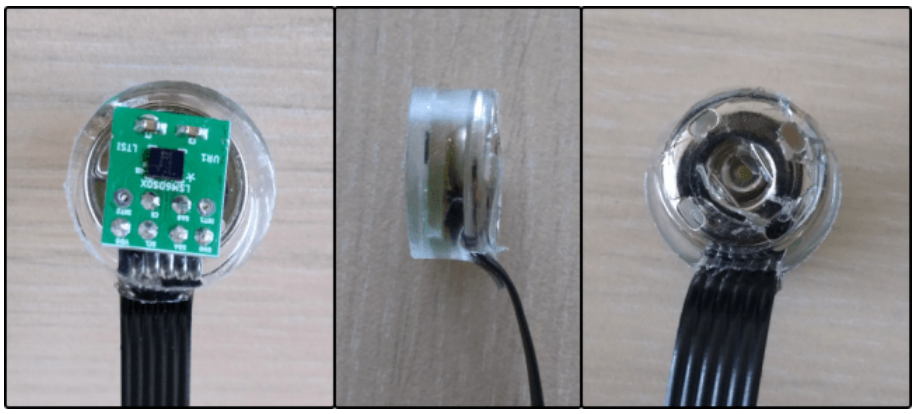

Figure 3.7 – Encapsulated LSM6DSOX custom board.

The cable that attaches directly to the board was carefully selected to provide the best sensor mobility because it is ultra-thin but still strong enough. The part of the lead comprising this type of cable is 50 cm long. At the end of the ultra-thin cable, another 1 m long cable with

double shielding for electrical noise isolation and increased strength was attached to provide more robustness to the lead. Finally, a female RS-232 connector was soldered to the end of the lead for easy connection without the risk of direct contact with the connection terminals. Figure 3.8 shows the final design of the MCG sensor lead. It is worth mentioning that the terminals corresponding to the interrupt pins were not connected because they were not needed in this application, so the lead has a total of 6 internal wires.

Figure 3.8 – Custom lead for MCG signals acquisition.

3.1.5 System housing

The main considerations when designing the system housing were the use of materials approved for use in a clinical environment, a compact design that is easy to transport and install, and a clear aesthetic appearance that reflects the professional design of the system. In addition, the possibility of implementing the system without the need to acquire the ECG and PCG signals in the future was considered, so two separate housings were designed: one for the Raspberry Pi with the HifiBerry board and a male RS-232 port for connecting the MEM sensor cable, and the other for the ECG sensor with the FT232H adapter. These housings were designed in Tinkercad® software from Autodesk® and subsequently printed on a Lulzbot® TAZ Pro 3D printer at the laboratory facilities using acrylonitrile butadiene styrene (ABS) material. Figure 3.9 shows the final system with all components connected.

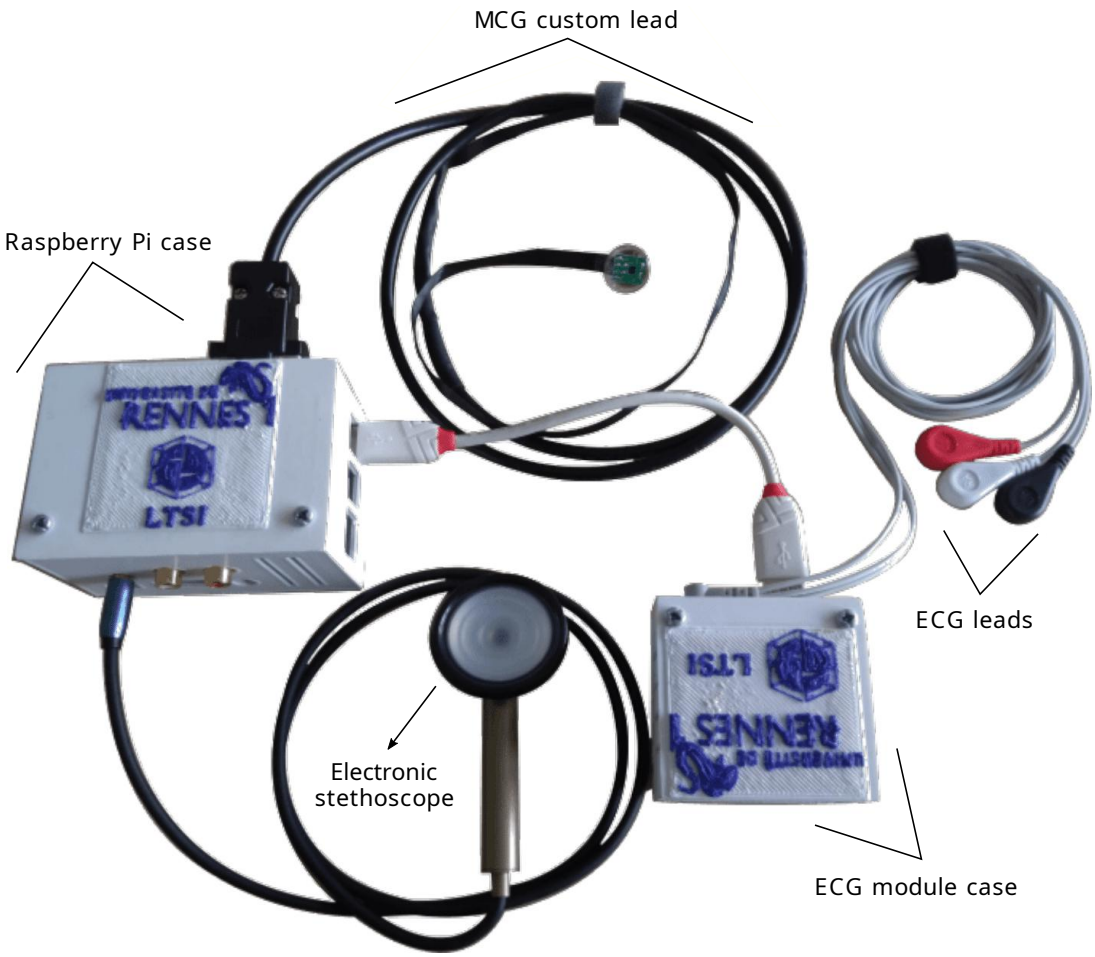

Figure 3.9 – Cardiac signal acquisition system.

3.2 Time calibration of the system

Synchronization of the sensors is a critical aspect to consider in the design of the acquisition system described above, mainly because some of the most relevant characteristics of the cardiac signals depend on their correct measurement in time, and the time error between the three sensors (MCG, ECG and PCG) must be reduced to the lowest possible value. Consequently, the procedures implemented to reduce this error in the system are described below.

3.2.1 Sampling frequency of the LSM6DSOX sensor

Although the LSM6DSOX sensor data sheet shows the different sampling frequencies that can be configured to measure SCG and GCG signals, these frequency values are not accurate if the internal clock of the Raspberry Pi board is used as a reference, which must register the data

acquisition rate of all sensors with high accuracy. For this reason, the actual sensor sampling rate must be determined by a calibration process.

The calibration procedure consists of acquiring multiple measurements from this sensor while monitoring the elapsed time with a counter controlled by the Raspberry Pi board. Considering that the data reading process uses the FIFO memory of the LSM6DSOX sensor, the number of samples read is organized in batches, so the calibration process will generate a file containing the time stamp t_i and the number of samples s_i read from each time the FIFO memory is accessed. The actual sampling rate f_{MCG} can be computed using Equation (3.1).

$$f_{MCG} = \frac{1}{B-1} \sum_{i=2}^{B} \frac{s_i}{t_i - t_{i-1}} \tag{3.1}$$

where B is the total number of acquired data batches.

This calibration procedure must be performed every time the sampling frequency of the LSM6DSOX sensor is changed or if the chip is replaced by a different one, even if it corresponds to the same model and reference because this error is relative to each chip. It is worth mentioning that it was not necessary to apply this calibration process to the ECG and PCG sensors because the ECG sensor has a much lower sampling frequency that did not present measurable error compared to the Raspberry Pi clock, and the PCG acquisition is directly controlled by the Raspberry Pi so it does not require a correction of the sampling frequency. For the experiments developed in this work, the ECG signals were acquired with a sampling frequency of 250 Hz, the PCG signals at 16 kHz and the MCG signals at 1685 Hz (frequency calculated by using Equation (3.1)).

3.2.2 Sensors synchronization

The best way to determine the difference between the acquisition times of the sensors is by generating a known and time-defined signal that all sensors can measure simultaneously. Considering the different measurement natures of the implemented sensors, it is necessary to design a system with multiple actuators that can generate a suitable signal for each sensor. The process implemented to solve this problem is described below.

Calibration circuit

The circuit designed to generate the calibration signal is quite simple and is shown in Figure 3.10. It consists of three physical phenomena generated from a single 3.3 V electrical signal controlled through one of the GPIO pins of the Raspberry Pi. Each phenomenon is associated with the nature of each of the used sensors. The first phenomenon consists of an electrical variation generated by a voltage divider between two resistors, one of 330 kΩ and the other of 33 Ω. The ECG sensor is connected to measure the voltage on the 33 Ω resistor (approximately 0.3 mV)

without risk of damaging the sensor. The second phenomenon is an audio signal generated with a small buzzer to be directly measured by the electronic stethoscope. The third phenomenon consists of the generation of vibrations that can be measured by the LSM6DSOX sensor, in this case another buzzer of higher power than the previous one mentioned was used since it generates small vibrations that can be measured due to the high sensitivity of the LSM6DSOX sensor.

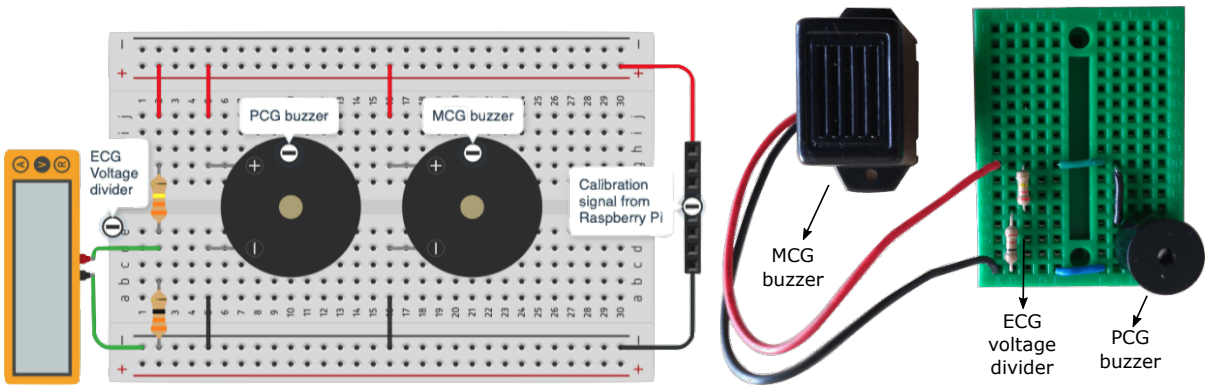

(a) Schematic design (b) Real circuit

Figure 3.10 – Calibration circuit.

Calibration signal generation

The calibration signal was configured to generate a periodically repeating pulse. The pulse duration was set to 2 ms because it was intended to be as short as possible to increase measurement accuracy and a duration of 2 ms was the minimum value detectable by the ECG sensor due to its low sampling rate. The pulse frequency was set at 2 s so that several measurements could be obtained in a single test to determine the precision of the measurement.

Calibration signal measurement

A code script was designed to display the calibration signal measurements and automatically calculate the difference in pulse detection times between the three sensors. Simple preprocessing was applied to the measured signals in order to perform automatic pulse detection. The preprocessing consisted of eliminating the offset of all the signals, then their absolute value was calculated and finally they were normalized. In the case of the LSM6DSOX sensor, the accelerometer three-axis norm was used because it was the best way to visualize the calibration pulse measured by this sensor. The pulses measured by the sensors were detected using a threshold high enough to differentiate the pulse from the sensor background noise. The final objective of this process is to obtain the synchronization error between the sensors, both in time and in number of samples according to the sampling frequency of each sensor. Figures 3.11a and 3.11b

show examples of the calibration signal measured before and after synchronizing the sensors, respectively. Figure 3.11c shows a signal in which pulses with decreasing duration are generated to verify that the pulses detected by the three sensors are coincident with each other.

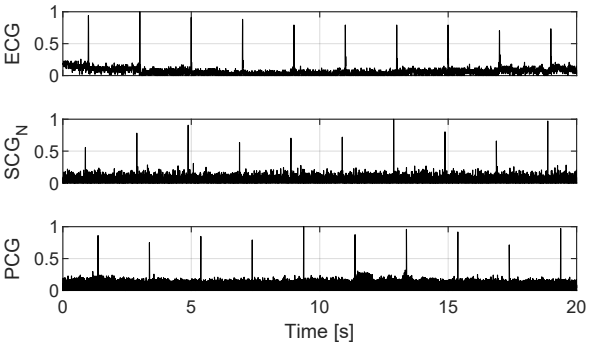

(a) Calibration signal before synchronization

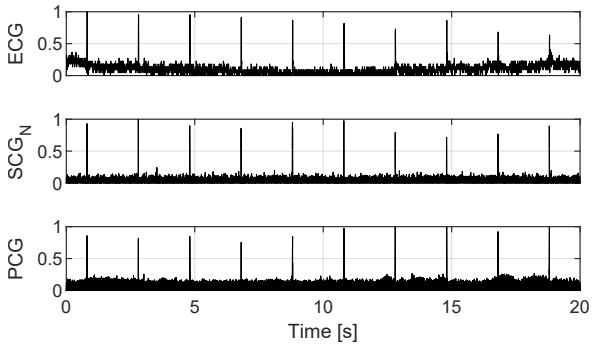

(b) Calibration signal after synchronization

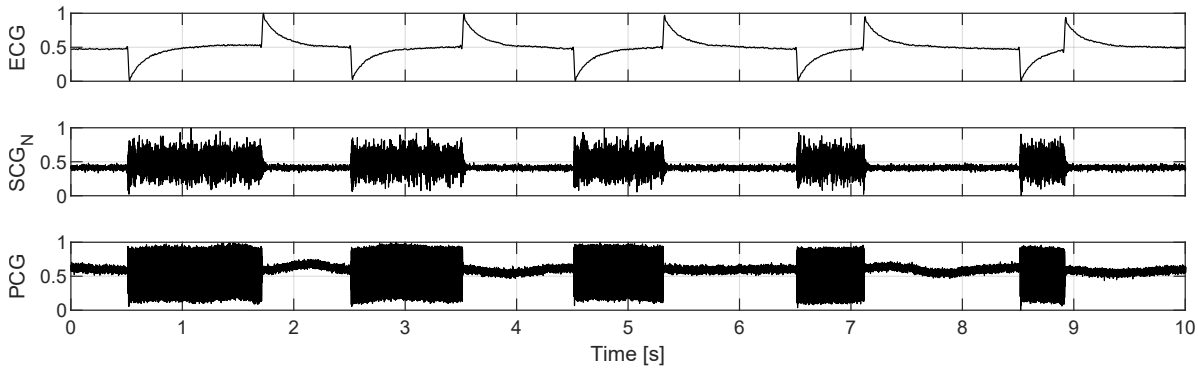

(c) Signal generated to verify correct synchronization of sensors

Figure 3.11 – Representative examples of the calibration process.

The sensor calibration process was performed with the acquisition of five recordings with a duration of 20 seconds each for a total of 50 pulses, considering that a pulse is generated every 2 seconds. The time difference between the signals was calculated taking the MCG sensor as a reference, since this is the sensor that presented the lowest latency in the measurement (which can be visualized in Figure 3.11a). Table 3.1 shows the results of the calibration process. It should be noted that only the values associated with the ECG and PCG signals are shown because the MCG sensor signal was taken as the reference. The error corresponding to the number of samples is relative to the sampling frequency of each sensor. One of the most relevant values in Table 3.1 is the standard deviation of the error measurements, because it shows the accuracy of the calibration process, finding that the standard deviation is even lower than the calibration pulse duration (2 ms) in all measurements, which validates the calculated calibration values as suitable for applying the time correction to ensure proper synchronization of the sensors for the process of measuring the cardiac signals.

Sensor	Sampling frequency	Mean error		Standard deviation
	[Hz]	[ms]	[samples]	[ms]
ECG	250	112.09	28	± 1.71
PCG	16000	839.79	13437	± 0.93

Table 3.1 – Sensor calibration results.

3.3 Experimental framework

The tests performed to evaluate the correct functioning of the cardiac signal acquisition system were divided into two groups: a first group of tests to validate the correlation between the MCG signals and the PCG, taking the latter as the gold standard reference. The second group of tests were developed for the purpose of conducting a preliminary evaluation of the hypothesis that the MLC embedded in the MEM sensor can be used to detect variations in the hemodynamic parameters of a patient in an automatic fashion. The details of these two test configurations are described below.

3.3.1 Preliminary validation with gold standard reference

This first set of tests was developed following a scheme similar to the one used to evaluate the gastric implant described in Chapter 2. The main objective of this stage of the experimental framework was to validate the acquisition of the MCG signals by comparing them with a gold standard reference, in this case provided by the PCG signal. It should be noted that the ECG signal does not require validation because it already corresponds by itself to a standard ECG configuration, which in the case of these experiments will be only used to identify the start and end of each cardiac cycle by detecting the R peaks.

Acquired data

Signals acquired for this first set of tests were measured in two healthy male volunteers from the LTSI team with an average age of 27 ± 2.8 years and an average weight of 60.5 ± 6.4 kg. One of the volunteers reported doing sport activities frequently and the other infrequently, but both reported feeling in good physical condition at the time of testing. Both volunteers were previously informed about the configuration of the tests and agreed to undergo them since they did not represent any risk to their health and did not involve invasive interventions.

The tests consisted of acquiring recordings in three different configurations: 1) baseline configuration to evaluate the correct visualization of the main cardiac components in the measured signals, 2) apnea configuration to evaluate the evolution of the cardiac signals in a minor car-

diorespiratory event, and 3) Valsalva maneuver configuration to evaluate the evolution of the cardiac signals in a more demanding cardiorespiratory event. The main objective of these configurations is to generate variations in the hemodynamic parameters of the volunteers that can be reflected in the measured signals. Three recordings were acquired with each of the configurations on two different days to increase the variability of the tests and obtain more representative results. Consequently, a total of 36 recordings were acquired in this first set of tests.

Volunteers were asked to sit on a reclining chair with an approximate tilt angle of 45° to make the volunteers comfortable during the acquisition process. The sensors were positioned as shown in Figure 3.12. On the first day of acquisition the ECG leads were fixed using standard electrodes in direct contact with the skin, the MCG sensor was fixed in the mid-sternal area between the third and fourth rib using an electrode and additionally secured using adhesive tape to simulate the effect of a subcutaneous implantation of the sensor, the PCG sensor was secured with adhesive tape in the mitral area to ensure that the pressure of the stethoscope over the chest of the volunteer did not vary during the whole acquisition process. On the second day, the same sensor configuration was used, with the only difference that the MCG sensor was fixed only with the electrode snap in order to analyze the effects on the measured signals by allowing more freedom of movement to the sensor.

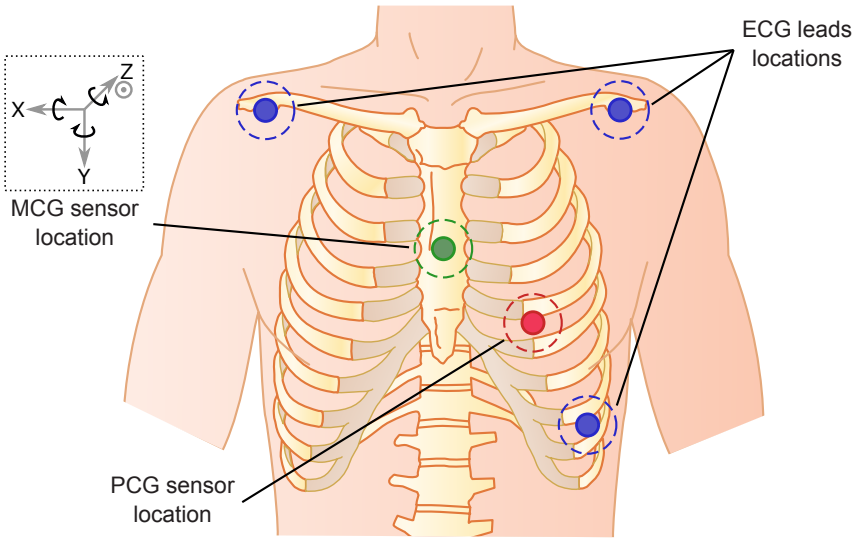

Figure 3.12 – Sensor locations used for data acquisition. Adapted from [35] with permission, copyright ©2015 Elsevier.

Each recording had a duration of 1 minute and was taken with a time gap of no less than 3 minutes between recordings. In the baseline recordings, the volunteers remained seated in a resting state with constant normal breathing. The apnea recordings started with 10 seconds of rest, followed by 20 seconds of apnea and ending with 30 seconds of recovery (on the second

day the duration of apnea was extended to 30 seconds considering that the volunteers showed a good ability to hold their breath). The Valsalva recordings consisted of an initial 10 seconds of rest, followed by a 10-second Valsalva maneuver and ending with 40 seconds of recovery.

Cardiac signal processing

The ECG signals were acquired with a sampling frequency of 250 Hz, the PCG signals at 16 kHz and the MCG signals at 1685 Hz (frequency calculated by applying the procedure described in Section 3.2.1). The filters used with these signals were much less restrictive than those used with the gastric signals described in the previous chapter, mainly because these signals have a much lower noise influence and therefore the content of a wider frequency range can be exploited. The combination of independent high-pass and low-pass third order Butterworth filters was applied to the signals by direct and reverse zero-phase digital IIR filtering. The frequency band used for ECG signals was from 1 to 100 Hz, the band for MCG signals was from 10 to 90 Hz, and finally the band for PCG signals was between 5 Hz and 1 kHz. The norm of the 3D SCG and 3D GCG were calculated before applying the filtering process and were treated as new axes representing SCG and GCG components independent of both linear and angular direction of motion.

Baseline recordings were used to analyze measurements of the main components of the CVS (S1 and S2 related to the first and second heart sounds, respectively) in both duration and amplitude. This process was performed after calculating the coherent mean of each of the signals in each of the recordings in order to apply the heart sound detection process proposed in [24] (also decribed in Section 2.3.4) and subsequently using Algorithm 1 to synchronize the heart sound detections among all the MCG signals. The apnea and Valsalva recordings were used to evaluate the correlation between the MCG and PCG signals, implementing a process similar to that described in Section 2.4.2, where the time profiles of duration and peak-to-peak value of the MCG and PCG signals were calculated using a window of 2 cardiac cycles to obtain a better resolution of the variations and thanks to the fact that these signals had a better signal-to-noise ratio than those taken with the gastric implant.

3.3.2 Preliminary machine learning core evaluation

The second set of tests was developed with the purpose of evaluating the hypothesis that the MLC embedded in the sensor used to acquire the MCG signals can be used to automatically detect variations in the hemodynamic parameters of the volunteers. These tests were developed as a first approach that seeks to test the hypothesis without the explicit need to achieve the highest performance in detection since it is proposed to use a basic configuration of the MLC without performing a post-training optimization process.

Acquired data

In this second set of tests only the signals of one of the volunteers involved in the previous tests were recorded. The tests consisted of two types of configurations that would allow assessment of the proposed hypothesis from two different perspectives: 1) apnea configuration that proposes the detection of an event that generates variations mostly of a respiratory nature, and 2) Valsalva maneuver configuration that requires the detection of both respiratory and hemodynamic variations. The arrangement of the sensors was the same as proposed in Figure 3.12, attaching the ECG leads to the electrodes, securing the electronic stethoscope with adhesive tape and fastening the MCG sensor only with the electrode snap.

The acquisition process consisted of taking three training recordings and three test recordings for each of the configurations, taking a total of 12 recordings. Each recording had a duration of one minute with a time gap between recordings of at least 3 minutes. Each of the recordings was divided into samples of 1 second duration, with the purpose of capturing at least one complete cardiac cycle in each sample. The apnea recordings were divided into 3 stages (classes): **Baseline** with 30 seconds duration, **Apnea** with 20 seconds duration and **Post-apnea** (which corresponds to the time immediately after the apnea stage) with 10 seconds duration, and similarly the Valsalva recordings were divided into 3 stages (classes): **Baseline** with 40 seconds duration, **Valsalva** with 10 seconds duration and **Post-Valsalva** (which corresponds to the time immediately after the Valsalva stage) with 10 seconds duration. This process resulted in a distribution of the samples as shown in Table 3.2.

Configuration	**Class**	**Number of samples**		
		Train	**Test**	**Total**
Apnea	Baseline	90	90	180
	Apnea	60	60	120
	Post-apnea	30	30	60
Valsalva	Baseline	120	120	240
	Valsalva	30	30	60
	Post-valsalva	30	30	60
Total		360	360	720

Table 3.2 – Distributions of samples recorded for MLC evaluation.

The classes selected for each of the configurations were based on the fact that the seconds immediately after the cardiorespiratory event (apnea or Valsalva) present some significant variations in the S1 and S2 waveforms, so it was proposed to differentiate these variations from the baseline stage in order to perform a more complete evaluation of the different hemodynamic variations that can generate these cardiorespiratory events.

MLC configuration

The MLC in the LSM6DSOX sensor is specially designed to be used in mobile devices such as smartphones or smartwatches, so it has features suitable for this type of devices and applications related to them, such as recognition of activities like walking, running, riding a bike, sitting or driving a vehicle. This may represent a disadvantage for the present project because such features are not ideally suited to those required for the analysis and processing of CVS. However, adjustments can be made to the configuration that allow for a basic and functional analysis of these types of signals that is supposed to be sufficient for the proposed task. Figure 3.13 shows a representative diagram of the different tools that can be configured in the MLC of the LSM6DSOX sensor for processing the acquired signals up to defining a specific machine learning application.

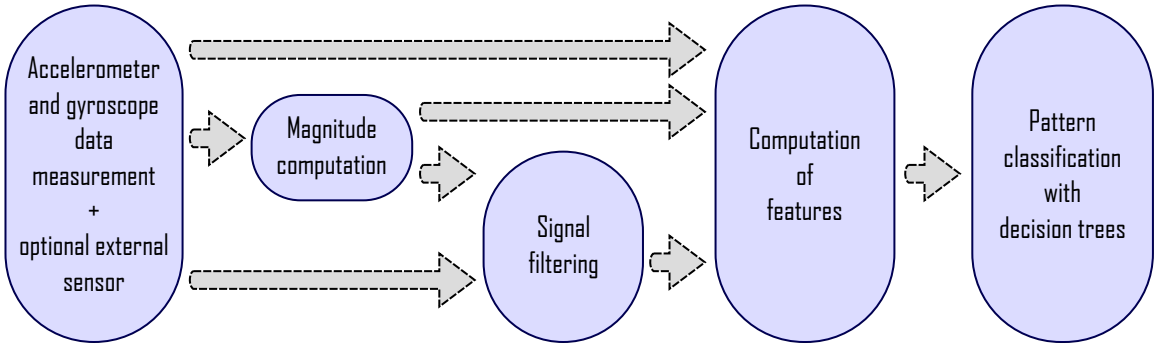

Figure 3.13 – diagram of the data acquisition and processing pipeline in the MLC.

The MLC has a maximum sampling rate of 104 Hz, so the MCG sensor sampling rate was set to 105.31 Hz (frequency calculated using the process described in Section 3.2.1) while the ECG and PCG sensor sampling rates were kept the same at 250 Hz and 16 kHz, respectively. One of the most useful features of the MLC is the possibility of configuring filters that are applied to the measured signals prior to the feature generation process. The filters can be configured based on a second order IIR filter with the transfer function shown in Equation (3.2) to generate the output shown in Equation (3.3). The parameters b_1, b_2, b_3, a_2, a_3 and $Gain$ are configurable to obtain the desired low pass, high pass, and band pass filters.

$$H(z) = \frac{b_1 + b_2 z^{-1} + b_3 z^{-2}}{1 + a_2 z^{-1} + a_3 z^{-2}} \tag{3.2}$$

$$y(z) = (H(z) \cdot x(z)) \cdot Gain \tag{3.3}$$

where $x(z)$ represents the input signal and $y(z)$ the output signal.

Three different filters were configured to represent distinct components of the cardiorespiratory signals. A first low-pass filter with a cutoff frequency of 1 Hz to extract only the component corresponding to respiration, a second high-pass filter with a cutoff frequency of 5 Hz to retain only the components associated with cardiac vibrations, and a third band-pass filter between 20 and 40 Hz to emphasize the components of the CVS that carry the highest energy of this type of signal [24, 126]. Figure 3.14 shows the frequency response of these filters and their corresponding parameters are presented in Table 3.3.

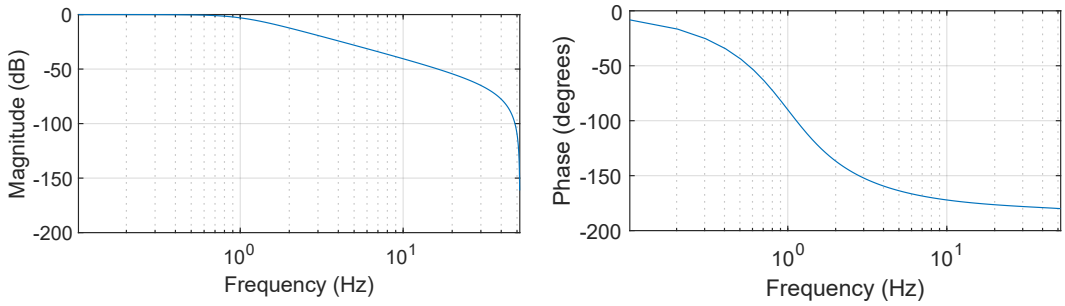

(a) Magnitude and phase responses of Filter 1

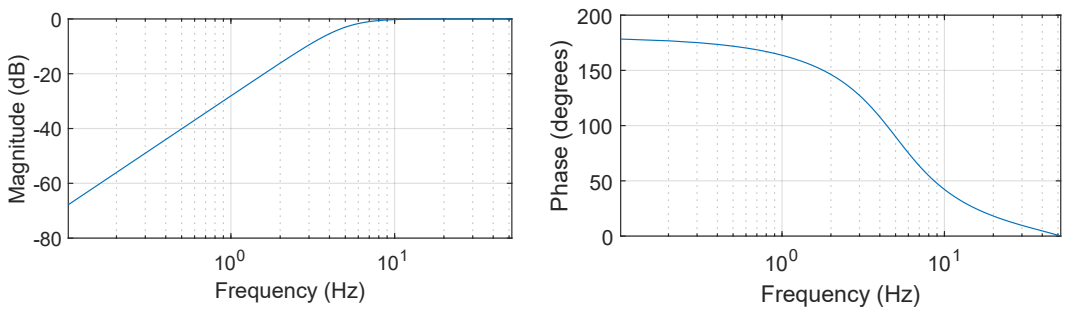

(b) Magnitude and phase responses of Filter 2

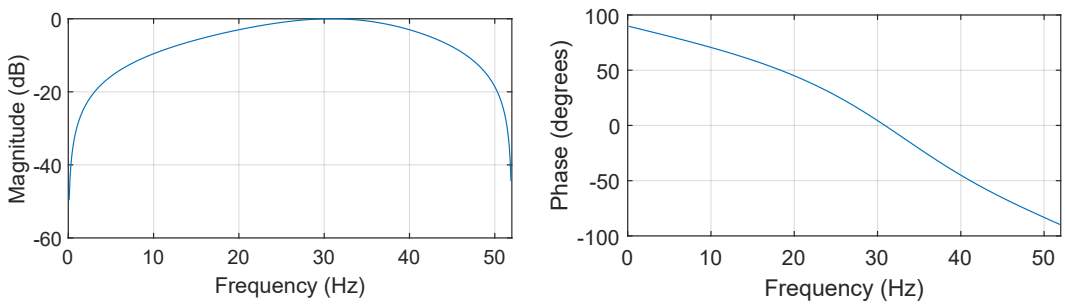

(c) Magnitude and phase responses of Filter 3

Figure 3.14 – Frequency response of the filters configured in the MLC.

The MLC offers the possibility to compute multiple types of features on the raw SCG and GCG signals, as well as to compute the same features on the norm and squared norm of both types of signals and also on the output of any of the filters applied to all the aforementioned

ID	Filter type	Coefficients					
		b_1	b_2	b_3	a_2	a_3	Gain
Filter 1	Low-pass	0.0009	0.0017	0.0009	-1.9146	0.9181	1.0000
Filter 2	High-pass	0.8075	-1.6150	0.8075	-1.5776	0.6524	1.0000
Filter 3	Band-pass	1.0000	0.0000	1.0000	0.3441	0.1833	0.4084

Table 3.3 – MLC filter parameters.

signals. The features are mainly based on statistical measures applied on each of the training samples. These features are mean, variance, energy, peak-to-peak, minimum and maximum values, and counters with adjustable threshold of zero crossing, positive zero crossing, negative zero crossing, peak detector, positive peak detector and negative peak detector.

Considering that the LSM6DSOX sensor allows to compute a maximum of 31 features, only the mean, variance, energy and peak-to-peak value measurements were computed over the SCG and GCG norm and the outputs of the three filters described in Table 3.3 applied to the SCG and GCG norm, thus obtaining 8 features for each measurement. The energy of the output of the third filter applied to the GCG norm was omitted in order to meet the limit of 31 features. It was chosen to calculate the features using only the SCG and GCG norm seeking that the detections were not affected by changes in volunteer position during the recording process or changes in the position of the sensor, which was fastened using only the electrode snap.

Decision tree creation and detection assessment

The data acquisition process was developed as follows:

1. Install the sensors on the chest of the volunteer while he was sitting comfortably in a reclining chair with an approximate tilt angle of 45°.
2. Take the three training recordings for the apnea configuration.
3. Use the training data to train a decision tree using the software tools provided by the LSM6DSOX sensor manufacturer [160].
4. Load the decision tree configuration into the sensor to take the three test recordings, reading and saving the MLC detections in real time during the recording process.
5. Repeat steps 2 through 4 for the valsalva configuration.
6. Evaluate the obtained detection results by applying different evaluation measures.

Considering that the collected data present a large imbalance between classes, especially for the Valsalva configuration, different evaluation measures were used that could reflect the real performance of the detection avoiding the bias generated by the imbalance of the classes. The

evaluation measures used are sensitivity (SEN), specificity (SPC), precision (PRE), geometric mean (G-mean), F1 score and accuracy (ACC), which were calculated using Equations (3.4) to (3.9), respectively. All measures are calculated based on the assignment of true-positive (TP), true-negative (TN), false-positive (FP) and false-negative (FN) samples that make up the confusion matrix.

$$SEN = \frac{TP}{TP + FN} \tag{3.4}$$

$$SPC = \frac{TN}{TN + FP} \tag{3.5}$$

$$PRE = \frac{TP}{TP + FP} \tag{3.6}$$

$$\textit{G-mean} = \sqrt{SEN \cdot SPC} \tag{3.7}$$

$$\textit{F1 score} = 2 \cdot \frac{PRE \cdot SEN}{PRE + SEN} \tag{3.8}$$

$$ACC = \frac{TP + TN}{TP + TN + FP + FN} \tag{3.9}$$

3.4 Results

3.4.1 Preliminary validation of MCG against a gold standard reference

Analysis of baseline recordings

Figures 3.15 and 3.16 show representative examples of the coherent mean of each of the signals measured during the first day of acquisition on the first and second volunteer, respectively. Similar figures associated with respresentative examples taken during the second day of acquisition can also be found in Appendix A. Also included in these figures are the final results of the detection process of S1 and S2, differentiating the detection applied on the MCG and PCG signals separately to have a better visualization of the comparison of the results of this detection process on both types of signals. It should be noted that the detection of the first and second heart sounds obtained on the PCG was projected onto the ECG to analyze the relationship between the heart sounds and the main electrophysiological events of the heart. The PCG detection was chosen to be projected because this signal is taken as the gold standard reference.

Several interesting details can be observed in these figures obtained from the baseline signals.

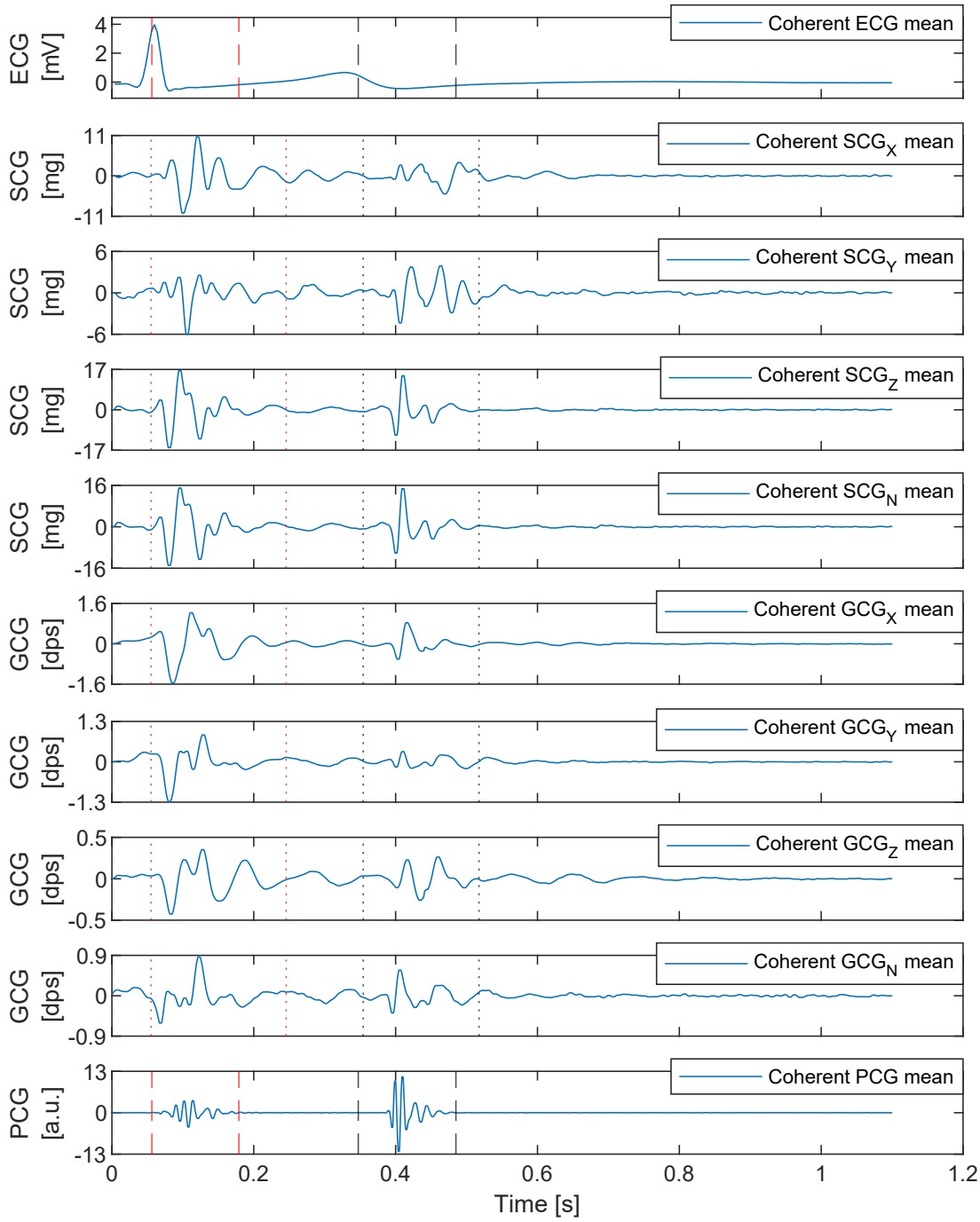

Figure 3.15 – Representative example of signals taken in volunteer 1 on the first day. The vertical lines represent the detection times of the first and second heart sounds in red and black, respectively. The dotted lines represent detection using the MCG, while the dashed lines represent detection using the PCG. Note also that the detection of heart sounds using the PCG is projected onto the ECG for better analysis of the relationship between electrophysiological events and heart sounds.

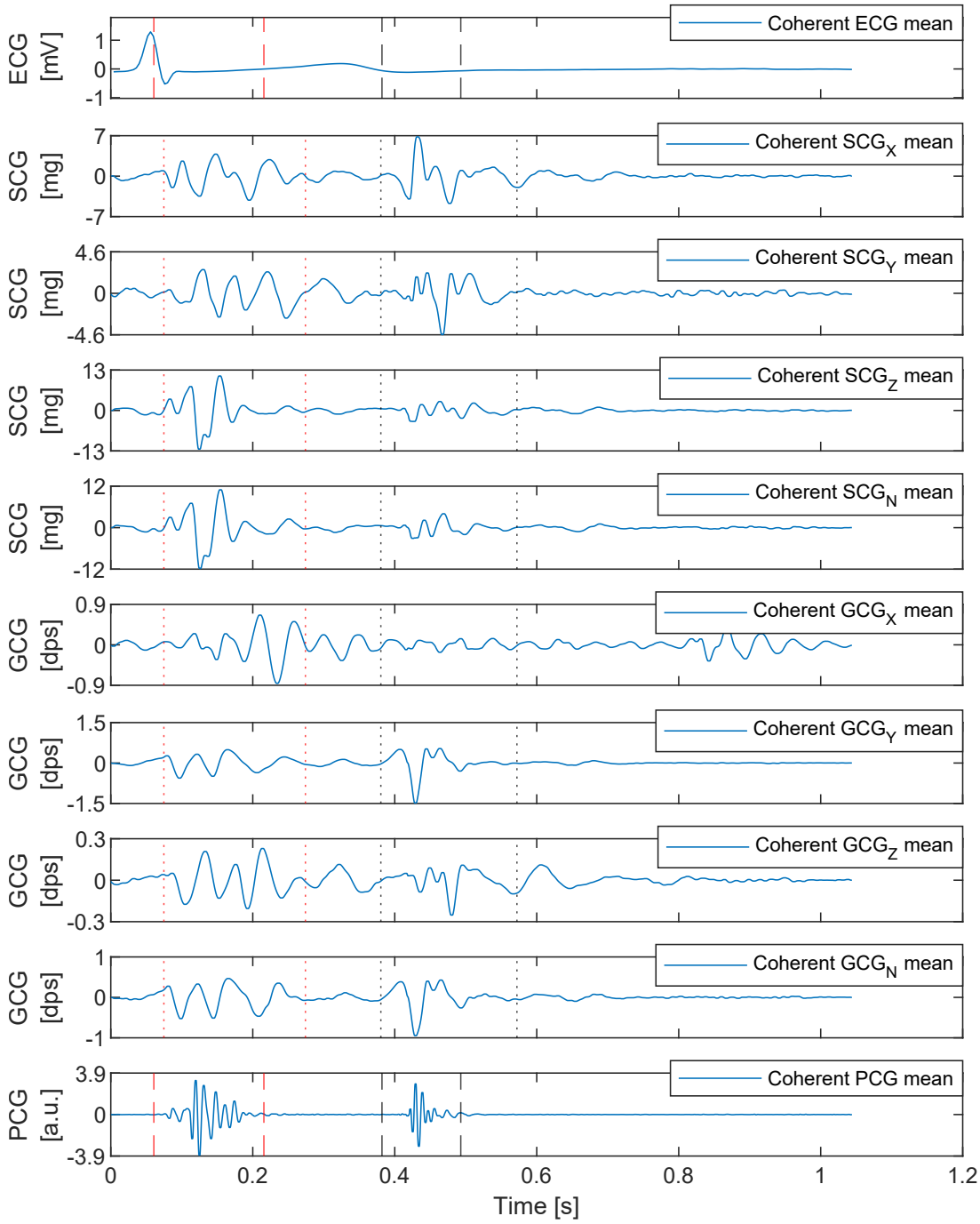

Figure 3.16 – Representative example of signals taken in volunteer 2 on the first day. The vertical lines represent the detection times of the first and second heart sounds in red and black, respectively. The dotted lines represent detection using the MCG, while the dashed lines represent detection using the PCG. Note also that the detection of heart sounds using the PCG is projected onto the ECG for better analysis of the relationship between electrophysiological events and heart sounds.

A first detail is the significant difference observed in the waveforms of the signals corresponding to the first volunteer compared to those of the second volunteer, which evidences the high inter-subject variability associated with CVS that has been widely mentioned in the literature [11, 27, 108], pointing out such variability as one of the main reasons to develop devices and algorithms that can be configured in a personalized way for each patient. Another interesting detail is that the duration of S1 and S2 tends to be longer in the MCG signals than in the PCG, which can be mainly explained by the difference in sensitivity between these sensors (evidenced by the signal to noise ratio observable in both types of signals), in addition to the fact that the measured signals come from different natures in which the CVS manage to capture a greater amplitude in low frequency components that can be overshadowed by the higher frequency components in the PCG. A final detail is the great similarity between the waveforms of the SCG and GCG signals, which has also been highlighted before in the literature and is mainly explained by the fact that both types of signals are generated from the same physical nature measured from different kinetic variations [108].

Table 3.4 shows the signal-to-noise ratio and contrast measurements of the first and second heart sounds in the baseline signals for both volunteers during the two days of data acquisition. These measurements were calculated in the same way as was done with the signals captured with the gastric implant described in the previous chapter, as specified in Section 2.3.5. This table shows how the ECG measurements remain constant for both days of acquisition while the PCG shows some significant intra-subject variations that can be explained by small changes in the position and pressure of the stethoscope on the chest of the volunteer between both days of acquisition, because these small changes (very difficult to control) can significantly affect the amplitude of the sounds measured in the PCG. Nevertheless, the measurements of both sensors in all cases present sufficiently high values that reflect a good quality of the measurements.

One of the most important results presented in Table 3.4 is the fact that both the signal-to-noise ratio and the contrast of S1 and S2 are significantly enhanced between the first and second day of acquisition for all MCG signals in volunteer 1 and most MCG signals in volunteer 2. This observation implies that the use of the adhesive tape to simulate a subcutaneous implant generates a significant reduction in the sensitivity of the MCG sensor to measure CVS, so it is recommended to use this sensor secured only with the electrode snap in order to avoid limiting its mobility and thus improving its sensitivity, evidently only for external measurement use cases and in resting conditions such as those used in the experiments proposed in this work. All the MCG signals present a better signal-to-noise ratio and contrast than those measured with the gastric implant (whose results are shown in Table 2.6) and consequently in accordance with the literature [149, 150, 126], which is to be expected considering that the acquisition conditions in this case are much more controlled and the sensor location is less exposed to sources of noise and artifacts.

				Volunteer 1		Volunteer 2	
				Recordings of day 1	Recordings of day 2	Recordings of day 1	Recordings of day 2
Signal-to-Noise Ratio [dB]	ECG			29.97±0.54	30.51±0.55	28.50±1.91	29.42±1.03
	First heart sound	SCG		24.11±2.15	29.01±2.91	21.77±2.33	21.69±1.77
		GCG		18.26±2.99	23.43±3.03	15.83±2.75	19.96±3.36
		PCG		33.83±3.98	35.20±3.09	32.11±3.28	36.41±5.11
	Second heart sound	SCG		24.33±1.81	27.04±2.88	14.25±2.65	20.84±1.77
		GCG		14.46±2.42	18.42±2.92	18.90±2.91	20.50±3.46
		PCG		38.88±2.59	34.87±3.27	30.24±2.89	28.14±5.13
Heart sounds contrast	First heart sound	SCG		7.18±1.16	10.36±2.30	5.04±0.96	4.71±0.64
		GCG		3.68±0.79	6.34±1.83	3.49±0.70	4.48±1.00
		PCG		29.49±11.36	35.02±12.41	15.38±6.90	24.25±12.94
	Second heart sound	SCG		5.58±0.76	7.17±1.71	2.27±0.51	3.70±0.60
		GCG		2.50±0.45	3.20±0.98	3.56±0.85	3.96±0.96
		PCG		40.39±11.22	29.04±9.92	11.07±4.79	11.11±5.89

Table 3.4 – Quality measurements of signals acquired as baseline. Note that for SCG and GCG signals only the measurements taken on the norm (N-axis) between the 3 axes (X, Y and Z) are shown.

Table 3.5 shows the results of the time analysis of the detection of S1 and S2. The duration of systole and diastole were calculated using both MCG and PCG signals for comparison, in addition to calculating the difference between each of the start and end times of S1 and S2 (first and second heart sounds in the PCG, respectively) measured in the MCG and PCG. The results show that the detection of S1 and S2 start times ($t1$ and $t3$, respectively) are closely similar between the MCG and PCG, which is also evidenced by the small margin of error between systole and diastole duration calculations. The major difference is seen in the end times of both S1 and S2, which as mentioned earlier, is an understandable error based on the sensitivity and source nature of the physical phenomena measured by both sensors.

Analysis of apnea and Valsalva recordings

Figures 3.17 and 3.18 show representative examples of the duration time-profiles of S1 and S2 for recordings taken on volunteer 1 with the apnea and Valsalva configurations, respectively. Similar figures of representative examples of the recordings taken on volunteer 2 can be found in Appendix B. These figures allow to observe how both apnea and Valsalva maneuver manage to generate significant variations in the duration of S1 and S2 for both volunteers, which validates

		Recording	Heart rate [BPM]	Systole [ms]		Diastole [ms]		Heart sounds timing difference between MCG and PCG [ms]			
				MCG	PCG	MCG	PCG	$t1$	$t2$	$t3$	$t4$
Volunteer 1	Day 1	1	55	299.11	291.00	800.89	809.00	-1.14	66.70	6.97	32.51
		2	55	300.30	292.67	791.69	799.33	-0.40	78.34	7.23	16.34
		3	55	298.52	296.33	793.47	795.67	-0.07	53.72	2.12	8.04
	Day 2	1	49	324.63	321.33	907.42	910.67	0.05	41.87	3.35	-6.09
		2	52	312.76	309.00	833.23	837.00	0.23	39.82	3.99	14.05
		3	50	313.95	307.67	881.90	888.33	0.27	53.32	6.55	7.61
Volunteer 2	Day 1	1	57	305.64	321.33	738.28	722.67	14.11	58.52	-1.58	79.11
		2	60	310.98	316.00	680.71	676.00	13.22	52.73	8.20	56.08
		3	64	309.20	304.33	624.93	629.67	-2.73	47.08	2.14	36.30
	Day 2	1	51	337.09	343.67	830.86	824.33	-16.43	50.67	-23.00	53.46
		2	53	343.03	352.33	785.16	775.67	-5.09	50.47	-14.40	85.26
		3	50	345.40	366.33	852.52	831.67	-3.56	56.74	-24.50	55.23

Table 3.5 – Timing measurements of signals acquired as baseline.

the proposal to use these strategies to indirectly analyze the measurement of the hemodynamic parameters, which, as clearly established in Section 1.3, are correlated with the main components of the CVS and heart sounds. Such variations are more evident in the signals measured on volunteer 2, which largely depends on the effectiveness with which the volunteers were able to perform the proposed tests and the inter-subject variability of the cardiovascular response to this type of stimuli.

Although there is a considerable difference between the end times of the MCG components (S1 and S2) and the main heart sounds, as evidenced in Table 3.5, it is possible to observe that the total duration of these components manage to keep a close relationship with the total duration of the heart sounds, showing patterns of increase and decrease in the duration of the heart sounds that are simultaneously reflected between the MCG and the PCG. However, it is also evident that in some time instants the MCG and PCG duration time profiles do not seem to have a good correlation, which indicates that there is a high complexity regarding the accurate detection of the start and end times of S1 and S2, becoming a problem that needs to be further worked on and for this purpose strategies that take advantage of the use of the data multimodality can be further developed to improve the results, as proposed with the use of Algorithm 1.

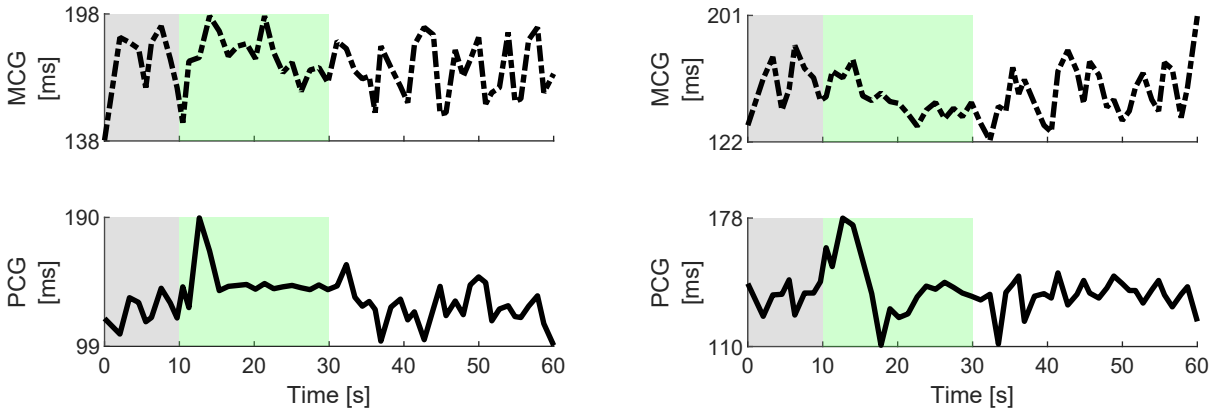

(a) Time-profile of S1 duration (b) Time-profile of S2 duration

Figure 3.17 – Representative example of evolution over time of heart sounds duration on volunteer 1 during apnea. Dash-dotted lines correspond to the MCG signals and solid lines correspond to the reference PCG signals. The gray, green and white backgrounds correspond to the baseline, apnea and recovery stages, respectively.

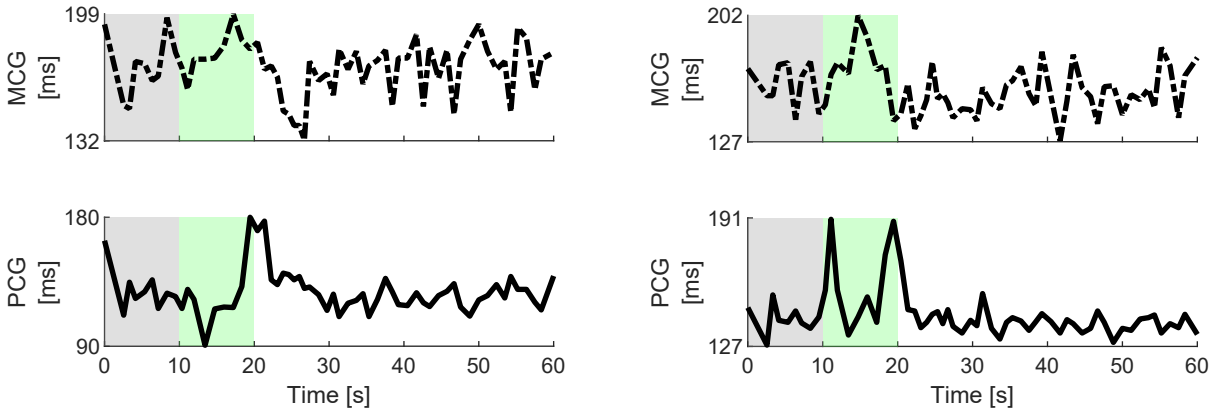

(a) Time-profile of S1 duration (b) Time-profile of S2 duration

Figure 3.18 – Representative example of evolution over time of heart sounds duration on volunteer 1 during Valsalva. Dash-dotted lines correspond to the MCG signals and solid lines correspond to the reference PCG signals. The gray, green and white backgrounds correspond to the baseline, Valsalva and recovery stages, respectively.

Figures 3.19 and 3.20 show representative examples of the peak-to-peak time-profiles of S1 and S2 for recordings taken on volunteer 1 with the apnea and Valsalva configurations, respectively. Similar figures of representative examples of recordings taken on volunteer 2 can also be found in Appendix B. These figures show more clearly the evident similarity between the amplitude of the two main heart sounds and the S1 and S2 components of all MCG signals. These patterns of similarity between both types of signals suggest the presence of a high correlation between the signals of the MCG and the PCG, which is the main claim that seeks to be tested by performing these tests. Additionally, both the peak-to-peak value time profiles of the signals measured during apnea and Valsalva maneuver are shown to have a frequency component ap-

parently associated with respiration, which is highlighted in both the MCG and PCG. This may be caused by the fact that the sensitivity of the sensors may be slightly affected depending on the amount of air contained in the lungs, which generates a variation of the distance between the sensors and the heart through the expansion and contraction of the rib cage.

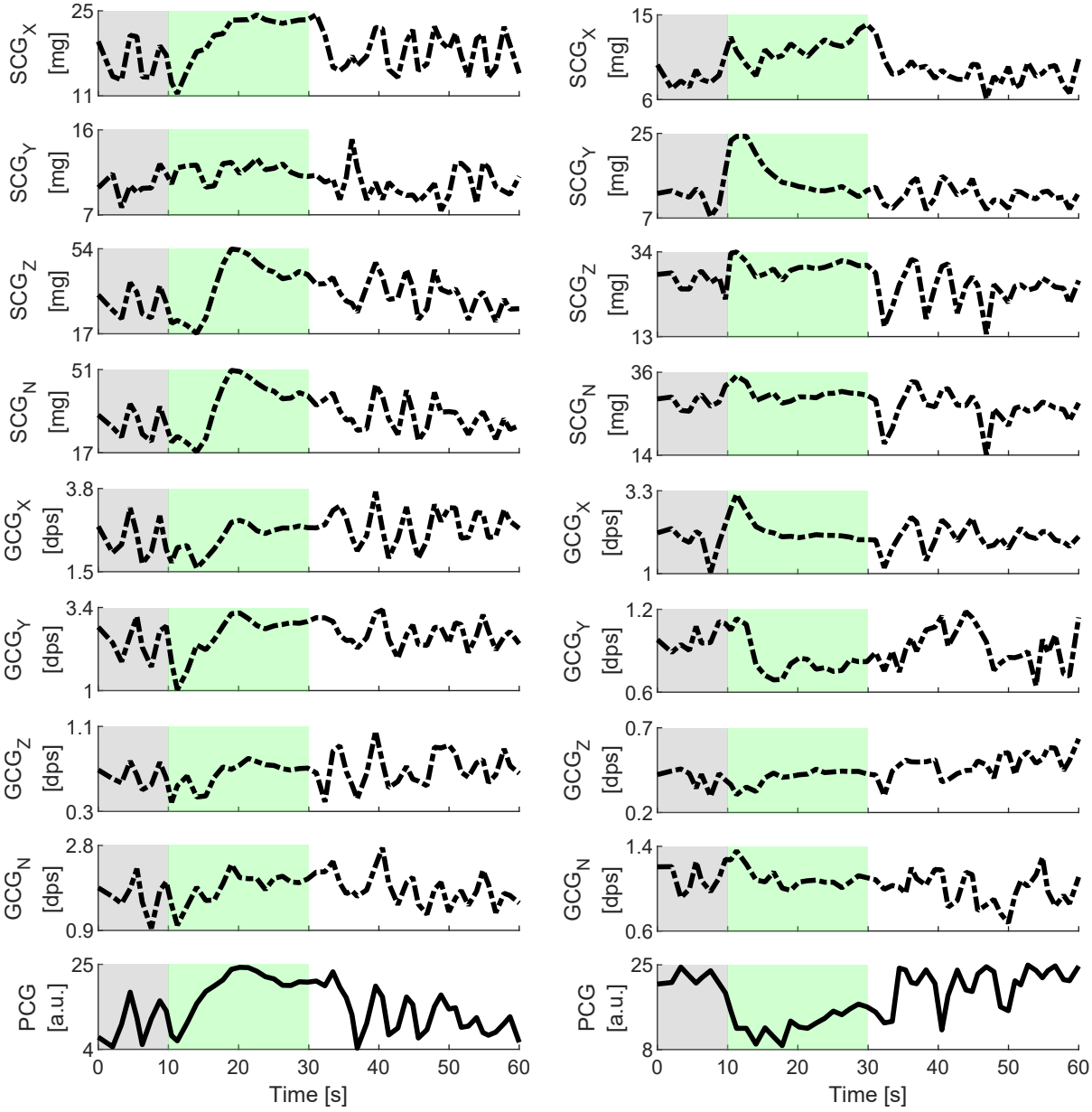

(a) Time-profile of S1 peak-to-peak value

(b) Time-profile of S2 peak-to-peak value

Figure 3.19 – Representative example of evolution over time of heart sounds peak-to-peak value measured on volunteer 1 during apnea. Dash-dotted lines correspond to the MCG signals and solid lines correspond to the reference PCG signals. The gray, green and white backgrounds correspond to the baseline, apnea and recovery stages, respectively.

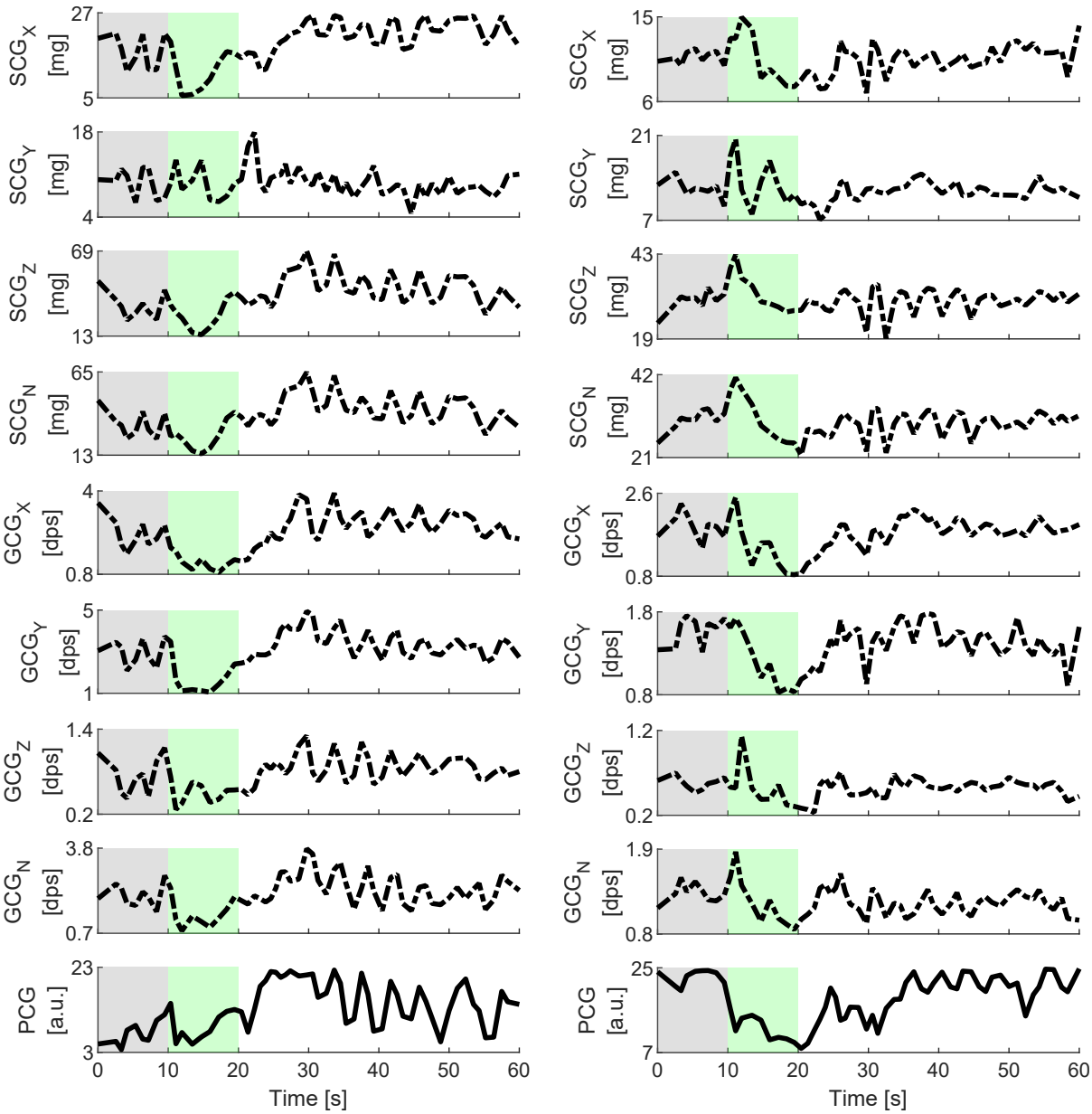

(a) Time-profile of S1 peak-to-peak value

(b) Time-profile of S2 peak-to-peak value

Figure 3.20 – Representative example of evolution over time of heart sounds peak-to-peak value measured on volunteer 1 during Valsalva. Dash-dotted lines correspond to the MCG signals and solid lines correspond to the reference PCG signals. The gray, green and white backgrounds correspond to the baseline, Valsalva and recovery stages, respectively.

It is worth mentioning that the figures associated with the time-profiles of both duration and peak-to-peak value were developed with the purpose of proposing a tool that allows a qualitative analysis of the evolution of S1 and S2 over time during each of the tests, allowing a quick and effective analysis in a simpler way than plotting the measured signals with all their

content, which finally could be interpreted as a high noise content that obscures the true relevant characteristics of the target signals.

Tables 3.6 and 3.7 show quantitative results of the comparison between MCG and PCG time-profiles for the first and second heart sounds, respectively. These tables show that both the duration and peak-to-peak time-profiles of the MCG have a high correlation with those of the PCG, which is consistent with the results also obtained from measurements made with the gastric implant described in the previous chapter, whose results are shown in Table 2.3.

Day	**Time-profile**			**Correlation between MCG and PCG for the first heart sound [%]**			
				Volunteer 1		**Volunteer 2**	
				Apnea	**Valsalva**	**Apnea**	**Valsalva**
1	**Duration**			99.25±0.04	99.08±0.24	99.17±0.38	97.79±0.69
	Peak-to-peak value	**SCG**	**X**	96.23±0.17	92.61±1.97	94.16±0.39	94.94±1.76
			Y	91.63±0.97	90.71±1.63	89.07±3.95	89.21±5.18
			Z	96.35±0.69	94.19±1.95	91.58±3.08	94.65±1.13
			N	96.25±0.80	94.21±1.84	92.97±2.52	94.89±1.08
		GCG	**X**	93.78±0.73	91.96±1.05	88.36±2.96	84.70±5.66
			Y	94.94±0.13	93.16±2.27	91.68±1.31	95.32±1.13
			Z	93.34±1.23	92.66±2.57	89.96±4.42	84.55±8.16
			N	94.20±1.15	92.78±2.36	91.66±1.49	93.53±3.07
2	**Duration**			99.28±0.12	98.37±0.28	98.63±0.34	98.39±0.30
	Peak-to-peak value	**SCG**	**X**	87.87±18.54	95.12±0.90	95.18±2.20	92.85±2.10
			Y	89.77±13.31	90.60±4.22	88.95±11.40	92.56±1.17
			Z	98.55±0.73	96.45±0.73	91.36±9.29	91.45±1.14
			N	98.74±0.52	96.12±0.84	90.55±10.81	92.90±0.90
		GCG	**X**	85.03±22.70	84.97±5.79	81.31±11.40	91.70±1.21
			Y	89.30±15.68	96.78±0.84	92.70±4.49	90.53±2.71
			Z	92.74±5.49	88.31±4.90	87.25±14.62	85.81±8.20
			N	86.12±19.40	86.87±9.66	92.29±5.57	91.84±2.82

Table 3.6 – Correlation between MCG and PCG time-profiles for the first heart sound.

An important detail that should be highlighted in these results is the fact that the correlation measurements of both the first and second heart sounds show higher values in most cases for

Day	Time-profile			Correlation between MCG and PCG for the second heart sound [%]			
				Volunteer 1		Volunteer 2	
				Apnea	Valsalva	Apnea	Valsalva
1	Duration			99.40±0.22	99.33±0.12	98.99±0.40	96.04±0.36
	Peak-to-peak value	SCG	X	93.87±3.15	95.91±0.57	94.57±1.90	92.89±2.54
			Y	91.96±3.85	93.34±2.99	96.51±1.71	89.74±2.75
			Z	95.64±2.32	96.57±1.11	96.05±1.22	90.47±1.79
			N	96.16±1.91	96.92±0.94	97.23±2.16	91.29±1.17
		GCG	X	95.01±2.13	91.35±9.22	94.08±3.49	79.85±9.14
			Y	96.56±1.71	95.07±3.09	94.89±2.08	89.36±3.78
			Z	98.43±1.04	82.91±17.46	93.63±0.55	74.10±15.51
			N	95.74±2.29	90.13±6.86	93.27±2.66	90.10±1.79
2	Duration			98.66±1.32	98.93±0.37	98.40±0.31	95.78±1.57
	Peak-to-peak value	SCG	X	83.82±9.61	89.20±5.21	90.56±3.71	92.63±2.41
			Y	88.16±7.65	87.36±9.79	92.70±4.19	93.28±2.31
			Z	93.52±2.10	93.70±1.49	91.77±2.92	92.90±0.99
			N	93.76±1.88	94.44±1.59	92.90±3.45	92.38±1.11
		GCG	X	77.09±17.02	77.28±7.71	88.64±10.38	88.65±7.37
			Y	87.52±12.35	88.27±5.70	89.03±4.09	92.30±1.90
			Z	68.82±13.48	77.79±4.48	91.09±7.83	78.71±9.27
			N	88.79±8.12	84.54±8.13	89.17±4.74	89.88±0.96

Table 3.7 – Correlation between MCG and PCG time-profiles for the second heart sound.

measurements made on the first day of acquisition than those made on the second day. This is true for both volunteers and may be due to the fact that there is an increase in the background noise of the signals during the performance of the apnea and Valsalva maneuver due to movements such as trembling, changes in the inclination of the body of the volunteer and increase in the amplitude and frequency of respiration at the end of the maneuvers to catch the breath. The reason why this increase in noise has a greater influence on the measurements of the second day is because the MCG sensor has greater freedom for movement due to the removal of the adhesive tape used during the first day, which increases the sensitivity of the sensor for measuring cardiac vibrations, but unfortunately also for measuring noise.

Some strategies that will allow to eliminate the problem of increased background noise in future experiments will be to perform measurements in patients undergoing changes or adjustment of implantable devices such as pacemakers, so that no subject movement or effort is required to generate variations in hemodynamic parameters, or there is also the possibility of performing measurements during animal experimentation, generating hemodynamic changes through the use of drugs such as dobutamine and esmolol.

3.4.2 Automatic detection of apnea and Valsalva using the MLC

Construction of decision trees

After verifying the correct synchronization of the sensors, the training data was acquired to build the decision trees using the software tools provided by the manufacturer of the LSM6DSOX sensor. The decision trees have the special characteristic of functioning as feature selectors while being trained to perform the classification task. Table 3.8 shows the list of all the features that were calculated from the training samples and the number of times the trained decision trees for the apnea and Valsalva configurations selected each feature. Additionally, Figures 3.21 and 3.22 show in detail the structure and threshold values of the decision trees constructed for apnea and Valsalva detection, respectively.

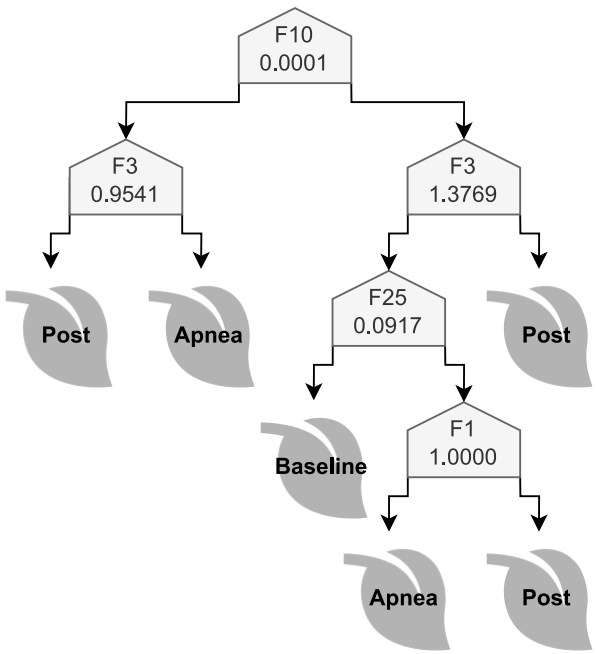

Figure 3.21 – Decision tree generated for the evaluation of MLC during apnea. Branches and leaves growing to the right correspond to values above the threshold established for each feature, while branches and leaves growing to the left represent values below or equal to the threshold.

Feature ID	Measure	Source (norm)	Filter	Number of times selected by decision tree	
				Apnea	Valsalva
F1	Mean	SCG	Unfiltered	1	0
F2	Mean	GCG	Unfiltered	0	1
F3	Mean	SCG	Filter 1	2	3
F4	Mean	GCG	Filter 1	0	1
F5	Mean	SCG	Filter 2	0	1
F6	Mean	GCG	Filter 2	0	0
F7	Mean	SCG	Filter 3	0	1
F8	Mean	GCG	Filter 3	0	0
F9	Variance	SCG	Unfiltered	0	0
F10	Variance	GCG	Unfiltered	1	0
F11	Variance	SCG	Filter 1	0	0
F12	Variance	GCG	Filter 1	0	1
F13	Variance	SCG	Filter 2	0	1
F14	Variance	GCG	Filter 2	0	0
F15	Variance	SCG	Filter 3	0	0
F16	Variance	GCG	Filter 3	0	1
F17	Energy	SCG	Unfiltered	0	1
F18	Energy	GCG	Unfiltered	0	0
F19	Energy	SCG	Filter 1	0	0
F20	Energy	GCG	Filter 1	0	0
F21	Energy	SCG	Filter 2	0	0
F22	Energy	GCG	Filter 2	0	0
F23	Energy	SCG	Filter 3	0	0
F24	Peak to peak	SCG	Unfiltered	0	0
F25	Peak to peak	GCG	Unfiltered	1	1
F26	Peak to peak	SCG	Filter 1	0	1
F27	Peak to peak	GCG	Filter 1	0	0
F28	Peak to peak	SCG	Filter 2	0	1
F29	Peak to peak	GCG	Filter 2	0	2
F30	Peak to peak	SCG	Filter 3	0	0
F31	Peak to peak	GCG	Filter 3	0	0

Table 3.8 – Features computed for the classification of cardiorespiratory events. All features were computed on the SCG and GCG norm. Note that the number of times a feature was selected by a decision tree can be considered as an indicator of relevance of that feature.

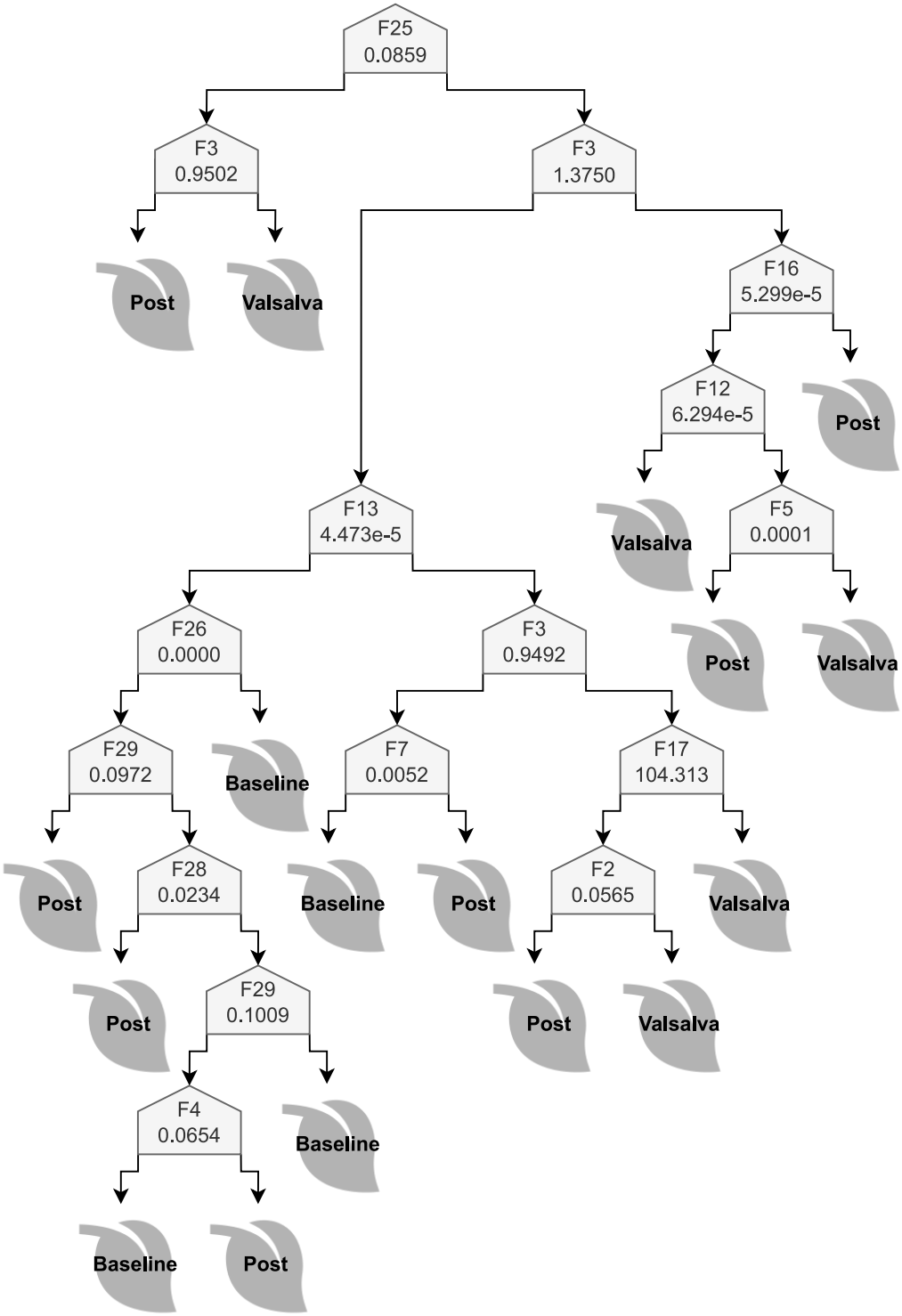

Figure 3.22 – Decision tree generated for the evaluation of MLC during Valsalva. Branches and leaves growing to the right correspond to values above the threshold established for each feature, while branches and leaves growing to the left represent values below or equal to the threshold.

The number of times each decision tree selected a feature can be considered as an indicator of relevance associated with that feature, since the training algorithm has established such a feature to be useful in determining the class to which a sample belongs by setting a threshold based on the values calculated for the feature concerned. In that order of ideas, it can be seen in Table 3.8 that both the decision tree trained for apnea detection and the one trained for Valsalva detection assigned the highest relevance to feature F3, corresponding to the mean of the SCG norm filtered using Filter 1, which is the low-pass filter designed to extract from signals the frequency component associated with respiration. This fact, besides being extremely interesting, is of great importance for the obtained results, since it demonstrates how the decision trees have managed to associate the changes in respiration with the cardiorespiratory events to be detected, given that, in a logical way, a good method of detecting these events is to identify when respiration has stopped.

Another interesting detail regarding the selected features is that the decision tree trained to detect apnea-related events only used features coming from unfiltered signals or filtered with Filter 1, which may suggest that this decision tree is basing its results considering only variations in respiration but not in CVS, which may also be logical since apnea is a mostly respiratory event, at least under the conditions of the performed tests. On the other hand, the decision tree trained to detect events related to the Valsalva maneuver does make use of several features derived from signals filtered with Filters 2 and 3, which suggests a greater influence of the variations measured in the cardiac vibration components in determining the final result of the detection of this decision tree, as it is evident that the Valsalva maneuver has a more significant effect on the hemodynamic behavior of the cardiovascular system by increasing the pressure inside the chest of the volunteer, as could also be observed in the results obtained with the first group of tests.

One relevant detail regarding the structure and threshold values of the decision trees shown in Figures 3.21 and 3.22 is the similarity at the base of both trees (considering the upper part of the figures as the base of the decision tree), which shows the use of the feature F3 with quite similar threshold values, suggesting that the decision tree trained for Valsalva detection performs an evaluation of the state of respiration before evaluating the state of the cardiac vibration measurements. This can also be interpreted to mean that the low-pass filter generates features with global character appropriate for a first level of detection, while the high-pass and band-pass filters generate features that highlight finer details of the signal that are more appropriate for providing greater accuracy to the final detection. This behavior can be compared to the operation of filters in a deep neural networks, which relate to global features being in the shallower layers and focus on fine details being in the deeper layers.

Real-time detection of the cardiorespiratory events using the MLC

Figures 3.23 and 3.24 show representative examples of the cardiac signals measured with the acquisition system and the MLC output for the apnea and Valsalva configurations, respectively. It is worth mentioning that for test signals it was considered to establish a 1-second delay for the transition of states from one class to another, this consideration is due to the time it takes the MLC to generate a new output, which is relative to the size (duration) of the samples used for training (each sample corresponds to 1 second of signal measurement in the case of the configuration implemented for this work). Additionally, the values assigned by the MLC to each class in the apnea configuration are 0, 1 and 2 for Baseline, Apnea and Post-apnea, respectively, and likewise such values in the Valsalva configuration are 0, 1 and 2 for Baseline, Valsalva and Post-Valsalva, respectively. No processing was applied to the signals shown in these figures to obtain a better representation of the data read by the MLC. It can be clearly seen how the detection of the different classes is effective for both configurations, being evident a greater confusion between the Baseline and Post-apnea/Valsalva classes, which was expected since the decision trees are putting a great weight on the breathing state in order to classify a sample between one class and another, so it is theoretically easier to differentiate the Apnea and Valsalva classes from the other classes because during these stages the volunteer is holding the breath.

Table 3.9 shows the results of the evaluation measures applied to the training and testing stages of the MLC. A first evident detail in this table is that both decision trees show an overfit to the training data, especially the decision tree trained for the Valsalva configuration that basically obtains a perfect score. This overfitting to the training data can be explained by the design of the developed tests, which was intended to preliminary evaluate the hypothesis that the MLC embedded in the LSM6DSOX sensor can be used to detect different cardiorespiratory events, so the implemented methods sought to be as simple as possible to achieve a validation of the stated hypothesis without incurring in strategies that appeared to force a favorable result. In this way, the use of methods usually used to improve the performance of machine learning algorithms, such as data augmentation, previous feature selection, the use of optimization algorithms, among others, was omitted. Nevertheless, this type of methods can be used in future works with the purpose of developing a sufficiently robust configuration that allows to exploit the maximum potential of the MLC.

Although the decision trees are over-fitted to the training data, the evaluation measures obtained on the test data are sufficiently high to demonstrate the capability of the MLC to perform tasks associated with the detection of cardiorespiratory events. The implementation of multiple evaluation measures allows to see that the biggest challenge encountered for both the apnea and Valsalva settings was the detection of the Post-apnea and Post-Valsalva classes, which is mainly attributable to the high importance that the decision tree structure is giving

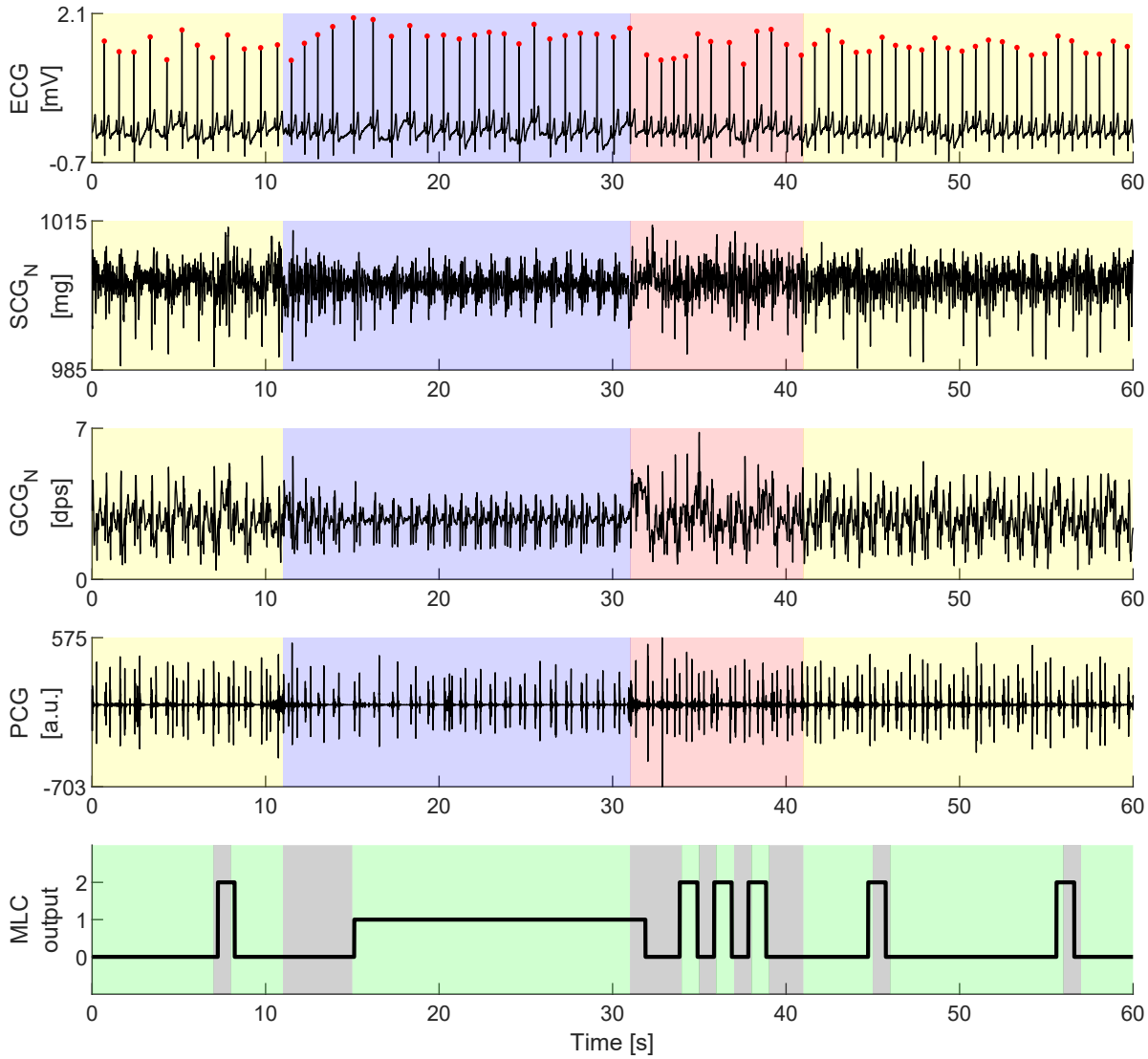

Figure 3.23 – Representative example of test signals taken during apnea to evaluate the MLC output. The red dots over the ECG plot correspond to detected R peaks. The yellow, blue and red backgrounds correspond to the Baseline, Apnea and Post-apnea stages, respectively. The green and gray backgrounds in the MLC output plot correspond to the correct and erroneous detected classes, respectively.

to the breathing state, making it difficult to differentiate these classes from the Baseline class because the breathing state is quite similar between all of them. One reason why decision trees show this tendency to rely on breathing-related features may also be due to the simplicity of the statistical measures used to calculate the features, which can overshadow important details contained in the CVS, leading to problems like, for example, the inability to differentiate the specific information of S1 and S2 into the features content.

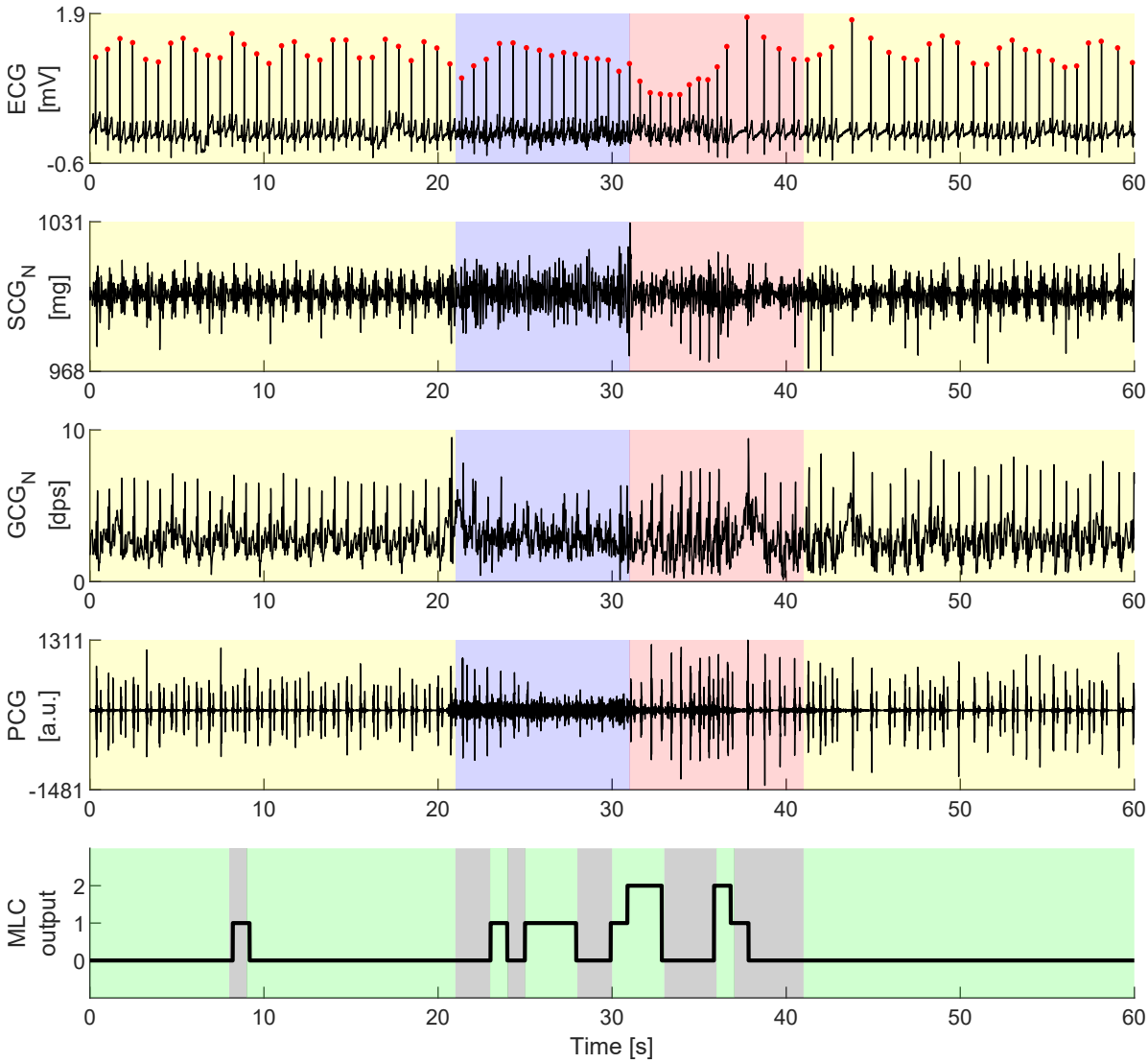

Figure 3.24 – Representative example of test signals taken during Valsalva to evaluate the MLC output. The red dots over the ECG plot correspond to detected R peaks. The yellow, blue and red backgrounds correspond to the Baseline, Valsalva and Post-Valsalva stages, respectively. The green and gray backgrounds in the MLC output plot correspond to the correct and erroneous detected classes, respectively.

3.5 Discussion

This chapter presented, to our knowledge, the first prototype system for cardiac signal acquisition implementing a MEM sensor with an embedded MLC for the monitoring of hemodynamic variations on-the-edge, by detecting acute cardiorespiratory events such as apnea and Valsalva maneuver. The initial experiments were divided into two sets of tests. Results obtained from the first set compared the measured CVS to a gold standard PCG signal, showing a high correlation

		Class	Evaluation measure					
			SEN	**SPC**	**PRE**	**G-mean**	**F1 score**	**ACC**
Apnea evaluation	**Train**	Baseline	1.0000	0.8778	0.8911	0.9369	0.9424	0.9389
		Apnea	0.9333	1.0000	1.0000	0.9661	0.9655	
		Post-apnea	0.7667	1.0000	1.0000	0.8756	0.8679	
	Test	Baseline	0.9111	0.6667	0.7321	0.7794	0.8119	0.7667
		Apnea	0.7500	0.9750	0.9375	0.8551	0.8333	
		Post-apnea	0.3667	0.9400	0.5500	0.5871	0.4400	
Valsalva evaluation	**Train**	Baseline	1.0000	1.0000	1.0000	1.0000	1.0000	1.0000
		Valsalva	1.0000	1.0000	1.0000	1.0000	1.0000	
		Post-valsalva	1.0000	1.0000	1.0000	1.0000	1.0000	
	Test	Baseline	0.8917	0.6833	0.8492	0.7806	0.8699	0.7556
		Valsalva	0.7000	0.9333	0.6774	0.8083	0.6885	
		Post-valsalva	0.2667	0.9000	0.3478	0.4899	0.3019	

Table 3.9 – Performance of the MLC for classifying cardiorespiratory events.

between both types of signals in terms of both their timing and magnitude characteristics. The second set of tests allowed us to evaluate the feasibility to use the MLC embedded into the MEM sensor to detect the targeted cardiorespiratory events, even by using a basic configuration that leaves open the possibility for a wide margin of improvement of the results in future approaches.

The prototype acquisition system was developed to measure reliable signals that accurately represent the mechanical behavior of the heart. For this purpose, the analyses associated with the morphology of the acquired CVS were focused on time and magnitude characteristics, since these are the most commonly associated with different types of hemodynamic parameters in the literature. It was possible to measure the signal-to-noise ratio of the main components of the CVS. The obtained values were consistent with those obtained with the gastric implant studied in the previous chapter and with those found in the literature [149, 150, 126]. In addition, the implemented calibration process allowed for the measurement of the different signals with a synchronization error lower than 2 ms, which is appropriate considering that in some clinical applications variations lower than 3 ms in the systolic and diastolic periods can be neglected [24]. Furthermore, the values obtained for parameters $t1$ and $t3$ compared to the gold standard, which allow calculation of systole and diastole duration, were mostly in agreement with typical error values for the estimation of cardiac event intervals in the state of the art, which can vary between

5 and 10 ms, even when using techniques such as deep learning [161, 121].

The preliminary experimental framework was designed with the purpose of performing measurements during acute changes in the hemodynamic parameters of the volunteers, in such a way that these changes would be measurable through the sensors of the system without needing to involve invasive or risky interventions for the volunteers. Multiple works in the literature have implemented experimental routines that include an apnea stage during the measurement of different types of CVS to evaluate the cardiorespiratory response of the patients [162, 71, 163], as well as other works have studied such response by measuring CVS during the Valsalva maneuver [15, 164]. These cardiorespiratory events are very useful in the experimental setting, since they allow generating significant variations in the hemodynamic response in a safe way for the patient. However, there are some disadvantages associated with this type of strategies, which mainly correspond to the inclusion of noise in the target signals due to patient movements during the execution of the routines, in addition to the fact that the changes to be studied occur in very short periods of time, which sometimes makes the signals almost impossible to analyze even by an expert human operator [165].

The main feature of the cardiac signal acquisition system described in this chapter is the use of the MLC embedded in the LSM6DSOX sensor for automatic detection of cardiorespiratory events, such as apnea and Valsalva maneuver, through the analysis of multimodal MCG signals. The LSM6DSOX sensor has been previously used in the literature to leverage the functionalities offered by its embedded MLC in human activity recognition (HAR) tasks, such as sitting, standing or walking [166], which are in line with the activities proposed by the manufacturer as it is a sensor intended for use in mobile devices such as smartphones and smartwatches [160]. Other studies have explored more complex applications such as the detection of falls occurred in occupational risk environments, obtaining quite promising results in terms of sensitivity (0.97), specificity (0.91) and accuracy (0.95) [167, 168]. Considering that this type of technology is fairly new and has just begun to be extrapolated to other areas of research, this work represents, to our knowledge, the first approach developed to evaluate the feasibility of using this technology for the automatic detection of cardiorespiratory events by MCG measurement on-the-edge.

The main performance results obtained in this preliminary work with the MLC are real-time detection of apnea with sensitivity, specificity and precision of 0.75, 0.98 and 0.94, respectively, and real-time detection of Valsalva with sensitivity, specificity and precision of 0.70, 0.93 and 0.68, respectively. Other studies in the literature have achieved sensitivity of 0.58 and specificity of 0.98 in the automatic detection of respiratory events (apnea and hypopnea) using a positive airway pressure device [169], sensitivity of 0.86 and precision of 0.61 (0.89 and 0.59 in real time, respectively) using a cardiorespiratory Holter device [170, 171], and sensitivity of 0.92 with precision of 0.91 using nasal pressure signals [172]. Additionally, other studies have employed more advanced techniques involving the use of multimodal data from SCG, ECG and photoplethys-

mography, achieving high sensitivity (100%) and specificity (95%) values [173], in addition to the use of deep learning techniques, among other machine learning algorithms [174, 175]. However, all these works propose approaches where signal processing and detection of cardiorespiratory events is performed outside the sensor, requiring the use of an additional device with a microprocessor or a micro-controller.

Obviously, we are not claiming a direct comparison of our results with these works of the literature, since the preliminary work made in this chapter was mainly focused on a technological feasibility evaluation. Many limitations remain in this work, that will be overcome in future works of the team. Concerning the methodological and technical aspects, i) sensors may be still optimized in terms of data acquisition and conditioning; ii) signal processing methods may be embedded into the processing chain and iii) further developments on the machine learning phase, such as data augmentation, feature selection or training regularization should be performed. Also a number of unexploited features of the MLC in the LSM6DSOX sensor may be explored, for instance, the possibility of configuring up to 8 different decision trees that can interact with each other by means of a finite state machine [160]. Finally, a major limitation of this study is related to the very limited set of data used for learning and testing. A new specific clinical protocol, in line with our previous works in this field [23], will be performed in the future.

Despite the many advantages and opportunities offered by the cardiac signal acquisition system presented in this work, it is also affected by some problems that can complicate its use in certain types of applications. Beyond the problems associated with all systems of this type, such as the presence of noise and disturbances in the measured signals, the main difficulty facing the use of this system is that it only offers basic methods to address machine learning tasks. Although decision trees have been shown to be quite effective for the solution of multiple classification and detection problems, a large part of their potential lies on the features generated from the analyzed data, which in this case, consist only of simple statistical features that may not be sufficient to represent the relevant information in the signals regarding the task to be developed. Even so, this system can be effectively used in tasks that do not require a high complexity in the analysis of raw MCG signals, and it is expected that future advances in the development of this type of sensors will allow the incorporation of more advanced models that can make use of more complex and specific features. This is not so far from being achieved considering the latest technological advances in microchip fabrication, such as the possibility of implementing ultra-compact binary neural networks that require very low hardware capacity to operate [176], the development of analog computational processing that allows optimizing the operations that a microprocessor can perform [177], and the development of techniques that allow taking full advantage of the benefits of deep neural networks at physical scale to improve their energy efficiency and speed in real time applications [178].

3.6 Conclusion

This chapter presented the design, construction, calibration and initial evaluation of a specialized prototype system for the acquisition of multimodal cardiac signals. This system has been initially validated, with the capability to measure MCG, ECG and PCG signals synchronously with a high signal-to-noise ratio. The main feature of the system is the integration of a MLC embedded in the MCG sensor, which has demonstrated preliminary feasibility for recognizing and classifying patterns associated with multiple cardiorespiratory events involving variations in hemodynamic parameters, such as apnea and Valsalva maneuver. Although still preliminary, the obtained results represent, to our knowledge, the first attempt to detect cardiorespiratory events from CVS through an on-the-edge, machine learning inference model, embedded into the sensor. The main challenge in the use of this system lies in the simplicity of the methods offered by the MLC to perform automatic detection tasks, which offer ease of implementation but sacrifice the possibility of addressing highly complex tasks with good accuracy. Future work with the use of this system will be oriented to the acquisition of signals on a larger number of subjects, especially including patients diagnosed with heart failure, to determine the usefulness of the system in the development of future cardiac monitoring devices with the ability to early and automatically detect cardiac decompensation events.

Chapter 4

Conclusions and perspectives

The prognosis, symptoms and quality of life of patients with HF have notably improved with the latest advances in pharmacological and medical device treatments, which should be accompanied by advances in hemodynamic monitoring with implantable and wearable devices for regular optimization of treatments in a patient-specific manner, with the purpose of preventing decompensation events that can lead to hospitalization. In this thesis, signal acquisition and processing methods are proposed to make the best use of inertial units in the monitoring of patients with heart failure, by efficiently exploiting multimodal information from cardiac vibration signals (CVS), which provide relevant information on cardiac mechanical activity in relation to the study of hemodynamic parameters. The main contributions of the work developed in this thesis can be summarized as follows:

— The presentation of initial preclinical evidence on the feasibility of chronic cardiovascular monitoring from a minimally invasive implantable cardiac device placed in the gastric fundus.

— The development of a specialized prototype system for the acquisition of multimodal cardiac signals, which integrates a machine learning core (MLC) embedded in a MEM sensor for on-the-edge recognition and classification of multiple cardiorespiratory events related to hemodynamic variations.

— The proposition of an efficient and easy-to-implement algorithm based on context features to obtain the final detection instants of the main components of CVS commonly related to the main heart sounds.

4.1 Chronic cardiovascular monitoring through a minimally invasive gastric implant

In Chapter 2, we performed the characterization of signals acquired in pre-clinical experimentation using a gastric implant for evaluating the hypothesis that CVS can be captured from a small monitoring implant positioned at the gastric fundus, since this anatomical site seems a good candidate for long-term cardiovascular monitoring because it is physically close to the heart. Such implant is capable of measuring electrophysiological and 3D accelerometer cardiac

data and could be safely administered using minimally invasive implantation techniques such as gastroscopy, improving patient comfort and adherence to the treatments involving implantable devices. Three different versions of the implant were used to perform the proposed experiments, which were focused on the comparison of the signals acquired from the gastric fundus with reference data acquired through standard thoracic site sensors, and the assessing of the feasibility to estimate longitudinal cardiovascular markers from the gastric site.

The obtained results showed that time variation of markers such as heart rate and heart sound duration and amplitude measured with the implant were highly correlated with the reference signals, which is of great relevance for the intended utility of the implant in long-term monitoring of chronic HF. Additionally, when SNR values in the accelerometry signals are higher than 6 dB or heart sound contrast is higher than 2, the S1 and S2 components can be correctly segmented and hemodynamic markers can be estimated from these data, showing preclinical evidence on the feasibility of chronic cardiovascular monitoring in HF patients by using this implant. However, the main challenge for the use of the implant remains in optimizing the signal-to-noise ratio, in particular for handling some noise sources that are specific to the gastric acquisition site and can induce disturbances mainly in the measured CVS.

These results directly address the achievement of the first specific objective of this thesis. Considering that the satisfactory estimation of hemodynamic parameters could only become effective during specific periods of time that depend on the acquisition conditions, ongoing work should aim to the proposition of adaptive methods that will trigger data acquisition at the implant when specific noise level criteria are met and in further preclinical evaluation.

4.2 Cardiorespiratory events detection on-the-edge using a multimodal cardiac system

In Chapter 3, a prototype acquisition system to synchronously measure mechanocardiographic (MCG), electrocardiographic (ECG) and phonocardiographic (PCG) signals in a noninvasive manner was developed. Such system incorporates the measurement of CVS through the use of a cutting-edge, ultra-low-power MEM sensor, which has the special feature of integrating an MLC that allows the deployment of machine learning applications on-the-edge. Such a feature raises the hypothesis that this type of technology could be exploited for the future development of implantable or wearable devices for monitoring cardiac patients, with the advantage of enabling the use of machine learning on-the-edge to improve the efficiency of such devices in terms of real-time processing, speed, memory, size, power consumption, and even accuracy. In order to perform an initial evaluation of the system in light of such hypothesis, a first group of tests was performed to validate the correlation between the MCG and PCG signals, taking the latter as the gold standard reference, and a second group of tests were developed for the purpose of

conducting a preliminary evaluation of the hypothesis that the MLC embedded in the MEM sensor can be used to automatically detect cardiorespiratory events related to hemodynamic variations.

The obtained results showed satisfactory levels of correlation between the measured CVS and the PCG reference on time and magnitude characteristics, which are the most commonly associated with different types of hemodynamic parameters in the literature. In addition, a synchronization error lower than 2 ms between the different sensors, reflected the benefits of the particular effort given to the correct temporal synchronization of the signals, acquired through different sensors, with different protocols and heterogeneous resolutions. Furthermore, the experimental framework designed to performing measurements during acute changes in hemodynamic parameters allowed to obtain appropriate performance results, with real-time detection of apnea with sensitivity, specificity and precision of 0.75, 0.98 and 0.94, respectively, and real-time detection of Valsalva maneuver with sensitivity, specificity and precision of 0.70, 0.93 and 0.68, respectively. These results demonstrate preliminary feasibility for recognizing and classifying patterns associated with multiple cardiorespiratory events involving variations in hemodynamic parameters on-the-edge.

These results directly address the achievement of the third specific objective of this thesis, and pose a new perspective where the benefits offered by the use of the MLC for processing and analysis of CVS on-the-edge, could be leveraged to address the proposed future work with the use of the gastric implant described above, where the processing of the signals acquired by the implant could be performed during specific noise conditions, which would be easily detectable by the MLC. The main challenge in the use of this system lies in the simplicity of the methods offered by the MLC to perform automatic detection tasks, which offer ease of implementation but sacrifice the possibility of addressing highly complex tasks with good accuracy. Future work with the use of this system will be oriented to the acquisition of signals on a larger number of subjects, especially including patients diagnosed with heart failure, to determine the usefulness of the system in the development of future cardiac monitoring devices with the ability to early and automatically detect cardiac decompensation events.

4.3 Context-based algorithm for efficiently detecting the main components of CVS

An efficient and easy-to-implement algorithm based on context features was proposed in Chapter 2 to obtain the final detection instants for S1 and S2 from the fusion of multiple candidate detections of the main CVS components measured with a 3D accelerometer (Algorithm 1). This algorithm has the additional advantage of allowing the easy incorporation of other CVS sources such as PCG and GCG, This was evidenced by the fact that it was also used to process

the signals acquired with the system developed in Chapter 3. The development of this algorithm directly address the achievement of the second specific objective of this thesis, reasserting the cross-cutting scope of the entire content of this thesis in the perspective of leveraging CVS for the development of methods and tools that can be used in the long-term cardiovascular monitoring of patients diagnosed with chronic heart disease such as HF.

Appendix A

Second-day baseline signals

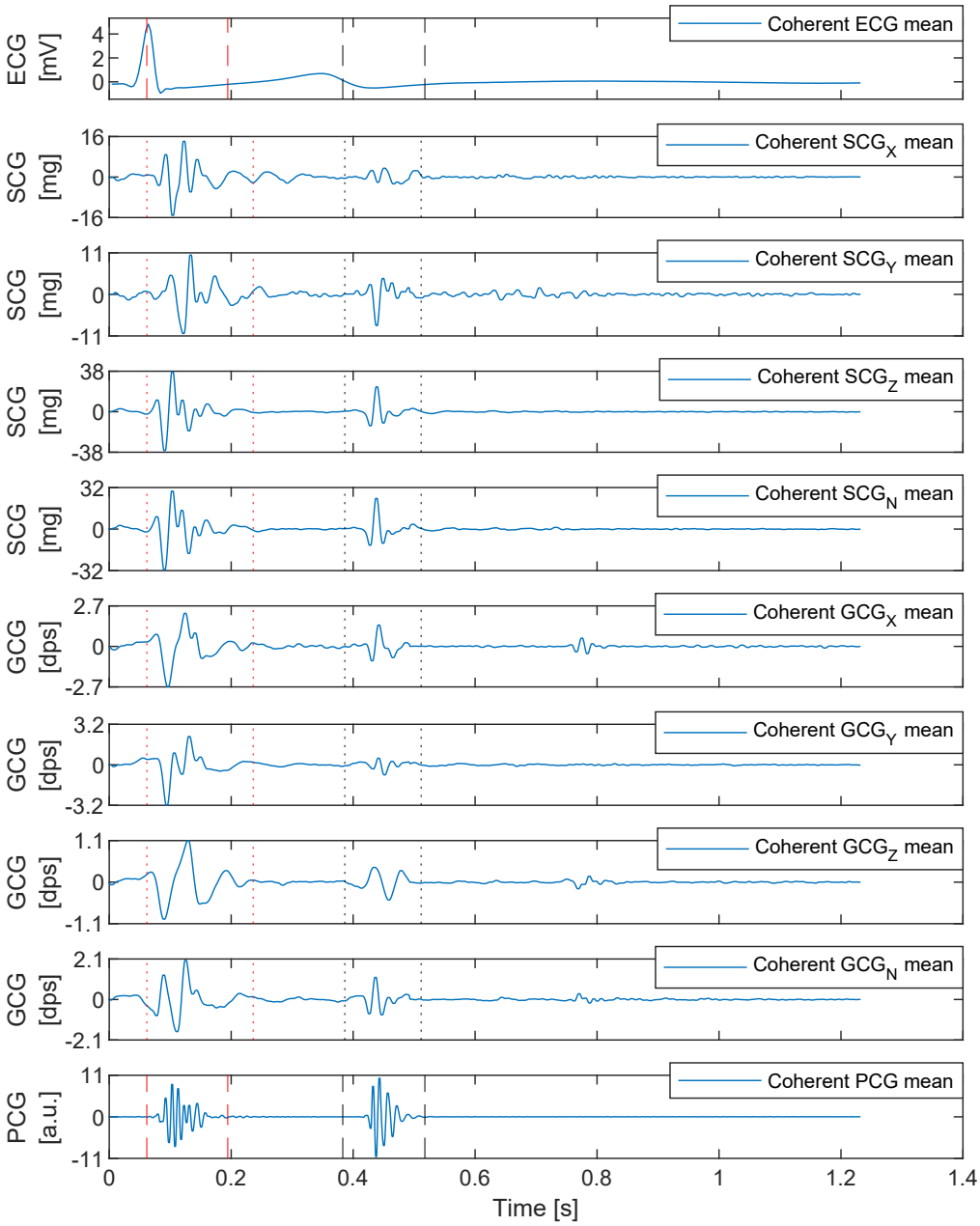

Figure A.1 – Representative example of signals taken in volunteer 1 on the second day. The vertical lines represent the detection times of the first and second heart sounds in red and black, respectively. The dotted lines represent detection using the MCG, while the dashed lines represent detection using the PCG.

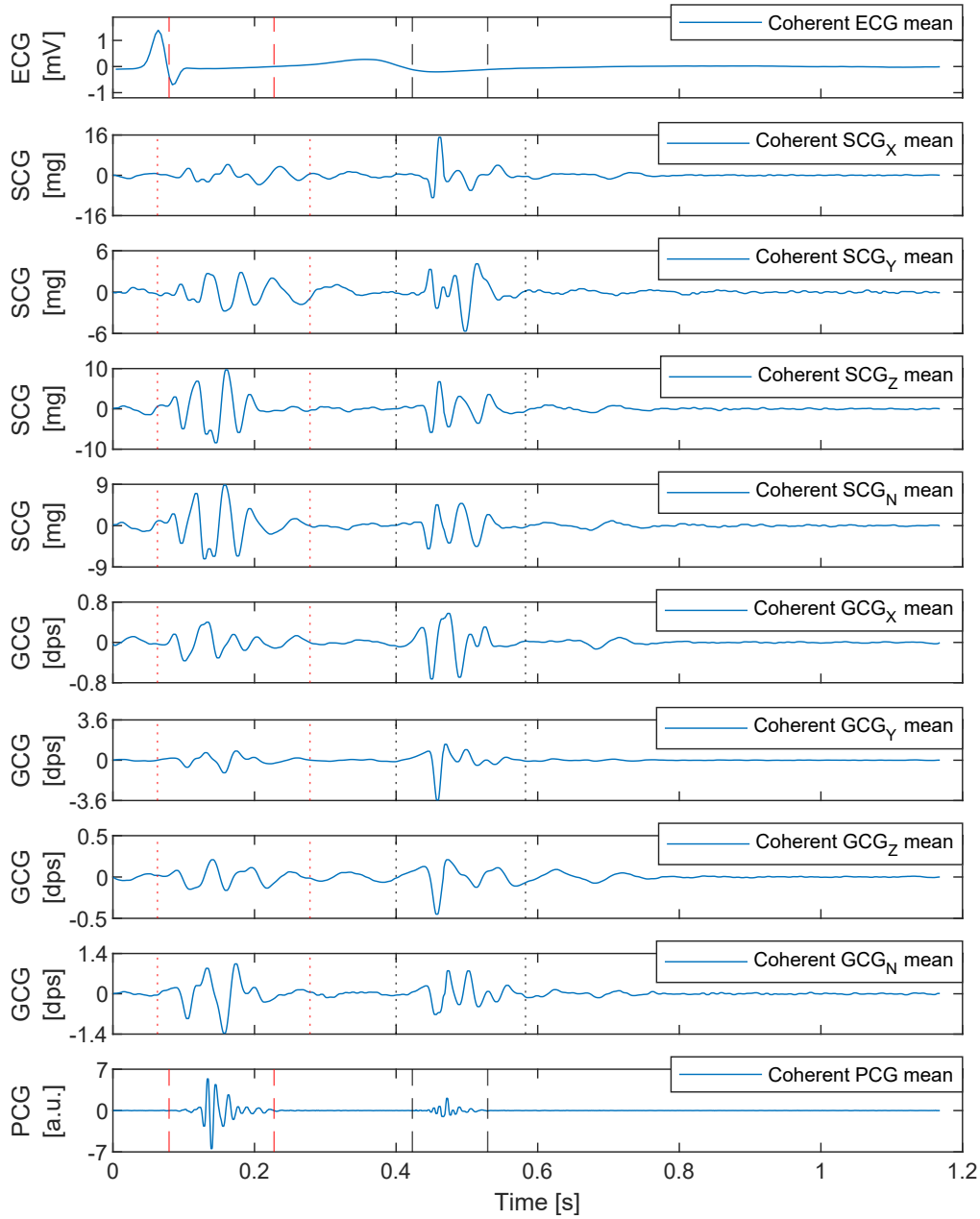

Figure A.2 – Representative example of signals taken in volunteer 2 on the second day. The vertical lines represent the detection times of the first and second heart sounds in red and black, respectively. The dotted lines represent detection using the MCG, while the dashed lines represent detection using the PCG.

Appendix B

Time-profiles for volunteer 2

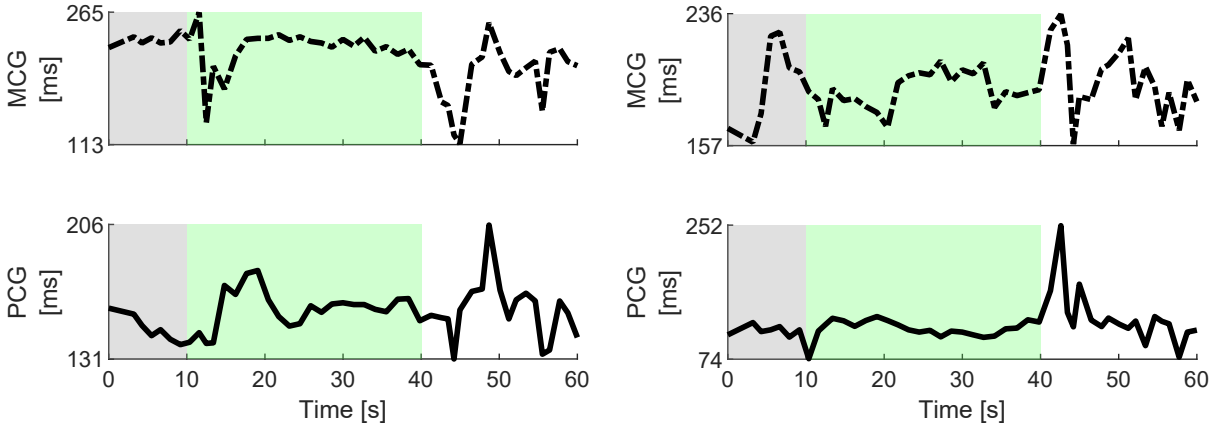

(a) Time-profile of S1 duration (b) Time-profile of S2 duration

Figure B.1 – Representative example of evolution over time of heart sounds duration measured on volunteer 2 during apnea. Dash-dotted lines correspond to the MCG signals and solid lines correspond to the reference PCG signals. The gray, green and white backgrounds correspond to the baseline, apnea and recovery stages, respectively.

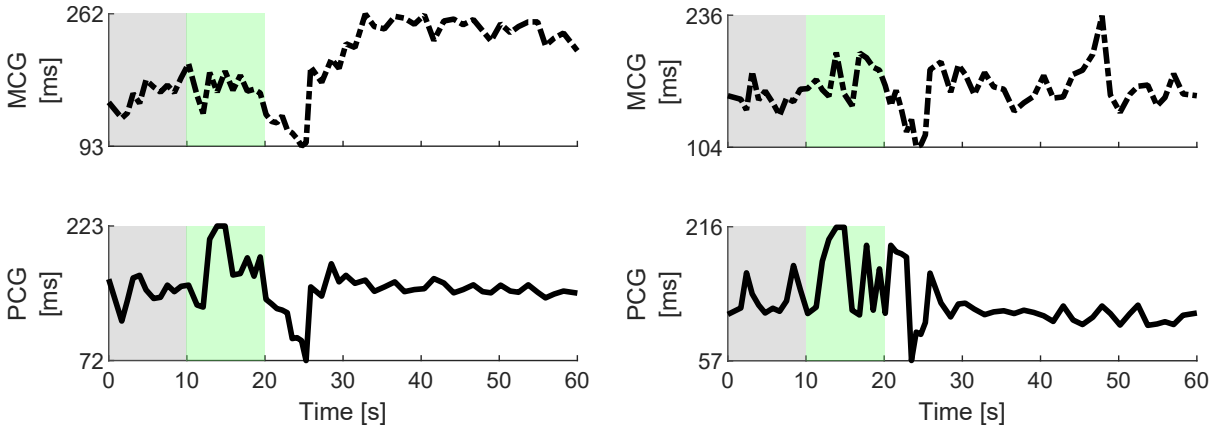

(a) Time-profile of S1 duration (b) Time-profile of S2 duration

Figure B.2 – Representative example of evolution over time of heart sounds duration measured on volunteer 2 during Valsalva. Dash-dotted lines correspond to the MCG signals and solid lines correspond to the reference PCG signals. The gray, green and white backgrounds correspond to the baseline, valsalva and recovery stages, respectively.

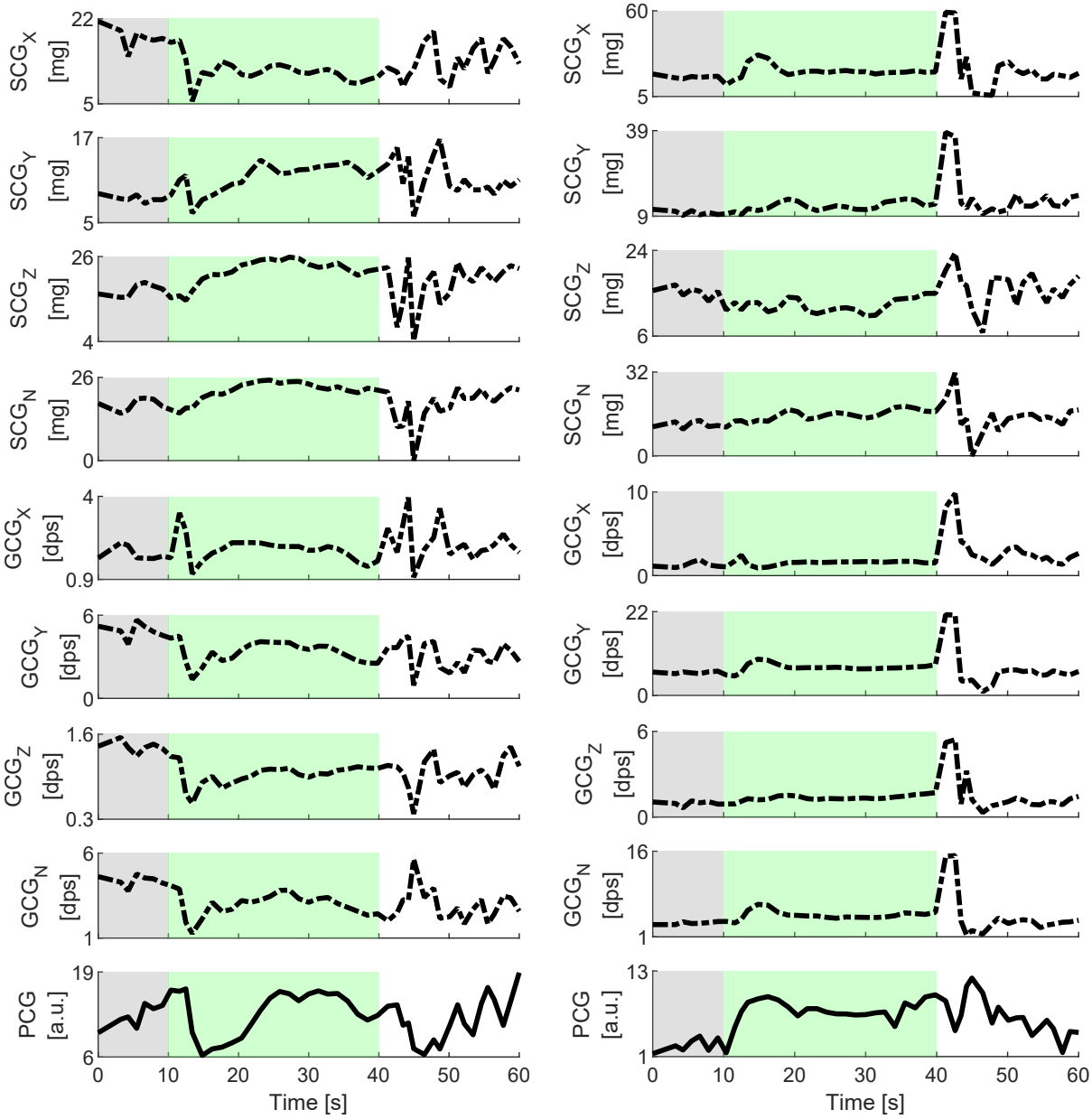

(a) Time-profile of S1 peak-to-peak value

(b) Time-profile of S2 peak-to-peak value

Figure B.3 – Representative example of evolution over time of heart sounds peak-to-peak value measured on volunteer 2 during apnea. Dash-dotted lines correspond to the MCG signals and solid lines correspond to the reference PCG signals. The gray, green and white backgrounds correspond to the baseline, apnea and recovery stages, respectively.

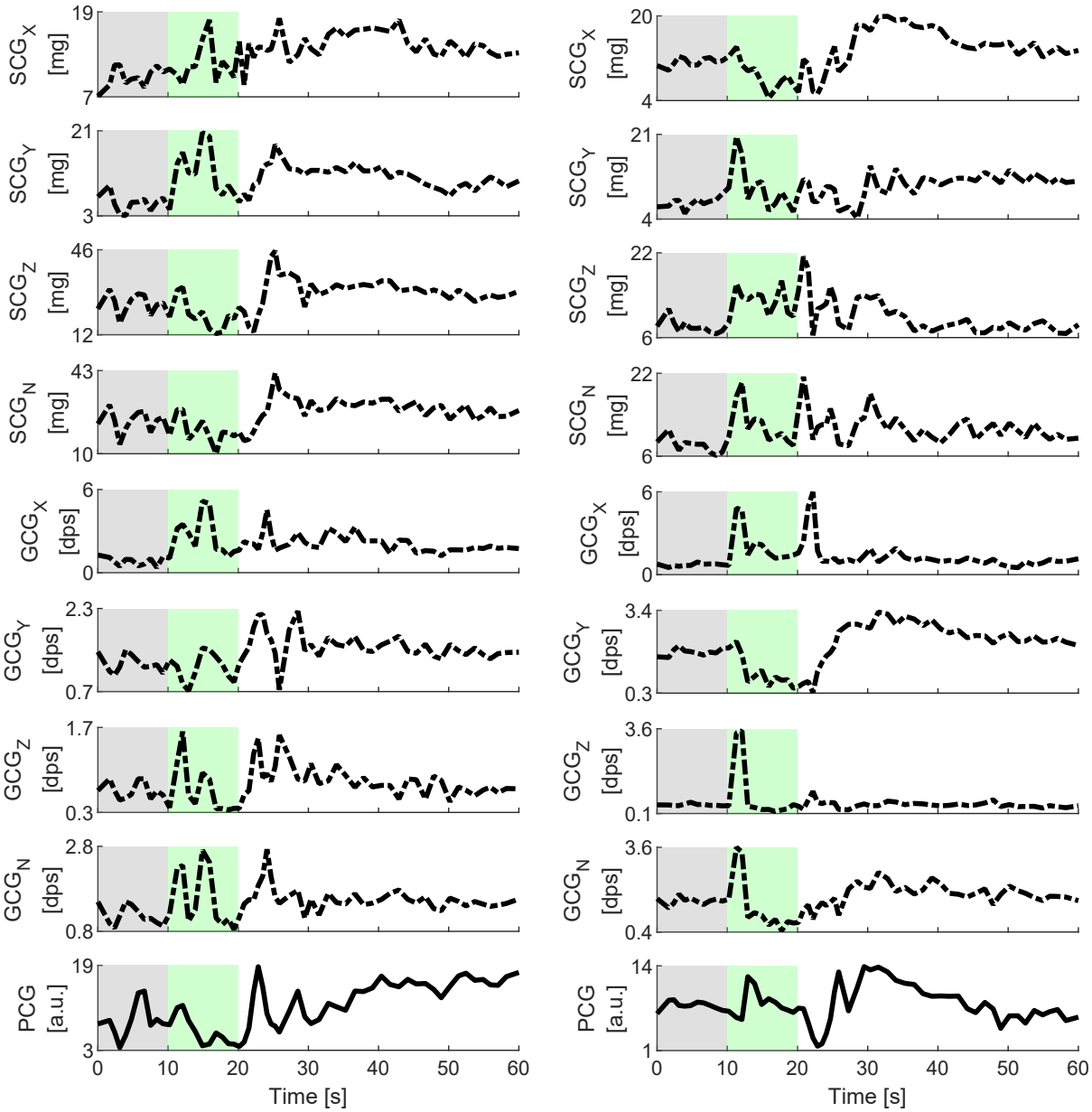

(a) Time-profile of S1 peak-to-peak value

(b) Time-profile of S2 peak-to-peak value

Figure B.4 – Representative example of evolution over time of heart sounds peak-to-peak value measured on volunteer 2 during Valsalva. Dash-dotted lines correspond to the MCG signals and solid lines correspond to the reference PCG signals. The gray, green and white backgrounds correspond to the baseline, valsalva and recovery stages, respectively.

Bibliography

[1] W. H. Organization *et al.*, "Noncommunicable diseases progress monitor 2022," 2022.

[2] World Health Organization, "Cardiovascular diseases (cvds)," 2022, accessed: 2022-09-18. [Online]. Available: https://www.who.int/en/news-room/fact-sheets/detail/cardiovascular-diseases-(cvds)

[3] G. A. Roth, G. A. Mensah, C. O. Johnson, G. Addolorato, E. Ammirati, L. M. Baddour, N. C. Barengo, A. Z. Beaton, E. J. Benjamin, C. P. Benziger *et al.*, "Global burden of cardiovascular diseases and risk factors, 1990–2019: update from the gbd 2019 study," *Journal of the American College of Cardiology*, vol. 76, no. 25, pp. 2982–3021, 2020.

[4] A. Timmis, N. Townsend, C. P. Gale, A. Torbica, M. Lettino, S. E. Petersen, E. A. Mossialos, A. P. Maggioni, D. Kazakiewicz, H. T. May *et al.*, "European society of cardiology: cardiovascular disease statistics 2019," *European heart journal*, vol. 41, no. 1, pp. 12–85, 2020.

[5] G. Savarese, P. M. Becher, L. H. Lund, P. Seferovic, G. Rosano, and A. J. Coats, "Global burden of heart failure: a comprehensive and updated review of epidemiology," *Cardiovascular Research*, 2022.

[6] J. G. Cleland, J.-C. Daubert, E. Erdmann, N. Freemantle, D. Gras, L. Kappenberger, and L. Tavazzi, "Longer-term effects of cardiac resynchronization therapy on mortality in heart failure [the cardiac resynchronization-heart failure (care-hf) trial extension phase]," *European heart journal*, vol. 27, no. 16, pp. 1928–1932, 2006.

[7] A. S. Desai, A. Bhimaraj, R. Bharmi, R. Jermyn, K. Bhatt, D. Shavelle, M. M. Redfield, R. Hull, J. Pelzel, K. Davis *et al.*, "Ambulatory hemodynamic monitoring reduces heart failure hospitalizations in "real-world" clinical practice," *Journal of the American College of Cardiology*, vol. 69, no. 19, pp. 2357–2365, 2017.

[8] G. Plicchi, E. Marcelli, M. Parlapiano, and T. Bombardini, "Pea i and pea ii based implantable haemodynamic monitor: pre clinical studies in sheep," *Europace*, vol. 4, no. 1, pp. 49–54, 2002.

[9] P. Bordachar, L. Labrousse, S. Ploux, J.-B. THAMBO, S. Lafitte, P. Reant, P. Jais, M. Haissaguerre, J. Clementy, and P. D. SANTOS, "Validation of a new noninvasive

device for the monitoring of peak endocardial acceleration in pigs: implications for optimization of pacing site and configuration," *Journal of cardiovascular electrophysiology*, vol. 19, no. 7, pp. 725–729, 2008.

[10] P. K. Jain and A. K. Tiwari, "Heart monitoring systems—a review," *Computers in biology and medicine*, vol. 54, pp. 1–13, 2014.

[11] O. T. Inan, P.-F. Migeotte, K.-S. Park, M. Etemadi, K. Tavakolian, R. Casanella, J. Zanetti, J. Tank, I. Funtova, G. K. Prisk *et al.*, "Ballistocardiography and seismocardiography: A review of recent advances," *IEEE journal of biomedical and health informatics*, vol. 19, no. 4, pp. 1414–1427, 2015.

[12] M. M. H. Shandhi, B. Semiz, S. Hersek, N. Goller, F. Ayazi, and O. T. Inan, "Performance analysis of gyroscope and accelerometer sensors for seismocardiography-based wearable pre-ejection period estimation," *IEEE journal of biomedical and health informatics*, vol. 23, no. 6, pp. 2365–2374, 2019.

[13] P. Gupta, M. J. Moghimi, Y. Jeong, D. Gupta, O. T. Inan, and F. Ayazi, "Precision wearable accelerometer contact microphones for longitudinal monitoring of mechano-acoustic cardiopulmonary signals," *NPJ digital medicine*, vol. 3, no. 1, pp. 1–8, 2020.

[14] A. I. Hernández, F. Ziglio, A. Amblard, L. Senhadji, and C. Leclercq, "Analysis of endocardial acceleration during intraoperative optimization of cardiac resynchronization therapy," in *2013 35th Annual International Conference of the IEEE Engineering in Medicine and Biology Society (EMBC)*. IEEE, 2013, pp. 7000–7003.

[15] C. Gallet, V. Le Rolle, J.-L. Bonnet, C. Henry, A. Hagège, P. Mabo, G. Carrault, and A. I. Hernández, "Analysis of endocardial micro-accelerometry during valsalva maneuvers," in *2016 Computing in Cardiology Conference (CinC)*. IEEE, 2016, pp. 21–24.

[16] P. Bordachar, S. Garrigue, P. Ritter, S. Ploux, L. Labrousse, C. Casset, M. Haissaguerre, and P. Dos Santos, "Contributions of a hemodynamic sensor embedded in an atrial lead in a porcine model," *Journal of cardiovascular electrophysiology*, vol. 22, no. 5, pp. 579–583, 2011.

[17] J. P. Boehmer, R. Hariharan, F. G. Devecchi, A. L. Smith, G. Molon, A. Capucci, Q. An, V. Averina, C. M. Stolen, P. H. Thakur *et al.*, "A multisensor algorithm predicts heart failure events in patients with implanted devices: results from the multisense study," *JACC: Heart Failure*, vol. 5, no. 3, pp. 216–225, 2017.

[18] M. Cao, R. S. Gardner, R. Hariharan, D. G. Nair, C. Schulze, Q. An, P. H. Thakur, B. Kwan, Y. Zhang, and J. P. Boehmer, "Ambulatory monitoring of heart sounds via an

implanted device is superior to auscultation for prediction of heart failure events," *Journal of cardiac failure*, vol. 26, no. 2, pp. 151–159, 2020.

[19] P. P. Delnoy, E. Marcelli, H. Oudeluttikhuis, D. Nicastia, F. Renesto, L. Cercenelli, and G. Plicchi, "Validation of a peak endocardial acceleration-based algorithm to optimize cardiac resynchronization: early clinical results," *Europace*, vol. 10, no. 7, pp. 801–808, 2008.

[20] A. Voigt, A. Shalaby, and S. Saba, "Continued rise in rates of cardiovascular implantable electronic device infections in the united states: temporal trends and causative insights," *Pacing and clinical electrophysiology*, vol. 33, no. 4, pp. 414–419, 2010.

[21] K. G. Tarakji, O. M. Wazni, S. Harb, A. Hsu, W. Saliba, and B. L. Wilkoff, "Risk factors for 1-year mortality among patients with cardiac implantable electronic device infection undergoing transvenous lead extraction: the impact of the infection type and the presence of vegetation on survival," *Europace*, vol. 16, no. 10, pp. 1490–1495, 2014.

[22] M. Calvo, J.-L. Bonnet, V. Le Rolle, M. Lemonnier, S. Yasuda, W. Oosterlinck, and A. Hernández, "Evaluation of three-dimensional accelerometers for the study of left ventricular contractility," in *2018 Computing in Cardiology Conference (CinC)*, vol. 45. IEEE, 2018, pp. 1–4.

[23] E. Donal, L. Giorgis, S. Cazeau, C. Leclercq, L. Senhadji, A. Amblard, G. Jauvert, M. Burban, A. Hernández, and P. Mabo, "Endocardial acceleration (sonr) vs. ultrasound-derived time intervals in recipients of cardiac resynchronization therapy systems," *Europace*, vol. 13, no. 3, pp. 402–408, 2011.

[24] L. Giorgis, P. Frogerais, A. Amblard, E. Donal, P. Mabo, L. Senhadji, and A. I. Hernández, "Optimal algorithm switching for the estimation of systole period from cardiac microacceleration signals (sonr)," *IEEE Transactions on Biomedical Engineering*, vol. 59, no. 11, pp. 3009–3015, 2012.

[25] P. Ponikowski, A. A. Voors, S. D. Anker, H. Bueno, J. G. Cleland, A. J. Coats, V. Falk, J. R. González-Juanatey, V.-P. Harjola, E. A. Jankowska *et al.*, "2016 esc guidelines for the diagnosis and treatment of acute and chronic heart failure: The task force for the diagnosis and treatment of acute and chronic heart failure of the european society of cardiology (esc) developed with the special contribution of the heart failure association (hfa) of the esc," *European heart journal*, vol. 37, no. 27, pp. 2129–2200, 2016.

[26] C. W. Yancy, M. Jessup, B. Bozkurt, J. Butler, D. E. Casey, M. M. Colvin, M. H. Drazner, G. S. Filippatos, G. C. Fonarow, M. M. Givertz *et al.*, "2017 acc/aha/hfsa focused update

of the 2013 accf/aha guideline for the management of heart failure: a report of the american college of cardiology/american heart association task force on clinical practice guidelines and the heart failure society of america," *Journal of the American College of Cardiology*, vol. 70, no. 6, pp. 776–803, 2017.

[27] A. Taebi, B. E. Solar, A. J. Bomar, R. H. Sandler, and H. A. Mansy, "Recent advances in seismocardiography," *Vibration*, vol. 2, no. 1, pp. 64–86, 2019.

[28] A. Galli, R. J. Montree, S. Que, E. Peri, and R. Vullings, "An overview of the sensors for heart rate monitoring used in extramural applications," *Sensors*, vol. 22, no. 11, p. 4035, 2022.

[29] H. Areiza-Laverde, C. Dopierala, L. Senhadji, F. Boucher, P. Y. Gumery, and A. Hernández, "Analysis of cardiac vibration signals acquired from a novel implant placed on the gastric fundus," *Frontiers in Physiology*, p. 2070, 2021.

[30] M. Linschoten and F. W. Asselbergs, "Capacity-covid: a european registry to determine the role of cardiovascular disease in the covid-19 pandemic," 2020.

[31] W. Committee, T. J. Gluckman, N. M. Bhave, L. A. Allen, E. H. Chung, E. S. Spatz, E. Ammirati, A. L. Baggish, B. Bozkurt, W. K. Cornwell III *et al.*, "2022 acc expert consensus decision pathway on cardiovascular sequelae of covid-19 in adults: myocarditis and other myocardial involvement, post-acute sequelae of sars-cov-2 infection, and return to play: a report of the american college of cardiology solution set oversight committee," *Journal of the American College of Cardiology*, vol. 79, no. 17, pp. 1717–1756, 2022.

[32] M. Patone, X. W. Mei, L. Handunnetthi, S. Dixon, F. Zaccardi, M. Shankar-Hari, P. Watkinson, K. Khunti, A. Harnden, C. A. Coupland *et al.*, "Risks of myocarditis, pericarditis, and cardiac arrhythmias associated with covid-19 vaccination or sars-cov-2 infection," *Nature medicine*, vol. 28, no. 2, pp. 410–422, 2022.

[33] N. L. Bragazzi, W. Zhong, J. Shu, A. Abu Much, D. Lotan, A. Grupper, A. Younis, and H. Dai, "Burden of heart failure and underlying causes in 195 countries and territories from 1990 to 2017," *European Journal of Preventive Cardiology*, vol. 28, no. 15, pp. 1682–1690, 2021.

[34] Agence Nationale de la Recherche, "Digital implantable gastric stethoscope – digs," Aug 2018, accessed: 2022-09-19. [Online]. Available: https://anr.fr/Project-ANR-18-CE19-0008

[35] J. E. Hall and M. E. Hall, *Guyton and hall textbook of medical physiology*, 13rd ed., ser. Guyton Physiology. London, England: Elsevier Health Sciences, May 2015.

[36] S. Standring *et al.*, *Gray's anatomy: the anatomical basis of clinical practice*, 41st ed., ser. Gray's Anatomy. London, England: Elsevier Health Sciences, Sep. 2016.

[37] T. W. Secomb, "Hemodynamics," *Comprehensive physiology*, vol. 6, no. 2, p. 975, 2016.

[38] C. E. Kossmann, "The normal electrocardiogram," *Circulation*, vol. 8, no. 6, pp. 920–936, 1953.

[39] L. Geddes, "Birth of the stethoscope," *IEEE Engineering in Medicine and Biology Magazine*, vol. 24, no. 1, pp. 84–86, 2005.

[40] K. Z. Siejko, P. H. Thakur, K. Maile, A. Patangay, and M.-T. OLIVARI, "Feasibility of heart sounds measurements from an accelerometer within an icd pulse generator," *Pacing and Clinical Electrophysiology*, vol. 36, no. 3, pp. 334–346, 2013.

[41] P. H. Thakur, Q. An, L. Swanson, Y. Zhang, and R. S. Gardner, "Haemodynamic monitoring of cardiac status using heart sounds from an implanted cardiac device," *ESC heart failure*, vol. 4, no. 4, pp. 605–613, 2017.

[42] C. M. Otto, *Textbook of clinical echocardiography*, 6th ed. Philadelphia, PA: Elsevier - Health Sciences Division, Feb. 2018.

[43] D. Kasper, A. Fauci, S. Hauser, D. Longo, J. Jameson, and J. Loscalzo, *Harrison's principles of internal medicine, 19e.* Mcgraw-hill New York, NY, USA:, 2015, vol. 1, no. 2.

[44] M. Leitman, P. Lysyansky, S. Sidenko, V. Shir, E. Peleg, M. Binenbaum, E. Kaluski, R. Krakover, and Z. Vered, "Two-dimensional strain–a novel software for real-time quantitative echocardiographic assessment of myocardial function," *Journal of the American Society of Echocardiography*, vol. 17, no. 10, pp. 1021–1029, 2004.

[45] A. Singh, W. B. Voss, R. W. Lentz, J. D. Thomas, and N. Akhter, "The diagnostic and prognostic value of echocardiographic strain," *JAMA cardiology*, vol. 4, no. 6, pp. 580–588, 2019.

[46] M. J. Benson, N. Silverton, C. Morrissey, and J. Zimmerman, "Strain imaging: An everyday tool for the perioperative echocardiographer," *Journal of Cardiothoracic and Vascular Anesthesia*, vol. 34, no. 10, pp. 2707–2717, 2020.

[47] R. M. Lang, L. P. Badano, V. Mor-Avi, J. Afilalo, A. Armstrong, L. Ernande, F. A. Flachskampf, E. Foster, S. A. Goldstein, T. Kuznetsova *et al.*, "Recommendations for cardiac chamber quantification by echocardiography in adults: an update from the american society of echocardiography and the european association of cardiovascular imaging," *European Heart Journal-Cardiovascular Imaging*, vol. 16, no. 3, pp. 233–271, 2015.

[48] B. Bozkurt, A. J. Coats, H. Tsutsui, M. Abdelhamid, S. Adamopoulos, N. Albert, S. D. Anker, J. Atherton, M. Böhm, J. Butler *et al.*, "Universal definition and classification of heart failure: a report of the heart failure society of america, heart failure association of the european society of cardiology, japanese heart failure society and writing committee of the universal definition of heart failure," *Journal of cardiac failure*, vol. 27, no. 4, pp. 387–413, 2021.

[49] D. C. Brater, "Diuretic therapy," *New England Journal of Medicine*, vol. 339, no. 6, pp. 387–395, 1998.

[50] R. Vardanyan and V. Hruby, "Cardiotonic drugs," in *Synthesis of Essential Drugs*. Elsevier, 2006, pp. 237–243. [Online]. Available: https://doi.org/10.1016/b978-044452166-8/50017-0

[51] F. Leyva, S. Nisam, and A. Auricchio, "20 years of cardiac resynchronization therapy," *Journal of the American College of Cardiology*, vol. 64, no. 10, pp. 1047–1058, 2014.

[52] C. Normand, D. M. Kaye, T. J. Povsic, and K. Dickstein, "Beyond pharmacological treatment: an insight into therapies that target specific aspects of heart failure pathophysiology," *The Lancet*, vol. 393, no. 10175, pp. 1045–1055, 2019.

[53] P. A. Heidenreich, B. Bozkurt, D. Aguilar, L. A. Allen, J. J. Byun, M. M. Colvin, A. Deswal, M. H. Drazner, S. M. Dunlay, L. R. Evers *et al.*, "2022 aha/acc/hfsa guideline for the management of heart failure: Executive summary: a report of the american college of cardiology/american heart association joint committee on clinical practice guidelines," *Journal of the American College of Cardiology*, vol. 79, no. 17, pp. 1757–1780, 2022.

[54] J. Bauersachs, "Heart failure drug treatment: the fantastic four," pp. 681–683, 2021.

[55] E. Donal, G. L'official, and W. Kosmala, "New guidelines for managing chronic heart failure patients and new needs in echocardiography," *International Journal of Cardiology*, 2022.

[56] M. Vaduganathan, B. L. Claggett, P. S. Jhund, J. W. Cunningham, J. P. Ferreira, F. Zannad, M. Packer, G. C. Fonarow, J. J. McMurray, and S. D. Solomon, "Estimating lifetime benefits of comprehensive disease-modifying pharmacological therapies in patients with heart failure with reduced ejection fraction: a comparative analysis of three randomised controlled trials," *The Lancet*, vol. 396, no. 10244, pp. 121–128, 2020.

[57] A. Groenewegen, F. H. Rutten, A. Mosterd, and A. W. Hoes, "Epidemiology of heart failure," *European journal of heart failure*, vol. 22, no. 8, pp. 1342–1356, 2020.

[58] H. B. Sprague, "History and present status of phonocardiography," *IRE Transactions on Medical Electronics*, pp. 2–3, 1957.

[59] K. Sørensen, "Seismocardiography: Interpretation and clinical application," 2021.

[60] W. Einthoven, "Die galvanometrische registrirung des menschlichen elektrokardiogramms, zugleich eine beurtheilung der anwendung des capillar-elektrometers in der physiologie," *Pflügers Archiv European Journal of Physiology*, vol. 99, no. 9, pp. 472–480, 1903.

[61] R. C. Schlant, R. J. Adolph, J. DiMarco, L. S. Dreifus, M. I. Dunn, C. Fisch, A. Garson Jr, L. Haywood, H. J. Levine, and J. A. Murray, "Guidelines for electrocardiography. a report of the american college of cardiology/american heart association task force on assessment of diagnostic and therapeutic cardiovascular procedures (committee on electrocardiography)." *Circulation*, vol. 85, no. 3, pp. 1221–1228, 1992.

[62] C. H. Hertz and I. Edler, "Use of ultrasonic reflectoscope for continuous recording of movements of heart walls, kung fysiograph sallsk," *Lund., Fordhandl*, vol. 24, p. 40, 1954.

[63] J. Gorcsan III, T. Abraham, D. A. Agler, J. J. Bax, G. Derumeaux, R. A. Grimm, R. Martin, J. S. Steinberg, M. S. J. Sutton, and C.-M. Yu, "Echocardiography for cardiac resynchronization therapy: recommendations for performance and reporting–a report from the american society of echocardiography dyssynchrony writing group endorsed by the heart rhythm society," *Journal of the American Society of Echocardiography*, vol. 21, no. 3, pp. 191–213, 2008.

[64] A. F. Rickards, T. BOMBARDINI, G. Corbucci, G. Plicchi, and M. P. S. Group, "An implantable intracardiac accelerometer for monitoring myocardial contractility," *Pacing and clinical electrophysiology*, vol. 19, no. 12, pp. 2066–2071, 1996.

[65] P. S. Halvorsen, A. Espinoza, L. A. Fleischer, O. J. Elle, L. Hoff, R. Lundblad, H. Skulstad, T. Edvardsen, H. Ihlen, and E. Fosse, "Feasibility of a three-axis epicardial accelerometer in detecting myocardial ischemia in cardiac surgical patients," *The Journal of thoracic and cardiovascular surgery*, vol. 136, no. 6, pp. 1496–1502, 2008.

[66] O. T. Inan, M. Etemadi, R. M. Wiard, L. Giovangrandi, and G. Kovacs, "Robust ballistocardiogram acquisition for home monitoring," *Physiological measurement*, vol. 30, no. 2, p. 169, 2009.

[67] K. Tavakolian, O. T. Inan, J.-O. Hahn, and M. Di Rienzo, "Cardiac vibration signals: Old techniques, new tricks, and applications," *Frontiers in Physiology*, p. 1044, 2022.

[68] ©Frontiers Media S.A. 2022 Frontiers in Physiology, "Cardiac vibration signals: Old techniques, new tricks and applications," 2021, accessed: 2022-09-21. [Online]. Available: https://www.frontiersin.org/research-topics/16908/cardiac-vibration-signals-old-techniques-new-tricks-and-applications#impact

[69] C. Yang, F. Fan, N. Aranoff, P. Green, Y. Li, C. Liu, and N. Tavassolian, "An open-access database for the evaluation of cardio-mechanical signals from patients with valvular heart diseases," *Frontiers in Physiology*, vol. 12, 2021.

[70] Z. M. Işilay Zeybek, V. Racca, A. Pezzano, M. Tavanelli, and M. Di Rienzo, "Can seismocardiogram fiducial points be used for the routine estimation of cardiac time intervals in cardiac patients?" *Frontiers in Physiology*, p. 372, 2022.

[71] E. Andreozzi, G. D. Gargiulo, D. Esposito, and P. Bifulco, "A novel broadband forcecardiography sensor for simultaneous monitoring of respiration, infrasonic cardiac vibrations and heart sounds," *Frontiers in physiology*, vol. 12, 2021.

[72] P. Dehkordi, E. P. Bauer, K. Tavakolian, Z. G. Xiao, A. P. Blaber, and F. Khosrow-Khavar, "Detecting coronary artery disease using rest seismocardiography and gyrocardiography," *Frontiers in Physiology*, vol. 12, 2021.

[73] J. Rabineau, A. Nonclercq, T. Leiner, P. v. d. Borne, P.-F. Migeotte, and B. Haut, "Closed-loop multiscale computational model of human blood circulation. applications to ballistocardiography." *Frontiers in physiology*, p. 2112, 2021.

[74] N. M. Marazzi, G. Guidoboni, M. Zaid, L. Sala, S. Ahmad, L. Despins, M. Popescu, M. Skubic, and J. Keller, "Combining physiology-based modeling and evolutionary algorithms for personalized, noninvasive cardiovascular assessment based on electrocardiography and ballistocardiography," *Frontiers in physiology*, p. 1953, 2022.

[75] J. Gordon, "On certain molar movements of the human body produced by the circulation of the blood," *Anat. & Physiol*, vol. 11, p. 533, 1877.

[76] I. Starr, A. Rawson, H. Schroeder, and N. Joseph, "The estimation of cardiac output and the determination of the blood's impacts (ballistocardiogram)," in *Proceedings Am. Soc. Clin. Invest. 30th Annual Meeting, J. Clin. Invest*, vol. 17, 1938, p. 506.

[77] E. Pinheiro, O. Postolache, and P. Girão, "Theory and developments in an unobtrusive cardiovascular system representation: ballistocardiography," *The open biomedical engineering journal*, vol. 4, p. 201, 2010.

[78] O. T. Inan, M. Etemadi, R. M. Wiard, G. T. Kovacs, and L. Giovangrandi, "Novel methods for estimating the ballistocardiogram signal using a simultaneously acquired electrocardiogram," in *2009 Annual International Conference of the IEEE Engineering in Medicine and Biology Society.* IEEE, 2009, pp. 5334–5347.

[79] I. Sadek, J. Biswas, and B. Abdulrazak, "Ballistocardiogram signal processing: a review," *Health information science and systems*, vol. 7, no. 1, pp. 1–23, 2019.

[80] A. Lindqvist, K. Pihlajamäki, J. Jalonen, V. Laaksonen, and J. Alihanka, "Static-charge-sensitive bed ballistocardiography in cardiovascular monitoring," *Clinical Physiology*, vol. 16, no. 1, pp. 23–30, 1996.

[81] O. Inan, M. Etemadi, A. Paloma, L. Giovangrandi, and G. Kovacs, "Non-invasive cardiac output trending during exercise recovery on a bathroom-scale-based ballistocardiograph," *Physiological measurement*, vol. 30, no. 3, p. 261, 2009.

[82] M. Etemadi, O. T. Inan, L. Giovangrandi, and G. T. Kovacs, "Rapid assessment of cardiac contractility on a home bathroom scale," *IEEE transactions on information technology in biomedicine*, vol. 15, no. 6, pp. 864–869, 2011.

[83] D. Da He, E. S. Winokur, and C. G. Sodini, "A continuous, wearable, and wireless heart monitor using head ballistocardiogram (bcg) and head electrocardiogram (ecg)," in *2011 Annual International Conference of the IEEE engineering in medicine and biology society.* IEEE, 2011, pp. 4729–4732.

[84] E. S. Winokur, D. Da He, and C. G. Sodini, "A wearable vital signs monitor at the ear for continuous heart rate and pulse transit time measurements," in *2012 Annual International Conference of the IEEE Engineering in Medicine and Biology Society.* IEEE, 2012, pp. 2724–2727.

[85] E. Pinheiro, O. Postolache, and P. Girao, "Pulse arrival time and ballistocardiogram application to blood pressure variability estimation," in *2009 IEEE International Workshop on Medical Measurements and Applications.* IEEE, 2009, pp. 132–136.

[86] J. H. Shin, K. M. Lee, and K. S. Park, "Non-constrained monitoring of systolic blood pressure on a weighing scale," *Physiological measurement*, vol. 30, no. 7, p. 679, 2009.

[87] R. Casanella, J. Gomez-Clapers, and R. Pallas-Areny, "On time interval measurements using bcg," in *2012 Annual International Conference of the IEEE Engineering in Medicine and Biology Society.* IEEE, 2012, pp. 5034–5037.

[88] B. S. Bozhenko, "Seismocardiography–a new method in the study of functional conditions of the heart," *Terapevticheskii arkhiv*, vol. 33, pp. 55–64, 1961.

[89] P. Mounsey, "Praecordial ballistocardiography," *British heart journal*, vol. 19, no. 2, p. 259, 1957.

[90] K. Sørensen, S. E. Schmidt, A. S. Jensen, P. Søgaard, and J. J. Struijk, "Definition of fiducial points in the normal seismocardiogram," *Scientific reports*, vol. 8, no. 1, pp. 1–11, 2018.

[91] V. Gemignani, E. Bianchini, F. Faita, V. Lionetti, M. Campan, F. A. Recchia, E. Picano, and T. Bombardini, "Transthoracic sensor for noninvasive assessment of left ventricular contractility: validation in a minipig model of chronic heart failure," *Pacing and clinical electrophysiology*, vol. 33, no. 7, pp. 795–803, 2010.

[92] K. Tavakolian, G. Portacio, N. R. Tamddondoust, G. Jahns, B. Ngai, G. A. Dumont, and A. P. Blaber, "Myocardial contractility: A seismocardiography approach," in *2012 Annual International Conference of the IEEE Engineering in Medicine and Biology Society.* IEEE, 2012, pp. 3801–3804.

[93] P. Castiglioni, A. Faini, G. Parati, and M. Di Rienzo, "Wearable seismocardiography," in *2007 29th annual international conference of the IEEE engineering in medicine and biology society.* IEEE, 2007, pp. 3954–3957.

[94] M. Etemadi and O. T. Inan, "Wearable ballistocardiogram and seismocardiogram systems for health and performance," *Journal of Applied Physiology*, vol. 124, no. 2, pp. 452–461, 2018.

[95] K. Tavakolian, "Characterization and analysis of seismocardiogram for estimation of hemodynamic parameters," Ph.D. dissertation, Applied Science: School of Engineering Science, 2010.

[96] M. M. H. Shandhi, J. Fan, J. A. Heller, M. Etemadi, O. Inan, and L. Klein, "Non-invasive seismocardiography can accurately track changes in pulmonary artery pressures during vasodilator challenge at the time of right heart catheterization," *Journal of the American College of Cardiology*, vol. 75, no. 11_Supplement_1, pp. 2075–2075, 2020.

[97] M. Di Rienzo, E. Vaini, P. Castiglioni, G. Merati, P. Meriggi, G. Parati, A. Faini, and F. Rizzo, "Wearable seismocardiography: Towards a beat-by-beat assessment of cardiac mechanics in ambulant subjects," *Autonomic Neuroscience*, vol. 178, no. 1-2, pp. 50–59, 2013.

[98] M. Di Rienzo, E. Vaini, P. Castiglioni, P. Meriggi, and F. Rizzo, "Beat-to-beat estimation of lvet and qs2 indices of cardiac mechanics from wearable seismocardiography in ambu-

lant subjects," in *2013 35th Annual International Conference of the IEEE Engineering in Medicine and Biology Society (EMBC)*. IEEE, 2013, pp. 7017–7020.

[99] K. Tavakolian, G. A. Dumont, G. Houlton, and A. P. Blaber, "Precordial vibrations provide noninvasive detection of early-stage hemorrhage," *Shock*, vol. 41, no. 2, pp. 91–96, 2014.

[100] M. J. Tadi, T. Koivisto, M. Pänkäälä, A. Paasio, T. Knuutila, M. Teräs, and P. Hänninen, "A new algorithm for segmentation of cardiac quiescent phases and cardiac time intervals using seismocardiography," in *Sixth International Conference on Graphic and Image Processing (ICGIP 2014)*, vol. 9443. SPIE, 2015, pp. 571–577.

[101] M. Di Rienzo, E. Vaini, and P. Lombardi, "An algorithm for the beat-to-beat assessment of cardiac mechanics during sleep on earth and in microgravity from the seismocardiogram," *Scientific reports*, vol. 7, no. 1, pp. 1–12, 2017.

[102] E. Andreozzi, A. Fratini, D. Esposito, G. Naik, C. Polley, G. D. Gargiulo, and P. Bifulco, "Forcecardiography: A novel technique to measure heart mechanical vibrations onto the chest wall," *Sensors*, vol. 20, no. 14, p. 3885, 2020.

[103] J. M. Zanetti and K. Tavakolian, "Seismocardiography: Past, present and future," in *2013 35th annual international conference of the IEEE engineering in medicine and biology society (EMBC)*. IEEE, 2013, pp. 7004–7007.

[104] U. Meriheinä, M. Juppo, T. Koivisto, M. Pänkäälä, K. Sairanen, and M. Grönholm, "Heart monitoring system," Mar 2015, WIPO Patent WO 2015/036925 A1.

[105] M. J. Tadi, E. Lehtonen, M. Pankäälä, A. Saraste, T. Vasankari, M. Terás, and T. Koivisto, "Gyrocardiography: A new non-invasive approach in the study of mechanical motions of the heart. concept, method and initial observations," in *2016 38th Annual International Conference of the IEEE engineering in medicine and biology society (EMBC)*. IEEE, 2016, pp. 2034–2037.

[106] P.-F. Migeotte, V. Mucci, Q. Delière, L. Lejeune, and P. v. d. Borne, "Multi-dimensional kineticardiography a new approach for wearable cardiac monitoring through body acceleration recordings," in *XIV Mediterranean Conference on Medical and Biological Engineering and Computing 2016*. Springer, 2016, pp. 1125–1130.

[107] M. Jafari Tadi, E. Lehtonen, A. Saraste, J. Tuominen, J. Koskinen, M. Teräs, J. Airaksinen, M. Pänkäälä, and T. Koivisto, "Gyrocardiography: A new non-invasive monitoring method for the assessment of cardiac mechanics and the estimation of hemodynamic variables," *Scientific reports*, vol. 7, no. 1, pp. 1–11, 2017.

[108] S. Sieciński, P. S. Kostka, and E. J. Tkacz, "Gyrocardiography: A review of the definition, history, waveform description, and applications," *Sensors*, vol. 20, no. 22, p. 6675, 2020.

[109] C. Yang and N. Tavassolian, "Combined seismo-and gyro-cardiography: A more comprehensive evaluation of heart-induced chest vibrations," *IEEE journal of biomedical and health informatics*, vol. 22, no. 5, pp. 1466–1475, 2017.

[110] J. Zia, J. Kimball, M. H. Shandhi, and O. T. Inan, "Automated identification of persistent time-domain features in seismocardiogram signals," in *2019 IEEE EMBS International Conference on Biomedical & Health Informatics (BHI)*. IEEE, 2019, pp. 1–4.

[111] Z. Iftikhar, O. Lahdenoja, M. Jafari Tadi, T. Hurnanen, T. Vasankari, T. Kiviniemi, J. Airaksinen, T. Koivisto, and M. Pänkäälä, "Multiclass classifier based cardiovascular condition detection using smartphone mechanocardiography," *Scientific reports*, vol. 8, no. 1, pp. 1–14, 2018.

[112] S. Mehrang, O. Lahdenoja, M. Kaisti, M. J. Tadi, T. Hurnanen, A. Airola, T. Knuutila, J. Jaakkola, S. Jaakkola, T. Vasankari *et al.*, "Classification of atrial fibrillation and acute decompensated heart failure using smartphone mechanocardiography: a multilabel learning approach," *IEEE Sensors Journal*, vol. 20, no. 14, pp. 7957–7968, 2020.

[113] S. Mehrang, M. J. Tadi, M. Kaisti, O. Lahdenoja, T. Vasankari, T. Kiviniemi, J. Airaksinen, T. Koivisto, and M. Pänkäälä, "Machine learning based classification of myocardial infarction conditions using smartphone-derived seismo-and gyrocardiography," in *2018 Computing in Cardiology Conference (CinC)*, vol. 45. IEEE, 2018, pp. 1–4.

[114] C. Yang, N. D. Aranoff, P. Green, and N. Tavassolian, "Classification of aortic stenosis using time–frequency features from chest cardio-mechanical signals," *IEEE Transactions on Biomedical Engineering*, vol. 67, no. 6, pp. 1672–1683, 2019.

[115] A. Tassin, A. Kobeissi, L. Vitali, F. Rouleau, P. Ritter, G. Gaggini, and J.-M. DUPUIS, "Relationship between amplitude and timing of heart sounds and endocardial acceleration," *Pacing and Clinical Electrophysiology*, vol. 32, pp. S101–S104, 2009.

[116] F. Broussous, A. Kobeissi, J. Dumont, F. Renesto, J. Mansourati *et al.*, "Validation of a marker of atrial contraction in the sonr signal," *World Journal of Cardiovascular Diseases*, vol. 5, no. 03, p. 53, 2015.

[117] P. S. Halvorsen, L. Fleischer, A. Espinoza, O. Elle, L. Hoff, H. Skulstad, T. Edvardsen, and E. Fosse, "Detection of myocardial ischaemia by epicardial accelerometers in the pig," *British journal of anaesthesia*, vol. 102, no. 1, pp. 29–37, 2009.

[118] O.-J. H. Grymyr, A.-T. T. Nguyen, F. Tjulkins, A. Espinoza, E. W. Remme, H. Skulstad, E. Fosse, K. Imenes, and P. S. Halvorsen, "Continuous monitoring of cardiac function by 3-dimensional accelerometers in a closed-chest pig model," *Interactive cardiovascular and thoracic surgery*, vol. 21, no. 5, pp. 573–582, 2015.

[119] A. Wajdan, M. R. Krogh, M. Villegas-Martinez, P. S. Halvorsen, O. J. Elle, and E. W. Remme, "Automatic detection of valve events by epicardial accelerometer allows estimation of the left ventricular pressure trace and pressure–displacement loop area," *Scientific Reports*, vol. 10, no. 1, pp. 1–11, 2020.

[120] M. R. Krogh, P. S. Halvorsen, O.-J. H. Grymyr, J. Bergsland, O. J. Elle, E. Fosse, and E. W. Remme, "Continuous estimation of acute changes in preload using epicardially attached accelerometers," *IEEE Transactions on Biomedical Engineering*, vol. 68, no. 7, pp. 2067–2075, 2020.

[121] A. Wajdan, T. S. Jahren, M. Villegas-Martinez, F. H. Khan, P. S. Halvorsen, H. H. Odland, O. J. Elle, A. H. S. Solberg, and E. W. Remme, "Automatic detection of aortic valve events using deep neural networks on cardiac signals from epicardially placed accelerometer," *IEEE Journal of Biomedical and Health Informatics*, 2022.

[122] L. Brancato, T. Weydts, H. De Clercq, T. Dimiaux, P. Herijgers, and R. Puers, "Biocompatible packaging and testing of an endocardial accelerometer for heart wall motion analysis," *Procedia engineering*, vol. 120, pp. 840–844, 2015.

[123] L. Brancato, T. Weydts, W. Oosterlinck, P. Herijgers, and R. Puers, "Packaging of implantable accelerometers to monitor epicardial and endocardial wall motion," *Biomedical microdevices*, vol. 19, no. 3, pp. 1–10, 2017.

[124] R. C. Álvarez, P.-Y. Joubert, F. Ziglio, A. Amblard, and D. Feuerstein, "Cardiac hemodynamic monitoring in the subcutaneous space: A pre-clinical proof-of-concept," in *2018 IEEE International Symposium on Medical Measurements and Applications (MeMeA)*. IEEE, 2018, pp. 1–6.

[125] R. Cordero, D. Feuerstein, and P.-Y. Joubert, "The cardiac systolic mechanical axis: Optimizing multi-axial cardiac vibrations by projecting along a physiological reference frame," *Biomedical Signal Processing and Control*, vol. 59, p. 101933, 2020.

[126] R. Cordero Álvarez, "Subcutaneous monitoring of cardiac activity for chronically implanted medical devices," Ph.D. dissertation, université Paris-Saclay, 2020.

[127] L. Hoff, O. J. Elle, M. Grimnes, S. Halvorsen, H. J. Alker, and E. Fosse, "Measurements of heart motion using accelerometers," in *The 26th Annual International Conference of the IEEE Engineering in Medicine and Biology Society*, vol. 1. IEEE, 2004, pp. 2049–2051.

[128] R. A. Bronicki, "Hemodynamic monitoring," *Pediatric Critical Care Medicine*, vol. 17, no. 8, pp. S207–S214, 2016.

[129] M. Deterre, "Mems integration for smart medical devices: Opportunities and challenges," in *2012 Symposium on Design, Test, Integration and Packaging of MEMS/MOEMS*. IEEE, 2012, pp. 253–257.

[130] A. Auricchio and W. A. Heggermont, "Technology advances to improve response to cardiac resynchronization therapy: what clinicians should know," *Revista Española de Cardiología (English Edition)*, vol. 71, no. 6, pp. 477–484, 2018.

[131] J. Brugada, P. P. Delnoy, J. Brachmann, D. Reynolds, L. Padeletti, G. Noelker, C. Kantipudi, J. M. Rubin Lopez, W. Dichtl, A. Borri-Brunetto *et al.*, "Contractility sensor-guided optimization of cardiac resynchronization therapy: results from the respond-crt trial," *European Heart Journal*, vol. 38, no. 10, pp. 730–738, 2017.

[132] G. Covino, M. Volpicelli, and P. Capogrosso, "Automatic continuous crt optimization to improve hemodynamic response: An italian single-center experience," *International Journal of Vascular Medicine*, vol. 2020, 2020.

[133] MicroPort-CRM, "Sonrtip™ atrial lead," 2018, accessed: 2022-06-29. [Online]. Available: http://respond-crt-system.com/respond-crt-system/sonr-tip-atrial-lead/

[134] A. T. Sandhu, J. D. Goldhaber-Fiebert, D. K. Owens, M. P. Turakhia, D. W. Kaiser, and P. A. Heidenreich, "Cost-effectiveness of implantable pulmonary artery pressure monitoring in chronic heart failure," *JACC: Heart Failure*, vol. 4, no. 5, pp. 368–375, 2016.

[135] E. Mostafavi, A. K. Dubey, B. Walkowiak, A. Kaushik, S. Ramakrishna, and L. Teodori, "Antimicrobial surfaces for implantable cardiovascular devices," *Current Opinion in Biomedical Engineering*, p. 100406, 2022.

[136] W. T. Abraham, P. B. Adamson, R. C. Bourge, M. F. Aaron, M. R. Costanzo, L. W. Stevenson, W. Strickland, S. Neelagaru, N. Raval, S. Krueger *et al.*, "Wireless pulmonary artery haemodynamic monitoring in chronic heart failure: a randomised controlled trial," *The Lancet*, vol. 377, no. 9766, pp. 658–666, 2011.

[137] I. S. Anand, W. W. Tang, B. H. Greenberg, N. Chakravarthy, I. Libbus, R. P. Katra, M. Investigators *et al.*, "Design and performance of a multisensor heart failure monitoring

algorithm: results from the multisensor monitoring in congestive heart failure (music) study," *Journal of cardiac failure*, vol. 18, no. 4, pp. 289–295, 2012.

[138] D. J. Whellan, K. T. Ousdigian, S. M. Al-Khatib, W. Pu, S. Sarkar, C. B. Porter, B. B. Pavri, C. M. O'Connor, and P. S. Investigators, "Combined heart failure device diagnostics identify patients at higher risk of subsequent heart failure hospitalizations: results from partners hf (program to access and review trending information and evaluate correlation to symptoms in patients with heart failure) study," *Journal of the American College of Cardiology*, vol. 55, no. 17, pp. 1803–1810, 2010.

[139] D. Slotwiner, N. Varma, J. G. Akar, G. Annas, M. Beardsall, R. I. Fogel, N. O. Galizio, T. V. Glotzer, R. A. Leahy, C. J. Love *et al.*, "Hrs expert consensus statement on remote interrogation and monitoring for cardiovascular implantable electronic devices," *Heart rhythm*, vol. 12, no. 7, pp. e69–e100, 2015.

[140] C. Dopierala, P.-Y. Gumérya, M.-R. Frikhaa, J.-J. Thiébaulta, P. Cinquina, and F. Bouchera, "Digital implantable gastric stethoscope for the detection of early signs of acute cardiac decompensation in patients with chronic heart failure." *ACTES DE L'ATELIER IA&SANTE*, 2019.

[141] W. Hasler, "Methods of gastric electrical stimulation and pacing: a review of their benefits and mechanisms of action in gastroparesis and obesity," *Neurogastroenterology & Motility*, vol. 21, no. 3, pp. 229–243, 2009.

[142] F. M. Carrano, M. P. Peev, J. K. Saunders, M. Melis, V. Tognoni, and N. Di Lorenzo, "The role of minimally invasive and endoscopic technologies in morbid obesity treatment: review and critical appraisal of the current clinical practice," *Obesity surgery*, vol. 30, no. 2, pp. 736–752, 2020.

[143] S. Beg, K. Ragunath, A. Wyman, M. Banks, N. Trudgill, M. D. Pritchard, S. Riley, J. Anderson, H. Griffiths, P. Bhandari *et al.*, "Quality standards in upper gastrointestinal endoscopy: a position statement of the british society of gastroenterology (bsg) and association of upper gastrointestinal surgeons of great britain and ireland (augis)," *Gut*, vol. 66, no. 11, pp. 1886–1899, 2017.

[144] M. Šarlija, F. Jurišić, and S. Popović, "A convolutional neural network based approach to qrs detection," in *Proceedings of the 10th international symposium on image and signal processing and analysis*. IEEE, 2017, pp. 121–125.

[145] M. Doyen, D. Ge, A. Beuchée, G. Carrault, and A. I. Hernández, "Robust, real-time generic detector based on a multi-feature probabilistic method," *Plos one*, vol. 14, no. 10, p. e0223785, 2019.

[146] H. Ashouri, S. Hersek, and O. T. Inan, "Universal pre-ejection period estimation using seismocardiography: Quantifying the effects of sensor placement and regression algorithms," *IEEE sensors journal*, vol. 18, no. 4, pp. 1665–1674, 2017.

[147] S. Sahoo, P. Biswal, T. Das, and S. Sabut, "De-noising of ecg signal and qrs detection using hilbert transform and adaptive thresholding," *Procedia Technology*, vol. 25, pp. 68–75, 2016.

[148] S. Chatterjee, R. S. Thakur, R. N. Yadav, L. Gupta, and D. K. Raghuvanshi, "Review of noise removal techniques in ecg signals," *IET Signal Processing*, vol. 14, no. 9, pp. 569–590, 2020.

[149] Z. Yu, F. M. Bui, P. Babyn, and A. Dinh, "Evaluation of compressed sensing in seismocardiogram (scg) systems," in *2013 26th IEEE Canadian Conference on Electrical and Computer Engineering (CCECE)*. IEEE, 2013, pp. 1–4.

[150] M. D. Deborah, J. Prasad, A. Aamina, and A. R. Devi, "Phonocardiogram signal processing using lms adaptive algorithm," *International Journal of Multidisciplinary Approach and Studies*, vol. 3, no. 2, pp. 66–73, 2016.

[151] P. Ponikowski, A. A. Voors, S. D. Anker, H. Bueno, J. G. Cleland, A. J. Coats, V. Falk, J. R. González-Juanatey, V.-P. Harjola, E. A. Jankowska *et al.*, "2016 esc guidelines for the diagnosis and treatment of acute and chronic heart failure: The task force for the diagnosis and treatment of acute and chronic heart failure of the european society of cardiology (esc) developed with the special contribution of the heart failure association (hfa) of the esc," *European heart journal*, vol. 37, no. 27, pp. 2129–2200, 2016.

[152] S. E. Schmidt, C. Holst-Hansen, C. Graff, E. Toft, and J. J. Struijk, "Segmentation of heart sound recordings by a duration-dependent hidden markov model," *Physiological measurement*, vol. 31, no. 4, p. 513, 2010.

[153] O. T. Inan, M. Baran Pouyan, A. Q. Javaid, S. Dowling, M. Etemadi, A. Dorier, J. A. Heller, A. O. Bicen, S. Roy, T. De Marco *et al.*, "Novel wearable seismocardiography and machine learning algorithms can assess clinical status of heart failure patients," *Circulation: Heart Failure*, vol. 11, no. 1, p. e004313, 2018.

[154] K. Cao, Y. Liu, G. Meng, and Q. Sun, "An overview on edge computing research," *IEEE access*, vol. 8, pp. 85 714–85 728, 2020.

[155] R. K. Sevakula, W.-T. M. Au-Yeung, J. P. Singh, E. K. Heist, E. M. Isselbacher, and A. A. Armoundas, "State-of-the-art machine learning techniques aiming to improve pa-

tient outcomes pertaining to the cardiovascular system," *Journal of the American Heart Association*, vol. 9, no. 4, p. e013924, 2020.

[156] J. C. Miller, D. Skoll, and L. A. Saxon, "Home monitoring of cardiac devices in the era of covid-19," *Current Cardiology Reports*, vol. 23, no. 1, pp. 1–9, 2021.

[157] Raspberry Pi, "Raspberry pi 3 model b+," 2022, accessed: 2022-08-18. [Online]. Available: https://www.raspberrypi.org

[158] ©2022 HiFiBerry and K. Borgerink, "Datasheet dac+ adc pro," Oct 2020, accessed: 2022-08-18. [Online]. Available: https://www.hifiberry.com/docs/data-sheets/datasheet-dac-adc-pro/

[159] J. Pan and W. J. Tompkins, "A real-time qrs detection algorithm," *IEEE transactions on biomedical engineering*, no. 3, pp. 230–236, 1985.

[160] ©2022 STMicroelectronics, "inemo inertial module with machine learning core, finite state machine and advanced digital functions. ultra-low power for battery operated iot, gaming, wearable and personal electronics," Apr 2022, accessed: 2022-08-18. [Online]. Available: https://www.st.com/content/st_com/en/products/mems-and-sensors/inemo-inertial-modules/lsm6dsox.html

[161] F. Khosrow-Khavar, K. Tavakolian, A. Blaber, and C. Menon, "Automatic and robust delineation of the fiducial points of the seismocardiogram signal for noninvasive estimation of cardiac time intervals," *IEEE Transactions on Biomedical Engineering*, vol. 64, no. 8, pp. 1701–1710, 2016.

[162] D. S. Morillo, J. L. R. Ojeda, L. F. C. Foix, and A. L. Jiménez, "An accelerometer-based device for sleep apnea screening," *IEEE transactions on information technology in biomedicine*, vol. 14, no. 2, pp. 491–499, 2009.

[163] J. Centracchio, E. Andreozzi, D. Esposito, G. D. Gargiulo, and P. Bifulco, "Detection of aortic valve opening and estimation of pre-ejection period in forcecardiography recordings," *Bioengineering*, vol. 9, no. 3, p. 89, 2022.

[164] R. Fadil, P. Aarotale, B. Hoffmann, F. Khosrow-Khavar, Z. G. Xiao, A. Akhbardeh, and K. Tavakolian, "Temporal changes of fiducial seismocardiogram points due to different sensor placements on the chest," in *2020 Computing in Cardiology*. IEEE, 2020, pp. 1–4.

[165] H. Ferdinando, E. Seppälä, and T. Myllylä, "Discrete wavelet transforms-based analysis of accelerometer signals for continuous human cardiac monitoring," *Applied Sciences*, vol. 11, no. 24, p. 12072, 2021.

[166] I. Antonov, "Sensors with artificial intelligence," Master's thesis, Escuela Técnica Superior de Ingenieros Industriales y de Telecomunicación, Universidad de Cantabria, 2021.

[167] E. Anceschi, G. Bonifazi, M. C. De Donato, E. Corradini, D. Ursino, and L. Virgili, "Savemenow. ai: a machine learning based wearable device for fall detection in a workplace," in *Enabling AI Applications in Data Science*. Springer, 2021, pp. 493–514.

[168] G. Bonifazi, E. Corradini, D. Ursino, L. Virgili, E. Anceschi, and M. C. De Donato, "A machine learning based sentient multimedia framework to increase safety at work," *Multimedia tools and applications*, vol. 81, no. 1, pp. 141–169, 2022.

[169] R. B. Berry, C. A. Kushida, M. H. Kryger, H. Soto-Calderon, B. Staley, and S. T. Kuna, "Respiratory event detection by a positive airway pressure device," *Sleep*, vol. 35, no. 3, pp. 361–367, 2012.

[170] D. Feuerstein, L. Graindorge, A. Amblard, A. Tatar, G. Guerrero, S. Christophle-Boulard, C. Loiodice, A. I. Hernandez, and J.-L. Pépin, "Real-time detection of sleep breathing disorders," in *2015 Computing in Cardiology Conference (CinC)*. IEEE, 2015, pp. 317–320.

[171] A. Hernández, G. Guerrero, D. Feuerstein, L. Graindorge, D. Perez, A. Amblard, P. Mabo, J.-L. Pépin, and L. Senhadji, "Pasithea: An integrated monitoring and therapeutic system for sleep apnea syndromes based on adaptive kinesthetic stimulation," *Irbm*, vol. 37, no. 2, pp. 81–89, 2016.

[172] D. Ge and A. Hernández, "Multi-feature probabilistic detector applied to apnea/hypopnea monitoring," in *2019 Computing in Cardiology (CinC)*. IEEE, 2019, pp. 1–4.

[173] N. Zavanelli, H. Kim, J. Kim, R. Herbert, M. Mahmood, Y.-S. Kim, S. Kwon, N. B. Bolus, F. B. Torstrick, C. S. Lee *et al.*, "At-home wireless monitoring of acute hemodynamic disturbances to detect sleep apnea and sleep stages via a soft sternal patch," *Science advances*, vol. 7, no. 52, p. eabl4146, 2021.

[174] Q. Shen, H. Qin, K. Wei, and G. Liu, "Multiscale deep neural network for obstructive sleep apnea detection using rr interval from single-lead ecg signal," *IEEE Transactions on Instrumentation and Measurement*, vol. 70, pp. 1–13, 2021.

[175] S. Lee, Y. Chu, J. Ryu, Y. J. Park, S. Yang, and S. B. Koh, "Artificial intelligence for detection of cardiovascular-related diseases from wearable devices: a systematic review and meta-analysis," *Yonsei medical journal*, vol. 63, no. Suppl, p. S93, 2022.

[176] F. Daghero, C. Xie, D. J. Pagliari, A. Burrello, M. Castellano, L. Gandolfi, A. Calimera, E. Macii, and M. Poncino, "Ultra-compact binary neural networks for human activity recognition on risc-v processors," in *Proceedings of the 18th ACM International Conference on Computing Frontiers*, 2021, pp. 3–11.

[177] M. Demler, "Mythic multiplies in a flash," *Microprocesser Report*, 2018.

[178] L. G. Wright, T. Onodera, M. M. Stein, T. Wang, D. T. Schachter, Z. Hu, and P. L. McMahon, "Deep physical neural networks trained with backpropagation," *Nature*, vol. 601, no. 7894, pp. 549–555, 2022.

COLLEGE DOCTORAL BRETAGNE | MATHS, TELECOMS INFORMATIQUE, SIGNAL SYSTEMES, ELECTRONIQUE

Université de Rennes

Titre : Analyse des signaux de vibrations cardiaques thoraciques et intra-gastriques pour le suivi de l'insuffisance cardiaque

Mot clés : Signaux de vibrations cardiaques, Mécanocardiogramme (MCG), Dispositifs implantables, Insuffisance cardiaque, Apprentissage automatique, Traitement des signaux biomédicaux

Résumé : Le développement d'un système de surveillance des vibrations cardiaques offrant une gestion intégrée des paramètres multimodaux avec un dispositif peu invasif est actuellement nécessaire dans le domaine des maladies cardiovasculaires chroniques, afin de déclencher une attention médicale précoce et adéquate contre les événements de décompensation et de réduire les hospitalisations. L'objectif principal de cette thèse est de proposer des méthodes d'acquisition et de traitement du signal afin d'utiliser au mieux les unités inertielles dans le suivi des patients atteints d'insuffisance cardiaque (HF), en exploitant efficacement les informations multimodales des signaux de vibration cardiaque (CVS). Deux nouvelles approches sont proposées dans ce contexte : 1) l'évaluation de la faisabilité de l'acquisition des CVS longitudinaux en utilisant un implant intragastrique dans une configuration d'expérimentation animale préclinique, et 2) le développement d'un système d'acquisition de signaux cardiaques afin d'évaluer de manière préliminaire la faisabilité de la détection automatique d'événements cardiorespiratoires on-the-edge à l'aide d'un capteur MEMS avec un noyau d'apprentissage automatique intégré (MLC). Les résultats obtenus montrent les premières preuves précliniques de la faisabilité d'une surveillance cardiovasculaire chronique à partir d'un dispositif cardiaque implantable peu invasif placé dans le fond de l'estomac, ainsi que la faisabilité préliminaire de l'utilisation d'un MLC intégré dans un capteur MEMS pour la détection on-the-edge de plusieurs événements cardiorespiratoires liés à des variations hémodynamiques, comme l'apnée et la manœuvre de Valsalva. La nature transversale de l'ensemble du contenu de cette thèse ouvre de nouvelles perspectives dans l'utilisation des CVS pour le développement de méthodes et d'outils pouvant être utilisés dans la surveillance cardiovasculaire à long terme de patients diagnostiqués avec une maladie cardiaque chronique telle que l'HF.

Title: Analysis of thoracic and intra-gastric cardiac vibration signals for the monitoring of heart failure

Keywords: Cardiac vibration signals, Mechanocardiogram (MCG), Implantable devices, Heart failure, Machine learning, Biomedical signal processing

Abstract: The development of a remote cardiac vibrations monitoring system offering integrated management of multimodal parameters with a minimally invasive device is currently needed in the chronic cardiovascular diseases domain, aiming to trigger early and adequate medical attention against the decompensation events and to reduce hospitalization. The main objective of this thesis is to propose signal acquisition and processing methods to make the best use of inertial units in the monitoring of patients with heart failure (HF), by efficiently exploiting multimodal information from cardiac vibration signals (CVS). Two novel approaches are proposed in this context: 1) the evaluation of the feasibility of acquiring longitudinal CVS using an intra-gastric implant in a preclinical animal experimentation setup, and 2) the development of a cardiac signal acquisition system to preliminarily assess the feasibility of automatically detecting cardiorespiratory events on-the-edge using a MEMS sensor with an embedded machine learning core (MLC). The obtained results show initial preclinical evidence on the feasibility of chronic cardiovascular monitoring from a minimally invasive implantable cardiac device placed in the gastric fundus, and preliminary feasibility for using a MLC embedded in a MEM sensor for on-the-edge detection of multiple cardiorespiratory events related to hemodynamic variations, such as apnea and Valsalva maneuver. The cross-cutting nature of the entire content of this thesis opens up new perspectives in the use of CVS for the development of methods and tools that can be used in the long-term cardiovascular monitoring of patients diagnosed with chronic heart disease such as HF.